

Alma Mater Studiorum – Università di Bologna

DOTTORATO DI RICERCA IN

Disegno e Metodi dell'Ingegneria Industriale  
e Scienze Aerospaziali

Ciclo XXVI

**Settore Concorsuale di afferenza:** 09/A1 Ingegneria Aeronautica, Aerospaziale e Navale

**Settore Scientifico disciplinare:** ING-IND/05 Impianti e Sistemi Aerospaziali

TITOLO TESI

**DEVELOPMENT OF NEW TOOLKITS  
FOR ORBIT DETERMINATION CODES  
FOR PRECISE RADIO TRACKING EXPERIMENTS**

**Presentata da: Marco Zannoni**

**Coordinatore Dottorato**

**Prof. Vincenzo Parenti Castelli**

**Relatore**

**Prof. Paolo Tortora**

**Esame finale anno 2014**



To my family, the old and the new.



# Author's Note

This thesis is continuously revised to correct all the errors that are found during a never-ending revision process. To obtain the most updated version, please feel free to contact the author by sending an e-mail at: [m.zannoni@unibo.it](mailto:m.zannoni@unibo.it).



# Summary

This thesis describes the developments of new models and toolkits for the orbit determination codes to support and improve the precise radio tracking experiments of the Cassini-Huygens mission.

Cassini-Huygens is a joint NASA/ESA/ASI interplanetary mission dedicated to the study of the Saturn's planetary system which, composed by the planet Saturn itself, its natural satellites and rings, is one of the most complex and interesting planetary systems known. In the mission context, the radio science subsystem provides fundamental information about the Saturn's rings, its atmosphere and ionosphere and the gravity fields of Saturn and its main satellites. In particular, the determination of the gravity field of a celestial body plays a crucial role in the investigation of its internal composition, structure and evolution, because it provides one of the very few direct measurements of its internal mass distribution, even if with various limitations. The gravity radio science is a particular application of the precise orbit determination of an interplanetary spacecraft, which consists in the estimation of a set of parameters that unambiguously defines its trajectory. The core of the process is the comparison between measured observables and the corresponding computed values, obtained by an orbit determination program using the adopted mathematical models. Hence, disturbances in either the observed or computed observables degrades the orbit determination process. While the different sources of noise in the Doppler measurements were the subject of several studies in the past, the errors in the computed Doppler observables were not previously analyzed and characterized in details.

Chapter 2 describes a detailed study of the numerical errors in the Doppler observables computed by the most important interplanetary orbit determination programs: NASA/JPL's ODP (Orbit Determination Program) and MONTE (Mission-analysis, Operations, and Navigation Toolkit Environment), and ESA/ESOC's AMFIN (Advanced Modular Facility for Interplanetary Navigation). During this study a mathematical model of the numerical noise was developed. The model was successfully validated analyzing directly the numerical noise in Doppler observables computed by the ODP and MONTE, showing a relative error always smaller than 50%, with typical values better than 10%. An accurate prediction of the numerical noise can be used to compute a proper noise budget in Doppler tracking of interplanetary spacecraft. This represents a critical step for the design of future interplanetary missions, both for radio science experiments, requiring the highest level of accuracy, and spacecraft navigation. As a result, the numerical noise proved to be, in general, an important source of noise in the orbit determination process and, in some conditions, it may becomes the dominant noise source. On the basis

of the numerical errors characterization, three different approaches to reduce the numerical noise were proposed.

MONTE is the new orbit determination software developed since late 2000s by the NASA/JPL. Only recently it was considered sufficiently stable to completely replace the ODP for the orbit determination of all the operational missions managed by the JPL. In parallel, MONTE replaced the ODP also for the analysis of radio science gravity experiment, so new set-ups, toolkits and procedures were developed to perform this task. In particular, to analyze the data acquired during the Cassini gravity radio science experiments the use of a multi-arc procedure is crucial while, at present, MONTE supports only a single-arc approach. Chapter 3 describes the development of the `multiarc` MONTE-Python library, which allows to extend the Monte capabilities to perform a multi-arc orbit determination. The library was developed and successfully tested during the analysis of the Cassini radio science gravity experiments of the Saturn's satellite Rhea.

Discovered on 1672 by Giovanni Domenico Cassini, Rhea is the second largest moon of Saturn. Before the Cassini arrival to Saturn, only the gravitational parameter  $GM$  was known, from the analysis of Pioneer and Voyager data. During its mission in the Saturn's system, Cassini encountered Rhea four times, but only two flybys were devoted to gravity investigations. The first gravity flyby, referred to as R1 according to the numbering scheme used by the project Cassini, was performed on November 2005. The radiometric data acquired during this encounter were analyzed by the scientific community with two different approaches, obtaining non-compatible estimations of the Rhea's gravity field. A first approach assumed *a priori* the hydrostatic equilibrium, deriving that Rhea's interior is a homogeneous, undifferentiated mixture of ice and rock, with possibly some compression of the ice and transition from ice I and ice II at depth. A second approach computed an unconstrained estimation of the quadrupole gravity field coefficients  $J_2$ ,  $C_{22}$  and  $S_{22}$ , obtaining a solution non statistically compatible with the condition of hydrostatic equilibrium. In this case, no useful constraint on Rhea's interior structure could be imposed. To resolve these discrepancies, a second and last gravity fly-by of Rhea, referred to as R4, was performed on March 2013. Chapter 4 presents the estimation of the Rhea's gravity field obtained from a joint multi-arc analysis of R1 and R4, describing in details the spacecraft dynamical model used, the data selection and calibration procedure, and the analysis method followed. In particular, the approach of estimating the full unconstrained quadrupole gravity field was followed, obtaining a solution statistically not compatible with the condition of hydrostatic equilibrium. To test the stability of the solution, different multi-arc analysis were performed, varying the data set, the strategy for the update of the satellite ephemerides and the dynamical model. The solution proved to be stable and reliable. Given the non-hydrostaticity, very few considerations about the internal structure of Rhea can be made. In particular, the computation of the moment of inertia factor using the Radau-Darwin equation can introduce large errors. Nonetheless, even by accounting for this possible error, the normalized moment of inertia is in the range 0.37-0.4 indicating that Rhea's may be almost homogeneous, or at least characterized by a small degree of differentiation. The internal composition cannot be assessed with more details with the available data but, unfortunately, no other gravity flybys are scheduled up to the end of the mission in 2017.

# Sommario

Questa tesi descrive lo sviluppo di nuovi modelli e strumenti per codici di determinazione orbitale, per supportare e migliorare gli esperimenti di radio tracking della missione Cassini-Huygens.

Cassini-Huygens è una missione spaziale interplanetaria dedicata allo studio del sistema planetario di Saturno che, costituito dallo stesso pianeta Saturno, dalle sue lune e dagli anelli, è uno dei sistemi planetari più complessi ed interessanti del sistema solare. In questo contesto, il sottosistema di Radio Scienza fornisce misure fondamentali degli anelli di Saturno, la sua atmosfera e ionosfera, e dei campi gravitazionali di Saturno e dei suoi satelliti principali. In particolare, la determinazione del campo di gravità di un corpo celeste ha un ruolo cruciale nello studio della sua composizione interna, struttura ed evoluzione, in quanto costituisce uno delle pochissime misure dirette della distribuzione interna della sua massa, anche se non attraverso una relazione univoca. Gli esperimenti di radio scienza dedicati alla gravità rappresentano una particolare applicazione del processo di determinazione orbitale di un veicolo spaziale interplanetario, che consiste nella stima di un insieme di parametri che definisce univocamente la sua traiettoria. Il processo di stima è basato sulla comparazione tra le reali misure ottenute a terra e i corrispondenti valori simulati usando dei modelli matematici. Di conseguenza, la stima viene degradata sia da errori sulle misure, sia da errori sulle osservabili simulate. Mentre le diverse sorgenti di rumore di misura sono state oggetto in passato di diversi studi, gli errori sulle osservabili simulate non sono stati mai analizzati in dettaglio.

Il Capitolo 2 descrive uno studio approfondito dei rumori numerici che caratterizzano le osservabili calcolate attraverso i principali software di determinazione orbitale: ODP e MONTE del NASA/JPL, e AMFIN di ESA/ESOC. Durante questo studio un modello matematico del rumore numerico è stato sviluppato. Il modello è stato validato analizzando direttamente il rumore numerico sulle osservabili Doppler calcolate da ODP e da MONTE, mostrando un errore relativo sempre inferiore al 50%, con valori tipici inferiori al 10%. Una predizione accurata del rumore numerico può essere usata per calcolare un più accurato *noise budget* del *tracking* Doppler di missioni interplanetarie. Questo rappresenta un aspetto critico nello sviluppo di future missioni, sia per la navigazione, sia per gli esperimenti di radio scienza, che richiedono le accuratezze più elevate. In generale, il rumore numerico si è rivelato essere un'importante sorgente di rumore nel processo di determinazione orbitale e, in alcune condizioni, può rappresentare la sorgente di rumore dominante. La caratterizzazione del rumore numerico ha permesso di identificare tre possibili approcci per ridurre il rumore numerico.

MONTE è il nuovo software di determinazione orbitale sviluppato sin dalla fine degli anni 2000 dal NASA/JPL. Solo recentemente MONTE è stato considerato sufficientemente stabile per sostituire completamente ODP nella determinazione orbitale delle missioni operative gestite dal JPL. Di conseguenza, MONTE ha sostituito ODP anche nell'analisi degli esperimenti di radio scienza, e a questo scopo nuovi set-up, strumenti e procedure sono stati sviluppati. In particolare, l'utilizzo del metodo multi-arco è fondamentale per l'analisi dei dati acquisiti durante gli esperimenti di radio scienza di Cassini dedicati alla gravità ma, attualmente, MONTE supporta solo il metodo singolo arco. Il Capitolo 3 descrive lo sviluppo e le caratteristiche della libreria MONTE-Python `multiarc`, che permette di estendere le funzionalità di Monte per effettuare analisi multi-arco. La libreria è stata sviluppata e testata durante l'analisi degli esperimenti di radio scienza di Cassini dedicati alla stima del campo di gravità di Rea.

Scoperto nel 1672 da Giovanni Domenico Cassini, Rea è il secondo più grande satellite di Saturno. Prima dell'arrivo della missione Cassini a Saturno, solo il  $GM$  di Rea era noto, attraverso l'analisi dei dati delle missioni Pioneer e Voyager. Durante la missione di Cassini nel sistema di Saturno, sono stati realizzati quattro *fly-bys* di Rea, di cui solo due dedicati alla stima del campo di gravità. Il primo fly-by, denominato R1 secondo lo schema di numerazione usato dal progetto Cassini, è stato effettuato nel Novembre 2005. I dati raccolti durante questo incontro sono stati analizzati dalla comunità scientifica utilizzando due approcci differenti, ottenendo stime del campo di gravità differenti e non compatibili tra loro. Una prima soluzione fu ottenuta assumendo *a priori* la condizione di equilibrio idrostatico, deducendo che Rea è un miscuglio omogeneo, non differenziato, di ghiaccio e roccia, con una possibile presenza di compressione del ghiaccio e transizione in profondità da ghiaccio I a ghiaccio II. Una seconda soluzione, ottenuta stimando un i coefficienti del campo di quadrupolo  $J_2$ ,  $C_{22}$  e  $S_{22}$  senza alcun vincolo, risultò non essere statisticamente compatibile con la condizione di equilibrio idrostatico. Di conseguenza alcun vincolo sulla possibile struttura interna di Rea potè essere imposto. Per risolvere questo disaccordo, un secondo e ultimo fly-by di Rea, denominato R4, fu pianificato ed eseguito nel Marzo 2013. Il Capitolo 4 presenta la stima del campo di gravità di Rea ottenuta dall'analisi dati congiunta di R1 e R4, descrivendo in dettaglio il modello dinamico della sonda utilizzato, la procedura di selezione e calibrazione dei dati, e il metodo di analisi adottato. In particolare, si è scelto di stimare l'intero campo gravitazionale di quadrupolo, senza alcun vincolo *a priori*, ottenendo una soluzione non compatibile con la condizione di equilibrio idrostatico. Per testare la stabilità della soluzione diverse analisi multi-arco sono state realizzate, modificando i dati analizzati, la strategia di aggiornamento delle effemeridi satellitari e il modello dinamico. La soluzione si è dimostrata stabile e affidabile. Data la condizione non idrostatica, poche considerazioni possono essere fatte sulla struttura interna di Rea. In particolare, il calcolo del momento di inerzia utilizzando l'equazione di Radau-Darwin non è del tutto affidabile. Nonostante ciò, anche considerando i possibili errori, il momento di inerzia normalizzato ottenuto si trova nel range 0.37-0.4, indicando che Rea potrebbe essere omogeneo, o almeno con un basso livello di differenziazione. Tuttavia, la composizione interna non può essere valutata più in dettaglio con i dati disponibili e, sfortunatamente, non sono previsti altri fly-by di Rea dedicati alla gravità fino alla fine della missione nel 2017.

# Contents

<b>Acronyms</b>	<b>xix</b>
<b>1 Introduction</b>	<b>1</b>
1.1 The Cassini-Huygens Mission . . . . .	1
1.1.1 The Scientific Objectives . . . . .	2
1.1.2 The Cassini Mission . . . . .	3
1.1.3 The Cassini-Huygens Spacecraft . . . . .	4
1.1.4 The Cassini Radio Science Subsystem . . . . .	6
1.1.4.1 Scientific Objectives . . . . .	6
1.1.4.2 Overview . . . . .	7
1.1.4.3 Spacecraft Segment . . . . .	8
1.1.4.4 Ground Segment . . . . .	10
1.2 The Orbit Determination Problem . . . . .	12
1.2.1 Introduction . . . . .	12
1.2.2 Pre-processing of radiometric measurements . . . . .	13
1.2.3 Observables and partials computation . . . . .	14
1.2.3.1 Planetary and/or Satellite ephemerides update . . . . .	14
1.2.3.2 Trajectory Integration . . . . .	15
1.2.3.3 Time transformations . . . . .	16
1.2.3.4 Ground station state computation . . . . .	17
1.2.3.5 Light-time solution computation . . . . .	18
1.2.3.6 Observables computation . . . . .	18
1.2.4 Estimation Filter . . . . .	19
1.2.5 Solution Analysis . . . . .	19
<b>2 Numerical Noise</b>	<b>21</b>
2.1 Introduction . . . . .	21
2.2 The Round-Off Errors . . . . .	23
2.2.1 The Floating Point Representation . . . . .	23
2.2.1.1 The Effect of the Measurement Units . . . . .	25
2.2.2 The Statistical Model . . . . .	26
2.2.3 Operation Errors . . . . .	27
2.3 The Numerical Error Model . . . . .	28
2.3.1 Differenced-Range Doppler Formulation . . . . .	28
2.3.2 Sources of Numerical Errors and Order of Magnitude Considerations . . . . .	30
2.3.2.1 Representation of Times . . . . .	30

2.3.2.2	Representation of Distances . . . . .	32
2.3.2.3	Additional Rounding Errors . . . . .	32
2.3.3	Numerical Error Preliminary Model . . . . .	33
2.3.4	Validation of the Widrow's Model . . . . .	35
2.3.5	Numerical Error Complete Model . . . . .	37
2.4	Model Validation . . . . .	38
2.4.1	Validation Procedure . . . . .	38
2.4.2	The Six-Parameter Fit . . . . .	39
2.4.3	Validation Results . . . . .	40
2.4.3.1	ODP . . . . .	40
2.4.3.2	MONTE . . . . .	44
2.4.4	Validation Conclusions . . . . .	49
2.5	Numerical Noise Analysis . . . . .	49
2.5.1	ODP Numerical Noise . . . . .	50
2.5.2	MONTE Numerical Noise . . . . .	54
2.6	Numerical Noise Mitigation . . . . .	54
2.7	Conclusions . . . . .	58
<b>3</b>	<b>Multi-Arc Toolkit</b>	<b>59</b>
3.1	Introduction . . . . .	59
3.2	The Single-Arc Approach . . . . .	59
3.3	The Multi-Arc Approach . . . . .	61
3.4	The Multi-Arc Monte Library . . . . .	62
3.4.1	Implementation . . . . .	62
3.4.1.1	The "external" approach . . . . .	62
3.4.1.2	The "multi-spacecraft" approach . . . . .	62
3.4.1.3	The "hybrid" approach . . . . .	63
3.4.2	The Multi-Arc Analysis Procedure . . . . .	64
3.4.3	Set-Up of a Multi-Arc Analysis . . . . .	66
3.4.3.1	Create the Multi-Arc Directory . . . . .	66
3.4.3.2	Add and Configure the Single Arcs . . . . .	67
3.4.3.3	Configure the Multi-Arc <code>Options.mpy</code> . . . . .	68
3.4.3.4	Configure the Multi-Arc Setup File . . . . .	68
3.4.3.5	Configure the Multi-Arc Filter . . . . .	69
3.4.4	Analysis Execution . . . . .	70
3.4.5	Current Limitations . . . . .	70
3.5	Conclusions and Future Work . . . . .	70
<b>4</b>	<b>Rhea Gravity Field</b>	<b>73</b>
4.1	Introduction . . . . .	73
4.2	Dynamical Model . . . . .	76
4.2.1	Gravitational Accelerations . . . . .	77
4.2.1.1	Rhea Rotation Model . . . . .	77
4.2.2	Non-Gravitational Accelerations . . . . .	78
4.2.2.1	Maneuvers . . . . .	79
4.2.2.2	RTGs . . . . .	79
4.2.2.3	Solar Radiation Pressure . . . . .	80

4.2.2.4	Saturn Albedo . . . . .	80
4.2.2.5	Atmospheric Drag . . . . .	80
4.3	Satellite Ephemerides Update . . . . .	80
4.4	Data . . . . .	82
4.4.1	Data Selection . . . . .	82
4.4.2	Data Calibration . . . . .	83
4.4.2.1	Time synchronization of AMC data . . . . .	83
4.5	Estimation . . . . .	86
4.6	Results . . . . .	88
4.6.1	Residuals . . . . .	88
4.6.2	Rhea Gravity Field . . . . .	89
4.6.3	Comments . . . . .	89
4.6.3.1	MONTE Set-Up Validation . . . . .	89
4.6.3.2	The Multi-Arc Strategy . . . . .	97
4.6.3.3	The Satellite Ephemerides Update Strategy . . . . .	98
4.7	Interpretation . . . . .	98
<b>5</b>	<b>Conclusions</b>	<b>101</b>
	<b>Bibliography</b>	<b>105</b>



# List of Figures

1.1	The Cassini-Huygens spacecraft in cruise configuration. . . . .	5
2.1	Round-off errors in time variables for ODP, AMFIN and MONTE. . . . .	31
2.2	Autocorrelation of $\Delta\bar{t}_3$ , computed on different tracking passes. . . . .	37
2.3	Time variation of the autocorrelation of $\Delta\bar{t}_3$ after $T_c = 60$ s. . . . .	38
2.4	ODP numerical noise residuals. . . . .	41
2.5	ODP numerical noise standard deviation: Cassini scenario. . . . .	42
2.6	ODP numerical noise standard deviation: Juno scenario. . . . .	43
2.7	MONTE numerical noise residuals. . . . .	45
2.8	MONTE numerical noise residuals: Juno scenario (bad points zoom). . . . .	46
2.9	MONTE numerical noise standard deviation: Cassini Scenario. . . . .	47
2.10	MONTE numerical noise standard deviation: Juno Scenario. . . . .	48
2.11	ODP numerical noise: Cassini cruise phase. . . . .	51
2.12	ODP numerical noise: Cassini Nominal and Equinox Missions. . . . .	51
2.13	ODP numerical noise: Cassini Solstice Mission. . . . .	52
2.14	ODP numerical noise: Juno Nominal Mission. . . . .	52
2.15	MONTE numerical noise: Cassini cruise phase. . . . .	55
2.16	MONTE numerical noise: Cassini Nominal and Equinox Missions. . . . .	55
2.17	MONTE numerical noise: Cassini Solstice Mission. . . . .	56
2.18	MONTE numerical noise: Juno Nominal Mission. . . . .	56
3.1	multiarc library: block diagram of the multi-arc procedure. . . . .	65
4.1	Estimations of Rhea $J_2$ and $C_{22}$ published to date. . . . .	75
4.2	Rhea R1 and R4 ground tracks. . . . .	76
4.3	Cassini elevation during R1 and R4. . . . .	84
4.4	R4 AMC on DSS-55: cross-correlation with residuals. . . . .	85
4.5	R4 AMC on DSS-25: cross-correlation with residuals. . . . .	86
4.6	Sol-R1 and Sol-R4: range-rate residuals. . . . .	90
4.7	Sol-MA-0: range-rate residuals. . . . .	91
4.8	Sol-MA: range-rate residuals. . . . .	92
4.9	Sol-MA-L: range-rate residuals. . . . .	93
4.10	Sol-MA-HE: range-rate residuals. . . . .	94
4.11	Rhea $GM$ 1-sigma error bars. . . . .	95
4.12	Rhea $J_2$ - $C_{22}$ 1-sigma error ellipses. . . . .	95
4.13	Rhea $J_2/C_{22} - 10/3$ 1-sigma error bars. . . . .	97



# List of Tables

2.1	Binary formats defined by IEEE-754. . . . .	25
2.2	List of bodies abbreviations. . . . .	29
4.1	Rhea characteristics. . . . .	73
4.2	R1 and R4 characteristics. . . . .	75
4.3	Coefficients defining the Cassini RTG acceleration. . . . .	80
4.4	Rhea estimated gravity fields. . . . .	96
4.5	Rhea Fluid Love's Number and $C/MR^2$ . . . . .	100



# Acronyms

<b>AMC</b>	Advanced Media Calibration system
<b>ASD</b>	Allan Standard Deviation
<b>AV</b>	Allan Variance
<b>AWVR</b>	Advanced Water Vapour Radiometer
<b>BWG</b>	Beam Wave Guided Antenna
<b>C/A</b>	Closest Approach
<b>CSO</b>	Cryogenically-cooled Sapphire Oscillator
<b>DDOR</b>	Delta Differential One-way Ranging
<b>DOR</b>	Differential One-way Ranging
<b>DRVID</b>	Differenced Range Versus Integrated Doppler
<b>DSN</b>	Deep Space Network
<b>DSS</b>	Deep Space Station
<b>ECEF</b>	Earth-Centered Earth-Fixed
<b>ECI</b>	Earth-Centered Inertial
<b>ERT</b>	Earth Received Time
<b>ESA</b>	European Space Agency
<b>ESTRACK</b>	ESA Tracking Stations Network
<b>ET</b>	Ephemeris Time
<b>GMT</b>	Greenwich Mean Time
<b>GPS</b>	Global Positioning System
<b>GRV</b>	GRaVity
<b>GSE</b>	Gravity Science Enhancement
<b>HEA</b>	High Efficiency Antenna

<b>IAU</b>	International Astronomical Union
<b>ICRF</b>	International Celestial Reference Frame
<b>IERS</b>	International Earth Rotation Service
<b>ITRF</b>	International Terrestrial Reference Frame
<b>JPL</b>	Jet Propulsion Laboratory
<b>LITS</b>	Linear Ion Trap Standard
<b>LOS</b>	Line Of Sight
<b>MONTE</b>	Mission-analysis, Operations, and Navigation Toolkit Environment
<b>MWR</b>	Micro-Wave Radiometer
<b>ODP</b>	Orbit Determination Program
<b>OWLT</b>	One-Way Light Time
<b>PLL</b>	Phase-Locked Loop
<b>PN</b>	Pseudo-random Noise
<b>RMS</b>	Root Mean Square
<b>RTTT</b>	Round-Trip Transit Time
<b>RTL</b>	Round-Trip Light Time
<b>RU</b>	Range Units
<b>SCET</b>	SpaceCraft Event Time
<b>SEP</b>	Sun-Earth-Probe angle
<b>SNR</b>	Signal to Noise Ratio
<b>SOS</b>	Sum Of Square
<b>SRA</b>	Sequential Ranging Assembly
<b>SRP</b>	Solar Radiation Pressure
<b>ST</b>	Station Time
<b>SVD</b>	Singular Value Decomposition
<b>TAI</b>	International Atomic Time
<b>TDB</b>	Barycentric Dynamical Time
<b>TEC</b>	Total Electron Count

<b>TSAC</b>	Tracking System Analytical Calibration
<b>TWLT</b>	Two-Way Light Time
<b>USO</b>	Ultra-Stable Oscillator
<b>UTC</b>	Coordinated Universal Time
<b>UT</b>	Universal Time
<b>VLBI</b>	Very Long Baseline Interferometry
<b>WVR</b>	Water Vapour Radiometer



# Chapter 1

## Introduction

### 1.1 The Cassini-Huygens Mission

Cassini-Huygens is a joint NASA/ESA/ASI interplanetary mission with the primary goal to conduct an in-depth exploration of the Saturn's system. NASA supplied the Cassini orbiter, ESA supplied the Huygens Titan probe, and ASI provided hardware systems for the orbiter as well as instruments for both the orbiter and probe. The primary goal of Cassini is to conduct an in-depth exploration of the Saturn system. The orbiter was named after the Italian astronomer Giovanni Domenico Cassini (1625-1712), who discovered the Saturn's satellites Iapetus, Rhea, Dione and Tethys, and who firstly noted rings features such as the Cassini division. The probe was named after the dutch astronomer Christiaan Huygens (1629-1695), who discovered the first moon of Saturn, Titan, using a self-made telescope.

Being visible to the naked eye, Saturn is known since the ancient times. Saturn is the second most massive planet in the Solar System, and its system is one of the most complex and extraordinary planetary systems known. It is composed by:

- The planet Saturn itself, with its atmosphere, gravity field, magnetic field.
- Titan, the biggest moon of Saturn, the second in the solar system.
- The icy satellites, among which Enceladus, Dione and Rhea are the most important.
- The rings system, the largest and most developed in the solar system.
- The Saturn magnetosphere.

Cassini is studying the present status of each element, the processes operating on or in them, and the interactions between them, on short and large time scales, allowing to characterize also the seasonal variations during almost half of the 30-year Saturn revolution period.

Our understanding of the Saturn system has been greatly enhanced by the Cassini-Huygens mission. Fundamental discoveries have altered our views of Saturn, Titan and the icy moons, the rings, and magnetosphere of the system.

### 1.1.1 The Scientific Objectives

In this section an overview of the scientific objectives of the Cassini-Huygens mission is provided, for each element of the Saturn system [44].

**Titan** Titan is the major focus of the mission. It is studied by both the Cassini orbiter and the Huygens probe. Second for dimensions, Titan has the thickest atmosphere among the satellites in the Solar System. Moreover, Titan is the only object in the solar system other than Earth that sustains an active hydrological cycle with surface liquids, most liquid methane and ethane, meteorology, and climate change. It possesses methane-ethane lakes and seas, fluvial erosion, and equatorial dunes shaped by winds and formed of organic particles derived from methane. The main scientific objectives related to Titan of the mission are:

- Determine the composition of the atmosphere, constraining scenarios of the formation and evolution of Titan and its atmosphere.
- Characterize the atmosphere, chemically, energetically, measuring winds and global temperatures, and observing the seasonal effects.
- Determine the topography and surface composition.
- Infer the internal structure of the satellite.
- Investigate the upper atmosphere, and its role as a source of neutral and ions materials for the magnetosphere of Saturn.

**Icy Satellites** Saturn has a large number of satellites, with sizes varying from several km to hundreds of km. As satellites become smaller they approach the size of ring particles. Some of the smaller icy satellites are embedded into the rings and interact with them creating complex and fascinating patterns. Among the icy satellites, the Cassini's discovery of ongoing endogenic activity of Enceladus was extremely important- The Cassini scientific objectives specific to the icy satellites are:

- Determine the general characteristics and geological histories of the satellites.
- Define the mechanisms, both external and internal, responsible of crustal and surface modifications.
- Investigate the composition and distribution of surface materials.
- Constrain models of the satellites bulk composition and internal structures.
- Investigate interactions with the magnetosphere and ring system, as possible sources or sink of neutral and ion particles.

**Magnetosphere** The scientific objectives specific to magnetospheric and plasma science are:

- Determine the configuration of the nearly axial symmetric Saturn magnetic field.
- Determine the composition, sources and sinks of magnetosphere charged particles.
- Investigate interactions between the magnetosphere, the solar wind, the satellites and the rings.

**Saturn's Ring System** Saturn has by far the best-developed ring system in the Solar system. The main scientific objectives related to rings are:

- Study ring configuration and dynamical processes.
- Map composition and size distribution of ring materials.
- Investigate correlation between rings and satellites.
- Study interactions between the rings and Saturn's magnetosphere, ionosphere and atmosphere

**Saturn** Saturn is a gas giant planet with a mass of about 95 Earth's masses. The main scientific objectives specific to Saturn are:

- Determine temperature and composition of the atmosphere.
- Measure winds and observe wind features.
- Infer the interior structure of Saturn.
- Study the Saturn's ionosphere.
- Provide observational constraint on scenarios for the formation and evolution of Saturn.

### 1.1.2 The Cassini Mission

Cassini was launched on October 15, 1997 using Titan IV-B rocket, in a configuration with two solid-rocket boosters and a Centaur upper stage. The launcher put Cassini into Earth's orbit and then the upper stage provided the necessary delta-v to inject it into its interplanetary trajectory. During its seven years cruise to Saturn, four gravity assists were employed to increase the spacecraft velocity and allow reaching Saturn: two Venus flybys (26 April 1998 and 24 June 1999), an Earth flyby (18 August 1999) and a Jupiter flyby (30 December 2000). For 6 months around the Jupiter gravity assist, performed at about  $137 R_J$ , scientific observations of Jupiter system were conducted. This served also as a test for Saturn later observations. For the first time, joint observations of an outer planet with two

spacecrafts were performed: in fact, at that time Galileo was carrying out scientific observations of Jupiter, since its arrival in 1995.

Cassini arrived at Saturn on 1 July 2004, roughly after 2 years the planet's northern winter solstice. The Saturn Orbit Insertion maneuver provided a total delta- $v$  of about 633 m/s, for a duration of 97 minutes, and marked the beginning of the Saturn tour phase. On December 23, 2004, the Huygens probe was released into Titan's atmosphere. After more than 70 orbits around Saturn and 45 Titan's fly-bys Cassini completed the 4 year prime mission in July 2008, returning a tremendous amount of high-quality scientific data. The mission was extended a first time for the 2 year Equinox mission, so named because the spring equinox of Saturn was in August 2009. Being the spacecraft in an excellent health status, the mission was extended a second time for the ambitious 7-year Solstice Mission, still in progress. During this phase, Cassini is continuing to study Saturn and its system, addressing new questions that have arisen during the Prime and Equinox Missions and allowing to characterize seasonal and temporal changes. Moreover, in November 2016 Cassini will start a new phase of the Solstice mission, entering the so-called "proximal orbits", a series of 42 short period, low-pericenter, orbits. The first 20 orbits will have periapses just outside the F ring, and the remaining 22 orbits will have a periapse just inside the D ring. This phase can be considered almost as a completely new mission, dedicated to close observations of Saturn. Moreover it will provide a unique comparison to the very similar Juno observations of Jupiter, planned for the same period. This mission phase would end with the spacecraft ultimately vaporizing in Saturn's atmosphere, with planned impact date on September 15, 2017.

### 1.1.3 The Cassini-Huygens Spacecraft

Cassini investigations are supported by the most capable and sophisticated set of instruments sent to the outer solar system [44].

The Cassini-Huygens spacecraft is represented Figure 1.1. It is made of several sections, from top to bottom [29, 44]:

- The High Gain Antenna (HGA)
- The electronic bus, with 12 bays housing the majority of the spacecraft electronics.
- The upper equipment module.
- The propellant tanks with the engines.
- The lower equipment module.

Until its release in December 2004 attached on one side there was the three-meter diameter Huygens probe. A 11 m boom supports the Magnetometer (MAG). Three thin 10 m antennas pointing in orthogonal directions are the sensors of the Radio and Plasma Wave Science (RPWS) experiment. Three Radio-isotope Thermal Generators (RTG) provides electrical power through the decaying of an isotope of

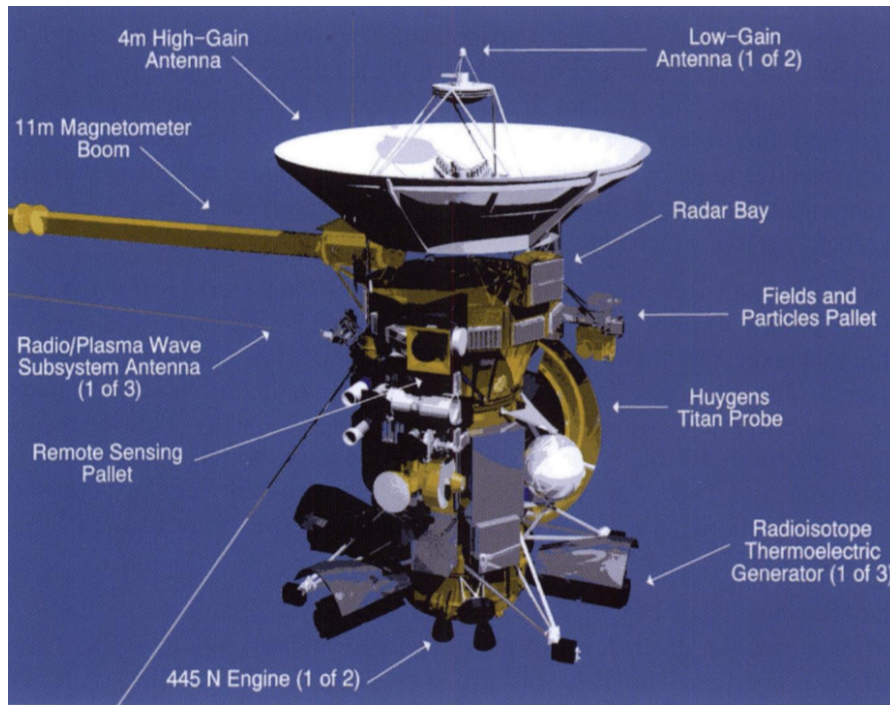


Figure 1.1: The Cassini-Huygens spacecraft in cruise configuration.

Plutonium (Pu-238). The heat generated by this natural process is converted into electrical power by solid-state thermoelectric converters, without any moving part.

Cassini is three-axis stabilized spacecraft. The attitude can be controlled either using the reaction wheels of a set of small thrusters. The instruments are body-fixed, so the observations require pointing the whole spacecraft. For this reason, during the scientific observations the HGA cannot be used to communicate to the Earth, either for transmit the telemetry or for gravity radio science experiments. The data are recorded on two solid-state recorders (SSR), each of which has a storage capacity of about 2 Gigabits. Due to the effects of solar and cosmic radiation the actual storage capacity decreased with time.

The Cassini-Huygens system carries 18 instruments, 12 on the orbiter Cassini and 6 on the Huygens probe. Most of the orbiter instruments are on two body-fixed platforms, the remote-sensing platform and the particles-and-fields pallet.

A brief description of the Cassini instruments follow [44]:

- Composite Infrared Spectrometer (CIRS): it consists of dual interferometers that measure infrared emission to determine the composition and temperatures of atmospheres, rings, and surfaces.
- Imaging Science Subsystem (ISS): it consists of both a wide angle camera and a narrow angle camera.
- Ultraviolet Imaging Spectrograph (UVIS): the instrument measures the views in ultraviolet spectrum.
- Visual and Infrared Mapping Spectrometer (VIMS): it consists of spectrometers observing in visual and infrared spectra.

- Cassini Plasma Spectrometer (CAPS): it measures the flux of ions and electrons.
- Cosmic Dust Analyzer (CDA): it measures directly the physical properties of the particles in the Saturn system.
- Ion and Natural Mass Spectrometer (INMS): it measures the composition of neutral and charged particles in Saturn system through mass spectroscopy.
- Dual Technique Magnetometer (MAG): it measures the Saturn magnetic field, its variation with time and interactions with the solar wind.
- Magnetospheric Imaging Instrument (MIMI): it measures the composition, charge state and energy distribution of energetic ions and electrons of the Saturn's magnetosphere.
- Radio and Plasma Wave Science (RPWS): it measures the electric and magnetic fields and electron density in the Saturn system.
- Radar (RADAR): it uses the HGA to study the surface composition and properties of bodies of the Saturn's system. In particular it allows to study the surface of Titan, which is covered by a thick atmosphere layer, opaque in the visible spectrum.
- Radio Science Subsystem (RSS): it studies the compositions of Saturn and Titan atmospheres and ionosphere, the rings structure and the gravity field of Saturn and its satellites.

### 1.1.4 The Cassini Radio Science Subsystem

In this section the Cassini Radio Science Subsystem will be described in details.

#### 1.1.4.1 Scientific Objectives

During the entire Cassini mission, the following radio science experiments were performed:

- Gravitational Wave Experiments (GWE), to detect the Doppler shift due to low-frequency gravitational waves.
- Solar Conjunction Experiments (SCE), to test the general relativity and study the solar corona.
- Ring occultation experiments.
- Atmospheric and ionospheric occultation experiments, for Saturn and Titan.
- Gravitational field experiments, to measure the gravity field of Saturn, Titan and the other icy satellites.

### 1.1.4.2 Overview

The radio science instrument is peculiar because it is not confined within the spacecraft, but it is composed by a ground segment and a spacecraft segment, which in turn is distributed among several spacecraft subsystems. Actually, the radio science subsystem can be considered as a solar-system-sized instrument observing at microwave frequencies, with one end at the spacecraft and the other end at DSN station on Earth [28].

The instrument operates in three fundamental modes:

- Two-way mode: the ground station generates one or more uplink signals, at either X-band and Ka-band, using as reference the local frequency and timing system. The signals are amplified, radiated through feed horns and collimated by a large parabolic antenna. The uplink frequency can be constant (unramped) or linearly variable with time (ramped) to compensate for the main Doppler shift due to the spacecraft-station relative motion. The spacecraft receives the uplink signals with the High Gain Antenna (HGA), or the Low Gain Antennas (LGA), lock the carrier through the transponder, generates one or more downlink signals that are coherent to the uplink carriers, using the uplink carriers as reference. To prevent interferences, the frequency of the downlink and uplink signals are different. The ratio between downlink and uplink frequencies is called turn-around ratio. The downlink signal is amplified, collimated and sent back to the earth where it is received, amplified and registered by a ground station. Three types of links can be generated:
  - X/X: a X-band downlink signal is generated using the X-band uplink as reference. The turn around ratio is 880/749.
  - X/Ka: a Ka-band downlink signal is generated using the X-band uplink as reference. The turn around ratio is 3520/749.
  - Ka/Ka: a Ka-band downlink signal is generated using the Ka-band uplink as reference. The turn around ratio is 14/15. At present this link is not available anymore, due to a unrecoverable failure of the KaT transponder.

The use of the three links at the same time allows a complete calibration of dispersive media, like solar plasma and earth ionosphere, using the full multi-frequency link combination [12, 42]. At present, being the KaKa link unavailable, this calibration method cannot be used, limiting the accuracies achievable by the experiments.

- Three-way mode: this mode is the same as two-way mode, but the transmitting and receiving ground station are different. Three-way mode is widely used when the geometric configuration do not allow continuous tracking from the same antenna.
- One-way mode: in this operative mode the source of the signal is the spacecraft. The Ultra-Stable Oscillator (USO) is used as reference to generate one or more downlink signals, at S-, X-, and Ka- bands. These signals are amplified

and radiated through the HGA toward Earth. After passing through the medium of interest (atmosphere, ionosphere, or rings) the perturbed signal is received and recorded by a ground station.

Two-way mode allows to achieve the greatest signal stabilities, because it exploits the greater stability of the ground reference frequency to achieve a signal much more stable. Currently, the DSN frequency standard is based upon a Hydrogen Maser Oscillator, which provides a very accurate frequency reference at the time scales of interest. Typical Allan deviations of the ground clock are of the order of about  $10^{-15}$  at 1000 s of integration time. As reference, the Allan deviation of the Cassini USO is about  $3 \times 10^{-13}$  at 1000 s of integration time.

#### 1.1.4.3 Spacecraft Segment

The Radio Science Subsystem is a virtual subsystem composed by the elements from three spacecraft subsystems:

- Radio Frequency Subsystem (RFS).
- Radio Frequency Instrument Subsystem (RFIS).
- Spacecraft Antennas.

**The Radio Frequency Subsystem** The Radio Frequency Subsystem (RFS) is a critical, redundant, spacecraft subsystem which supports spacecraft telecommunications, allowing the spacecraft to receive commands and transmit telemetry at X-band. The components of the RFS involved in the RSS are:

- The Ultra-Stable Oscillator (USO).
- The Deep-Space Transponders (DSTs).
- The X-band Traveling Wave Tube Amplifiers (X-TWTAs).

The RFS has three operative modes:

- Two-way coherent mode: the receiver in the DST locks the uplink carrier, which is used as a reference to generate a coherent downlink signal.
- Two-way non-coherent mode: the uplink carrier is locked into the DST, but the downlink signal is generated using as reference either the USO or the DST auxiliary oscillator.
- One-way mode: in this mode there is no uplink, and a downlink signal is generated using either the USO or the DST auxiliary oscillator.

The DST generates also the input signals for the S-band transmitter (SBT) and the Ka-band exciter (KEX) in the RFIS. Either the USO or the uplink signals can be used.

Cassini's USO is a crystal oscillator whose internal temperature is maintained constant to within 0.001 K by a proportionally controlled oven. The USO generates

a 114.9 MHz reference signal with exceptional short-term phase and frequency stability for the DST, SBT, and KEX.

The X-band downlink generated from the DST is amplified by the X-TWTA to 15.8 W, and radiated to Earth through the spacecraft antennas.

**The Radio Frequency Instrument Subsystem** The elements of the RFIS are devoted exclusively to radio science:

- S-Band Transmitter (SBT): it generates a 13.5 W 2.3 GHz (S-band) carrier from a 115 MHz input signal from the DST. The input signal can derive directly from the USO or can be generated coherently from the uplink signal. The S-band carrier is sent through a diplexer to the HGA.
- Ka-band EXciter (KEX): it generates a Ka-band 32 GHz carrier from both a 115 MHz and a X-band inputs from the DST. These inputs can be generated from the USO (in one-way mode) or coherently from the uplink (in two-way mode). The output is routed through a hybrid coupler to the K-TWTA.
- Ka-band Transponder (KAT): it generates a  $32 \text{ GHz}$  downlink signal coherently from a  $34 \text{ GHz}$  uplink signal, using a turnaround ratio of 14/15, with an intrinsic Allan deviation of  $3 \times 10^{-15}$  at 1000 s. integration time. The KAT output goes through the hybrid coupler and then to the K-TWTA.
- Ka-band Traveling Wave Tube Amplifier (K-TWTA): it amplifies the Ka-band output from both the KEX and the KAT, singly or simultaneously, feeding the HGA only. The amplifier produces a total output power of 7.2 W when operating with one carrier and 5.7 W in dual-carrier mode.

The SBT and KAT were funded by the Italian Space Agency (ASI) and produced by Thales Alenia Space Italy (formerly Alenia Spazio) as part of the Italian participation to the Cassini mission. Alenia Spazio also integrated and tested the RFIS.

**Orbiter Antennas** Cassini has one High-Gain Antenna (HGA) and two Low-Gain Antennas (LGA1 and LGA2) [63].

- The HGA is Cassegrain system, with a 4 m diameter parabolic primary reflector. The HGA is body-fixed with its boresight along the spacecraft  $-Z$  axis and is pointed by moving the spacecraft. In addition to supporting X-band telecommunications, the HGA supports the S-band, X-band and Ka-band radio science links, and serves as the transmit and receive antenna for the Cassini Radar, at Ku-band. It is the most complex antenna ever flown on a planetary spacecraft.
- The LGAs sacrifice gain to provide a relatively uniform coverage. They are used when the HGA can't be pointed toward the Earth, due to thermal constraints or when the spacecraft is in safe mode. LGA1 is mounted on top of the HGA and points along  $-Z$  axis, as the HGA, while LGA2 is

mounted on a boom below the Huygens Probe, and pointing along the  $-X$  axis. The LGAs can operate at X-band only. Recently, a test to use LGA for radio science gravity experiments was performed [11]. The test assessed the feasibility to perform precise orbit determination using the LGAs, making it possible to collect data also during satellites fly-bys not dedicated to gravity investigations, at the expense of a small degradation of the signal-to-noise ratio.

Carrier signals transmitted between the spacecraft and the ground are all circularly polarized. X-band uplink and downlink signals can be either Right-hand Circularly Polarized (RCP) or Left-hand Circularly Polarized (LCP). During normal operations the received and transmitted signals have opposite polarizations. The Ka-band uplink is only LCP, and the Ka-band downlink is only RCP.

#### 1.1.4.4 Ground Segment

The ground segment of the Cassini radio science subsystem is composed by the ground stations and facilities of the NASA's Deep Space Network (DSN). The DSN is composed by three complexes separated in longitude by about 120 deg, to provide a near-global coverage during the diurnal Earth rotation. The complexes are located near Goldstone, in the desert of the Southern California, near Madrid in Spain, and near Canberra in Australia. The first two complexes are in the northern hemisphere, while Canberra is located in the southern hemisphere. Each complex is equipped with several tracking stations of different aperture size and different capabilities, but each complex has at least one 70 m diameter station, one 34 m high-efficiency (HEF) station, and one 34 m beam-wave-guide (BWG) station. While the primary function of the DSN antennas is to send commands and receive telemetry from deep space probes, they are a fundamental part of the radio science instruments, so performances and calibration of the antennas components concur to determine the experiments accuracy. The antennas perform two functions:

- Transmitting function: an uplink signal, at the frequency assigned to the specific spacecraft, is generated using a very stable reference frequency provided by the frequency and timing subsystem. The performance of the frequency and timing subsystem is of order  $10^{-15}$  for integration times of 1000 s. The uplink frequency can be constant (unramped) or linearly varying with time (ramped). The DSN can transmit at S-, X- or Ka-bands depending on the transmitting station and the receiving spacecraft. The transmitted frequencies are recorded for post-processing of the two-way Doppler observable.
- Receiving function: the large parabolic primary reflector collect the incoming energy of the spacecraft downlink signals and focus it onto the feed horns. The received signal is amplified through low-noise amplifiers, then it is down-converted and routed to the receivers. These two processes define the most important contribution of the ground segment electronics to the overall noise budget of radio science experiments. Two types of receivers can be used:
  - Closed-loop receiver, also called Block V Receiver (BVR): it estimates parameters such as phase and amplitude in real time with standardized

values of receiver bandwidths and time constants. It is the primary DSN receiver for telemetry and tracking data. The signal is phase locked and demodulated from the telemetry and ranging signals. The tracking subsystem measures Doppler shifts and ranging information based on the closed-loop receiver output.

- Open-loop receiver, also called Radio Science Receiver (RSR): it record the electric field of the received signal downconverting and digitizing a selected bandwidth of the spectrum centered around the carrier signal. The RSR had several advantages with respect to the BVR:
  - \* More flexibility because the data (amplitudes and phases) are computed in post-processing.
  - \* Better performances due to more stringent requirements on amplitude, frequency and phase noise stability.
  - \* Simultaneous handling of signals in two polarization states.

**Media Calibration System** The Earth's troposphere is one of the most relevant noise contribution to the overall noise budget of the orbit determination process [9, 27, 34]. The neutral particles of the atmosphere introduce a phase and a group delay in the signal. The main contribution is represented by the gases in the lower part of the atmosphere, in particular the water vapor. Being a non-dispersive media, the group and phase delay are the same. In order to provide a continuous troposphere calibration a system based on GPS observation has been developed by JPL. The system, named Tracking System Analysis Calibration (TSAC) uses the GIPSY-OASIS II software to create continuous calibration of the Zenith Total Delay (ZTD). The delay along the line of sight of the spacecraft is obtaining scaling the ZTD with mapping functions.

In order to achieve the unprecedented accuracies needed by the Cassini's cruise radio science experiments, a new generation of media calibration system, called Advanced Media Calibration system (AMC), was developed [10, 52, 57, 58]. The AMC includes different meteorological instruments to retrieve the entire troposphere delay:

- A high-stability Water Vapor Radiometer (WVR), which senses the number of water vapor molecules along the line of sight.
- A Microwave Temperature Profiler (MTP), which senses the vertical temperature distribution.
- A Surface Meteorological station (SM), which measures the temperature, pressure and humidity.

The AMC system provides the most accurate calibration of the tropospheric noise to date, because it is capable to measure with very good accuracy the high-frequency scintillations of the tropospheric path delay due to variation of water vapor content along the line of sight.

## 1.2 The Orbit Determination Problem

### 1.2.1 Introduction

This Section provides a high-level description of the procedures to be implemented in order to correctly analyze Doppler data acquired during gravity radio science experiments on interplanetary missions. This analysis is strictly linked to the problem of orbit determination of interplanetary spacecraft. The orbit determination process is an iterative estimation procedure based upon the comparison between the measured observables (observed observables) and the corresponding computed values (computed observables), computed on the basis of mathematical models. The difference between the observed and the computed observables are called residuals. The aim of the orbit determination process is the estimation of a set of parameters (solve-for parameters) that unambiguously define the trajectory of a spacecraft. The orbit determination solution is composed by the value of the solve-for parameters that minimizes, in a least square sense, the residuals, and by the corresponding covariance matrix that defines the formal uncertainty of the solution. For Deep Space navigation purposes, the orbit determination S/W is typically used to analyze large data sets and estimate a large number of solve-for parameters, with the aim of providing the best estimate of the S/C state, for the need of both S/C operations and scientific data analysis. On the other hand, for radio science applications, typically small data sets acquired during the limited time intervals of dedicated experiments are analyzed in the orbit determination S/W, aiming at the estimation of a restricted set of parameters (in addition to the S/C state vector) that defines the gravity field of celestial bodies. These experiments are carefully designed in order to minimize the uncertainties in the orbit determination process and to maximize the Signal to Noise Ratio of the solve-for parameters. For gravity radio science experiments the solve-for parameters may include:

- coefficients of the gravity spherical harmonics expansion of a celestial body;
- Love's numbers, the define the gravity field response to external tidal effects;
- Rotational parameters of a celestial body.

The gravity field, and so the gravitational acceleration of the spacecraft, are a consequence of the planet/satellite internal composition and mass distribution, so the experiments results can be used to develop and test models of the origin, evolution and structure of celestial bodies, like planets, satellites and asteroids. Moreover the experiments can be used to test the general relativity, measuring relativistic effects like the Shapiro light-time delay or the Lense-Thirring effect.

The orbit determination process can be divided into five main steps:

- Pre-processing of radiometric measurements.
- Computation of radiometric observables and partial derivatives with respect to the solve-for parameters, using mathematical models.
- Observables and partial derivatives computation.

- Estimation filter.
- Solution analysis.

Because of the intrinsic non-linearity of the problem, these steps are usually repeated until convergence is reached. In the first iteration the observables and partials are computed using apriori values of the solve-for parameters. The estimation filter computes differential corrections to these values, on the basis of comparison between computed and observed observables. In the next iterations the observables are computed using the solution of the previous iteration for the solve-for parameters.

In the following each of these steps will be described from an operational point of view. For more details about the modelization of all the physical effects, see [51] and [54].

### 1.2.2 Pre-processing of radiometric measurements

During the pre-processing phase the radiometric observables are prepared for the orbit determination process. The most important Earth-based radiometric observables are:

- range: measured round-trip light time, in range units.
- Doppler: frequency shift of the carrier of the received signal.
- DDOR: angular measurement of the S/C along a baseline formed by two ground stations.

On these data, one or more of the following actions may be performed before the analysis:

- Apply the calibrations to correct intrinsically not predictable effects that could affect the measurements, like:
  - group delay due to electronics in ground stations and spacecraft;
  - group and phase delay due to propagation media, like troposphere, ionosphere and interplanetary plasma;

The calibrations are computed and provided by JPL.

- Compute received sky frequencies from open-loop recordings.
- Compute synthetic non-dispersive observables, if a multi-frequency link is available.
- Delete macroscopic invalid data (outliers). Typically up to 20% of the data may be removed in this phase.

### 1.2.3 Observables and partials computation

During this phase, the radiometric measurements are simulated using mathematical models of all physical effects that affect, in a not-negligible way, their values. The parameters that define the mathematical models can be divided into three categories:

- **Solve-for parameters:** not exactly known parameters that affect data and whose current estimate can be improved through the orbit determination process. At the first iteration their a priori values and uncertainty are used, obtained from the best measurements or theoretical estimations available to date. In the next iterations the solution obtained at the previous iteration is used. The solve-for parameters should always include the initial state of the spacecraft.
- **Consider parameters:** not exactly known parameters that affect data and whose current estimate cannot be improved through the analysis. Their best estimate to date must be used in the mathematical models, together with their uncertainties. The orbit determination filter does not change the consider parameters, but their uncertainty increases the solution covariance matrix.
- **Exact parameters:** parameters that are theoretically exactly known or whose uncertainty does not affect the estimation, because it is small with respect to their influence on measurements data.

Moreover, during this phase, also the partial derivatives of the observables with respect to the solve-for and consider parameters are computed. They are used to obtain the new estimate of the value of solve-for parameters and their covariance matrix.

The observables and partials computation is performed through the following procedures:

- Planetary and/or Satellite ephemerides update;
- Integration of equations of motion and variational equations;
- Time transformations;
- Ground Station state computation;
- Light-time solution computation;

#### 1.2.3.1 Planetary and/or Satellite ephemerides update

The spacecraft trajectory and the radiometric measurements depend on the gravity fields of nearby celestial bodies and relative positions between the spacecraft and celestial bodies. Hence, depending on the type of radiometric observables and geometry of the observation, to correctly extract the information content from the measurements should be necessary to estimate also the planetary and/or satellite ephemerides. For example, during gravity radio science experiments of

planetary satellites, the spacecraft trajectory and so the Doppler data are affected in a not-negligible way by the gravitational fields of both the planet and the satellite. So, the measurements are sensitive to the relative positions and velocities of the spacecraft, the satellite, and the planet. Hence, the orbit determination fit shall estimate both the planetary state of the spacecraft and of the satellite. As another example, the orbit of Mercury is heavily affected by relativistic effects. Accurate range measurements from a Mercury orbiter can be used to test the validity of the Einstein's general relativity, for example through the estimation of the Parameterized Post-Newtonian parameters  $\gamma$  and  $\beta$ . This requires the capability to update the planetary ephemerides of Mercury. At the first iteration of the orbit determination process the most updated ephemeris available at date are used, while in the next iterations the ephemerides should be updated using the estimate of the previous iteration. Ephemerides are generated integrating the full relativistic equations of motion of the planets from their initial states. The partials needed to update the ephemerides are obtained integrating the variational equations for the planetary/satellite state.

### 1.2.3.2 Integration of equations of motion and variational equations

The next step to compute the radiometric observables and partials is to reconstruct the spacecraft trajectory integrating the equations of motion with respect to a reference point (Center Of Integration, COI) from an input initial state. The a priori value (and uncertainty) of the initial state is usually given by the mission navigation team. To correctly reconstruct the spacecraft trajectory all non-negligible accelerations acting on the spacecraft and on the COI must be correctly modeled. The most important accelerations that may influence the spacecraft state are:

- Point-mass Newtonian gravitational acceleration due to the Sun, the planets, Pluto, small bodies, as asteroids and comets, the Moon and all satellites of a planetary system.
- Point-mass relativistic perturbative gravitational acceleration due to the Sun, the planets, Pluto and the Moon.
- Acceleration due to Geodesic precession.
- Acceleration due to Lense-Thirring precession.
- Newtonian acceleration due to the gravitational spherical harmonics of all the planets, Pluto, small bodies, as asteroids and comets, the Moon and all satellites of a planetary system. The acceleration of the S/C relative to the COI due to oblateness of one of the bodies listed above is computed as the acceleration of the S/C (direct component) minus the acceleration of the COI (indirect component). If also the COI is an oblate body, the acceleration of the COI is the sum of two terms:
  - the acceleration due to the spherical harmonics of the oblate body on the point-mass COI;

- the acceleration due to the point-mass oblate body on the COI's oblateness.

The acceleration due to the interaction between the oblateness of the body and the COI is neglected.

- Relativistic acceleration due to the gravitational spherical harmonics: this effect is usually considered only for the Earth's gravity field on a near-Earth S/C.
- Accelerations caused by tidal effects on the physical central body: the acceleration of the S/C derives from corrections to the central body's normalized harmonic coefficients due to the tides as:
  - solid tides;
  - ocean loadings;
  - pole tides.
- Gravitational acceleration due to planetary rings.
- Gravitational acceleration due to mascons.
- Solar radiation pressure;
- Planetary radiation pressure: acceleration due to the radiation emitted from the surface of a planet, both reflected visible light (albedo) and thermal emission.
- Thermal imbalance: acceleration due to non-uniform surface heating.
- Gas leakage: acceleration due to control jets leakage.
- Atmospheric drag.
- Maneuvers.

To compute the various contributions to the total spacecraft acceleration the position of the celestial bodies must be known, through planetary, satellite and small bodies ephemerides. At present the most accurate celestial ephemerides are provided by NASA/JPL, eventually updated in the previous step of the orbit determination process.

### 1.2.3.3 Time transformations

All radiometric observables measured at different tracking stations on the Earth are referred to the time measured by the station clock. Apart from a small drift due to clock stability, the station reference time is equal to UTC. However, to correctly compute the light-time solution, time must be expressed in Barycentric Coordinate Time (TCB), the coordinate time of the relativistic equations of motion in the Solar

System barycentric space-time frame of reference or in a linear transformation of TCB, like JPL Ephemeris Time ( $T_{eph}$ ) or Barycentric Dynamical Time (TDB)<sup>1</sup>.

#### 1.2.3.4 Ground station state computation

The location of a ground station is conventionally defined as the position of a reference point. The station's coordinates are given as inputs in a terrestrial reference frame, then the station location must be corrected to account for various effects:

- Solid Earth tides: the tides caused by the Moon and the Sun produce deformations of the Earth that change the location of the ground station. At least first order displacements and second order corrections due to a tidal potential of degree two due to both the Moon and the Sun must be considered. The first order displacement is about 50 cm, while the second order correction is about 13 mm. Usually the permanent tidal displacement is included in the expression of the first-order displacement, so the coordinates of the tracking stations must not include it. At present, terms less than 5 mm can be neglected.
- Ocean loadings: periodic displacements due to the periodic ocean tides. The displacements are less than 4 mm.
- Pole tide: the polar motion modifies the centrifugal potential of the Earth and caused a solid tide that produces a displacement of the tracking station. The displacement is less than 2 cm.
- Plate motion: a tracking station has a non zero velocity due to the tectonic plate motion. The station velocity due to plate motion can be up to 10 cm/y.
- Offset between the real COM of the Earth and the origin of the considered terrestrial reference frame.

Next, in order to solve the light-time problem it is necessary to convert the station location from the terrestrial reference frame to the celestial reference frame. The transformation between the two reference frames consists of a series of rotations:

- polar motion;
- Earth rotation;
- nutation;
- precession.

---

<sup>1</sup>Since JPL's DE430, the Ephemeris Time  $T_{eph}$  coincides with Barycentric Dynamical Time TDB, that is a defined linear transformation of TCB. For the older ephemerides  $T_{eph}$  is formally different from TDB, because it was computed as a part of the ephemerides estimation to remove a linear drift with the Terrestrial Time (TT). However, this difference at present is completely negligible.

These rotations are defined by a set of parameters, that depend on the particular modelization selected. An internal group at NASA/JPL provides the so-called Earth Orientation Parameters (EOP), that define these rotations according to IAU 1980 Theory of nutation and the IAU 1976 Precession Model. As an alternative, the more accurate IAU 2000 Model can be used. The coefficients defining the rotations are provided either by JPL or by IERS website<sup>2</sup>. After these rotations the geocentric state of the tracking station is expressed in the Geocentric space-time frame of reference, and it must be referred to Solar System barycentric space-time frame of reference, through proper Lorentz transformations.

### 1.2.3.5 Light-time solution computation

The next step to evaluate the computed value of a measured quantity is to obtain the solution of the light-time problem for that observable. The light-time solution consists of the epoch of participation and the state of each direct participant at its epoch of participation. The direct participants of the light-time problem and the times of participation are:

- the receiving station at the reception time  $t_3$ ;
- the S/C at the reflection time (for two-way or three-way observables) or transmission time (for one-way observables)  $t_2$ ;
- the transmitting station at the transmission time  $t_1$  (only for two-way or three-way observables).

In the orbit determination process, the reception time of an observed quantity is known, so it is necessary to solve the light-time problem to compute the reflection time and the transmission time. The light-time problem is based upon the expression of the time for light to travel from the transmitter to a receiver. This time is the sum of two components:

- Newtonian light-time, that represents the time for light to travel along a straight-line path at the speed of light  $c$ .
- The relativistic light-time delay, also called Shapiro effect, that accounts for the reduction of the coordinate velocity of light below  $c$  and the bending of the light path due to presence of a gravity field that curves the space-time.

### 1.2.3.6 Observables computation

The outputs of the light-time problem are used to compute the value of radiometric observables measured at Earth tracking stations. Moreover, the partial derivatives of the observables with respect to the solve-for parameters are computed. The model of the radiometric observables obtained at the stations of the Deep Station Network (DSN) and the corresponding partials are described in [51].

---

<sup>2</sup><http://www.iers.org/>

### 1.2.4 Estimation Filter

The estimation filter computes the value of the solve-for parameters that minimize, in a least square sense, a combination of the following quantities:

- Residuals between the observed and computed observables. The residuals should be weighted with their measurements noise. However, because noise is not known, as a start to the analysis an a-priori value is used, on the basis of available theoretical error budgets or experience. In the next analysis the measurements noise is estimated as the residuals' standard deviation. Note that this imply the assumption that the measurements noise is white. In the different iterations of the same analysis residuals weights are kept constants.
- Difference between the solve-for parameters and their a priori values. This difference is weighted using the uncertainty of the a-priori information. From a filtering point of view, a priori data are equivalent to additional observations. They are used to increase the numerical stability of the information matrix and facilitate the convergence.

The estimation filter produces two outputs:

- A differential correction to a priori values of the solve-for parameters. It gives the updated estimate of the solve-for parameters.
- The covariance matrix of the solve-for parameters, that represents the solution uncertainty. The a priori covariance matrix is updated on the basis of the influence on the solve-for parameters of the measurements noise and consider parameters uncertainty.

### 1.2.5 Solution Analysis

The solution obtained from the estimation filter should be verified and tested. The following aspects should be analyzed:

- Convergence: the orbit determination process reaches convergence if two (or more) successive iteration steps produce statistically equivalent solutions.
- Residuals analysis: the obtained solution is used to compute residuals. If the orbit determination process was performed correctly solution residuals represent only measurements noise, hence they must verify the following conditions:
  - Zero mean: the residuals mean must be much less than their standard deviation, i.e. compatible with a zero value;
  - Spectrum compatible with the expected noise characteristics;

Moreover, the residuals standard deviation should be compatible with the residuals weight used in the estimation filter.

- Solution covariance matrix analysis:

- Comparison between a priori and computed formal uncertainties: a parameter is fully observable from data if the computed uncertainties are much less than the a priori ones (as reference a factor 10 can be used). Otherwise, the estimation depends much more on a priori information than on radiometric measurements.
- Cross-correlation between solve-for parameters: if two solve-for parameters are largely correlated, their estimation is strictly dependent.
- Comparison between a priori values and the new estimates: the new and old estimate of the solve-for parameters should be statistically compatible.
- Solution stability: to check the solution stability it is useful to make another estimation process using the solution as a priori values, with "relaxed" increased a priori uncertainties. If the solution is sufficiently stable the new estimation will be statistically compatible with the testing solution.

# Chapter 2

## Numerical Noise in Interplanetary Orbit Determination Software

### 2.1 Introduction

The aim of the orbit determination process is the estimation of a set of parameters that unambiguously defines the trajectory of a spacecraft. The core of the process is the comparison between measured observables (“observed observables”) and the corresponding computed values (“computed observables”), obtained by an orbit determination program using the adopted mathematical models. The output of the orbit determination is the values of the parameters, called solve-for parameters, that minimize, usually in a least-square sense, the global difference between the observed observables and the computed observables. For the tracking of deep space probes the use of Earth-based radiometric techniques, especially based on Doppler measurements, is of fundamental importance.

Disturbances in either the observed or computed observables degrades the orbit determination process. The different sources of noise in the Doppler observed observables were the subject of several detailed studies in the past [6–9]. In [9] a detailed noise budget for Doppler tracking of deep space probes was presented; however recent tracking data acquired from the NASA/ESA/ASI Cassini-Huygens mission to the Saturn system showed imperfect quantitative agreement between the measured residual noise [34] and the predictions presented in [9], thus suggesting that there could be additional effects not considered so far, like errors in the Doppler observables computed by the orbit determination program.

In this study the three most important interplanetary orbit determination programs are considered:

- ODP (Orbit Determination Program), developed since the 1960s at NASA’s JPL, and used for navigation in almost all NASA missions controlled by JPL since recent years [15, 66, 67]. At present ODP is not used anymore for operational navigation. However, it is still used in different forms for specific purposes.
- MONTE (Mission-analysis, Operations, and Navigation Toolkit Environment), developed since late 2000s at NASA’s JPL to replace the ODP. After several

years of development and tests, at present it is used for navigation of all the operational missions controlled by JPL.

- AMFIN (Advanced Modular Facility for Interplanetary Navigation), developed at ESA/ESOC and used for the operational navigation of the ESA's interplanetary missions.

The errors in the computed radiometric observables can be divided into two categories:

- Model errors, caused by using incomplete mathematical models for the computation of the observables.
- Numerical errors, that arise from the use of finite-precision arithmetic.

Concerning the model errors, the basis of all the three most important interplanetary orbit determination programs is Moyer's formulation, described in detail in [51]. At present this formulation is considered sufficiently accurate, compared to the present level of noise in the radiometric measurements [48].

Numerical errors are introduced in every real number and computation step because, within a computer, the representation of numbers and the computations have to be performed using a finite number of digits. The resulting errors in the computed observables depend upon the hardware and software representation of numbers, the mathematical formulation of the observables and its implementation in the software. According to Moyer's formulation the two-way (or three-way) Doppler observable is computed as the difference of two round-trip light times between the spacecraft and the tracking station(s), thus it is called differenced-range Doppler (DRD) formulation [49, 50]. AMFIN implements also an older formulation, based upon a truncated Taylor series, called the integrated Doppler (ID) formulation, formerly implemented in the ODP and described in [50]. Moreover, both the ODP and AMFIN are compiled to use double-precision floating point arithmetic [17, 51].

MONTE

An order-of-magnitude estimation of numerical errors in DRD double-precision computed observables is provided in [50] and [49], where it is recommended to use at least 60 bits to represent the significand, also called mantissa, in order to keep a two-way accuracy of  $2 \times 10^{-2}$  mm/s at all integration times. This results in an Allan Standard Deviation (ASDEV) of about  $6.7 \times 10^{-14}$  s/s. However, the observational accuracy of the interplanetary missions has been gradually and continuously improving with time. For example, the current most precise two-way Doppler observations were achieved between the NASA Deep Space Network (DSN) and the Cassini spacecraft, reaching a fractional frequency stability, expressed in terms of ASDEV, of about  $3 \times 10^{-15}$  at 1000 s integration time [6]. Future interplanetary missions, such as ESA's BepiColombo mission to Mercury and NASA's Juno mission to Jupiter, carry radio science instrumentation which, used in conjunction with highly performing ground antennas, is required to reach a two-way fractional frequency stability of  $1.0 \times 10^{-14}$  at 1000 s integration time [23, 32], during most of their operational life. On the other hand, almost all modern computers follow the IEEE-754 standard, which establishes the use of 64 bits for double-precision floating point binary representation, where 52 bits are used for the

mantissa [30], less than the value of 60 recommended by [49]. For these reasons a more detailed study of the numerical noise is necessary to assess its actual impact on the precision of the computed observables, for present-day and future interplanetary missions.

This chapter describes a model of numerical errors in two-way (and three-way) Doppler observables, computed by an orbit determination program that implements Moyer's DRD formulation. In Chapter 2.2 the basic concepts of the floating point representation and arithmetic are introduced, together with the description of a statistical model used to evaluate the single contributions to the numerical error, their propagation and accumulation. An analytical model to predict numerical errors in two-way differenced-range Doppler observables is presented in Chapter 2.3, while the validation of this model is described in Chapter 2.4. In Chapter 2.5, the numerical error model is used to analyze the expected numerical noise for Cassini's and Juno's Doppler tracking data. Then, three different strategies to reduce the numerical noise in the Doppler link are presented in Chapter 2.6. Finally, Chapter 2.7 summarizes the results and presents the conclusions of this work.

## 2.2 The Round-Off Errors

### 2.2.1 The Floating Point Representation

The most used method for representing real numbers in modern computers is the binary floating point representation, based upon the normalized scientific notation in base 2. Using the normalized scientific notation in base 2 a value  $x_0$  is represented using an infinite number of bits  $b_i$ , as:

$$x_0 = (-1)^s (1.b_1^0 b_2^0 \dots b_{t-1}^0 b_t^0 b_{t+1}^0 \dots) \times 2^p \quad (2.1)$$

where:

- $s$  defines the sign of  $x$ :  $s = 0$  for positive values,  $s = 1$  for negative ones.
- $p$  is the base-2 order of magnitude of  $x_0$ .

$p$  can be computed from  $x_0$  using the following relation:

$$p(x_0) = \begin{cases} \lfloor \log_2 |x_0| \rfloor, & \text{if } x_0 \neq 0 \\ 0, & \text{if } x_0 = 0 \end{cases} \quad (2.2)$$

where  $\lfloor a \rfloor$  is the floor function of  $a$ .

Using the binary floating point representation the exact value  $x_0$  is encoded using a finite number of bits, as:

$$x = (-1)^s (1.b_1 b_2 \dots b_{t-1} b_t) \times 2^p \quad (2.3)$$

The first  $t - 1$  binary digits of  $x$  are the same of  $x_0$ :

$$b_i = b_i^0 \quad i = 1, \dots, t - 1 \quad (2.4)$$

$b_t$  is the last represented digit of  $x$  and is called Least-Significant Bit (*LSB*). In the representation of  $x_0$  the maximum value represented by the least-significant bit is:

$$q(x_0) = 2^{p(x_0)-t} \quad (2.5)$$

There are several rounding algorithms that define how to choose  $b_t$ . The most common are:

- Round toward 0, also called “truncation”:  $b_t$  is equal to  $b_t^0$ .
- Round toward nearest, usually simply called “rounding”:  $b_t$  is chosen so that  $x$  is closest to  $x_0$ . If  $x_0$  is halfway to two values there are two approaches:
  - Ties away from zero: the mantissa is rounded to the larger value. Because the mantissa does not contain any information about the sign, if the number is positive it is rounded above, if it is negative it is rounded below.
  - Ties to even: the mantissa is rounded to the even value. Statistically, this occurs in the 50% of the cases, so this rounding algorithm does not introduce a systematic drift.

The most used rounding algorithm is “round toward nearest, ties to even”, because it minimizes the rounding error for a given  $t$  and does not introduce a systematic drift [26]. In what follows, only this algorithm will be considered.

The use of a finite number of digits to represent the mantissa introduces an error. The absolute and relative rounding errors are defined as:

$$\Delta\bar{x}(x_0) \triangleq x - x_0 \quad (2.6)$$

$$\Delta\tilde{x}(x_0) \triangleq \frac{x - x_0}{x_0} \quad (2.7)$$

The maximum absolute value of the absolute error in the representation of a variable  $x_0$  is:

$$\Delta\bar{x}_{\max}(x_0) \triangleq \max |\Delta\bar{x}(x_0)| = \frac{q(x_0)}{2} = 2^{p(x_0)-t-1} \quad (2.8)$$

Hence, the maximum absolute error depends upon the number of digits available for the fractional part of the mantissa  $t$  and the order of magnitude  $p$  of the binary number. Given  $t$ , the maximum error is the same for all values in the range  $[2^p, 2^{p+1})$ .

The maximum absolute value of the relative error, also called machine epsilon or  $\varepsilon$ , is:

$$\varepsilon \triangleq \max |\Delta\tilde{x}(x_0)| = \frac{\Delta\bar{x}_{\max}}{|x_{\min}|} = 2^{-t-1} \quad (2.9)$$

$\varepsilon$  does not depend upon the order of magnitude of the value  $x_0$ , but only upon the number of digits of the fractional part of the mantissa  $t$ .

The IEEE-754 standard defines several basic floating-point binary formats that differ by the number of bits used to encode the sign, the exponent and the fractional part of the mantissa. The most important formats are:

- Binary32, also called single precision.
- Binary64, also called double-precision.
- Binary128, also called quadruple-precision.

Their characteristics are summarized in Table 2.1 [30].

Table 2.1: Characteristics of the most important binary formats defined by IEEE-754

IEEE format		Number of bits				$\varepsilon$
		Total	$s$	$f$	$p$	
Binary32	(Single-Precision)	32	1	23	8	$5.96 \times 10^{-8}$
Binary64	(Double-precision)	64	1	52	11	$1.11 \times 10^{-16}$
Binary128	(Quadruple-Precision)	128	1	112	15	$9.63 \times 10^{-35}$

### 2.2.1.1 The Effect of the Measurement Units

In the floating point representation of physical values, the choice of the unit of measurement affects the rounding error.

Given two proportional values  $x_1$  and  $x_2 = k x_1$ , in general the corresponding maximum representation errors  $\Delta \bar{x}_{\max}(x_2)$  and  $\Delta \bar{x}_{\max}(x_1)$  do not satisfy the same relation of proportionality, because of the presence of the floor function in the definition of  $p$  (Eq. 2.2). The maximum absolute errors are proportional if and only if the absolute value of the scale factor  $k$  is an integer power of the basis of representation:

$$|k| = 2^{n_k}, \quad n_k \in \mathbb{Z} \quad (2.10)$$

In this case:

$$\begin{aligned} p(x_2) &= \lfloor \log_2 |k x_1| \rfloor = \lfloor \log_2 |k| + \log_2 |x_1| \rfloor \\ &= \lfloor n_k + \log_2 |x_1| \rfloor = n_k + \lfloor \log_2 |x_1| \rfloor \\ &= n_k + p(x_1) \end{aligned} \quad (2.11)$$

$$\begin{aligned} \Delta \bar{x}_{\max}(x_2) &= 2^{p(x_2)-t-1} = 2^{n_k+p(x_1)-t-1} \\ &= 2^{n_k} 2^{p(x_1)-t-1} = |k| \Delta \bar{x}_{\max}(x_1) \end{aligned} \quad (2.12)$$

As an immediate consequence, the maximum absolute error in the floating point representation of a specific physical quantity depends upon the adopted unit. For example:

$$\text{LSB}(1 \text{ km}) \simeq 2.22 \times 10^{-16} \text{ km} = 2.22 \times 10^{-13} \text{ m} \quad (2.13)$$

$$\text{LSB}(1000 \text{ m}) \simeq 1.14 \times 10^{-13} \text{ m} \quad (2.14)$$

However, it can be shown that, for a generic scale factor  $k$ , the ratio  $\Delta \bar{x}_{\max}(x_2)/\Delta \bar{x}_{\max}(x_1)$  is still  $|k|$ , when averaged on a large enough interval. Hence, averaging on a large enough interval of values, the maximum absolute error in the floating point representation can be considered not depend upon the chosen unit of measurement.

### 2.2.2 The Statistical Model

The rounding error is a form of quantization error, with the LSB as the quantization step. Hence, it is possible to adopt a statistical model, usually applied to quantization errors, known as uniform quantization error model, or Widrow's model [70]. Using this description, given an exact time function  $x_0(t)$ , the round-off error  $\Delta\bar{x}(t)$  in its numerical representation is modeled as a stochastic process with the following characteristics:

- White.
- Wide-sense stationary.
- Uncorrelated with the represented function  $x_0(t)$ .
- With a Probability Density Function (PDF) uniform:

$$f_{\Delta\bar{x}}(\delta\bar{x}) = \begin{cases} 1/q(x_0), & \text{if } -q(x_0)/2 \leq \delta\bar{x} \leq q(x_0)/2 \\ 0, & \text{otherwise} \end{cases} \quad (2.15)$$

With this model, it is possible to compute the statistical properties of the rounding error:

1. Mean value:

$$E[\Delta\bar{x}(t)] = 0 \quad (2.16)$$

2. Maximum absolute value:

$$\Delta\bar{x}_{\max} = \frac{q}{2} \quad (2.17)$$

3. Variance:

$$\sigma_{\Delta\bar{x}}^2 = \frac{q^2}{12} \quad (2.18)$$

The model is valid if the probability density function and the Characteristic Function (the Fourier transform of the PDF) of the input signal  $x_0(t)$  satisfy the conditions of the Quantization Theorem (QT), stated in [70]. In [61] weaker necessary and sufficient conditions for the QT are provided but in practice, for real-world input signals, the conditions are very restrictive. For example, a sinusoidal signal does not satisfy the QT, but Widrow's model can still be applied with sufficient accuracy if the amplitude of the signal is several times larger than the quantization step [41].

In this work the statistical model was assumed to be valid and this assumption was verified through a detailed analysis of the rounding errors, described in Chapter 2.3.5.

### 2.2.3 Operation Errors

When performing an exact operation  $f(x_0, y_0)$  using floating point arithmetic, the result is affected by two kind of errors with respect to the theoretical value  $z_0$ :

- 1) Propagation error of the rounding errors in the inputs:

$$x = x_0 + \Delta\bar{x}, \quad y = y_0 + \Delta\bar{y} \quad (2.19)$$

If the errors are small enough:

$$\tilde{z}_0 = f(x, y) \simeq f(x_0, y_0) + \frac{\partial f}{\partial x}(x_0, y_0)\Delta\bar{x} + \frac{\partial f}{\partial y}(x_0, y_0)\Delta\bar{y} \quad (2.20)$$

- 2) Additional rounding error: even if the errors in the inputs are zero, the output could be affected by a rounding error. IEEE Standard 754 requires that the result of the basic operations (addition, subtraction, multiplication, division and square root) must be exactly rounded [30], i.e. the operation shall be performed as if it first produced an intermediate result correct to infinite precision, and then that result was rounded to the finite number of digits in use. The rounding on the result  $\tilde{z}_0$  can be represented by the addition of the random variable  $\Delta\bar{z}$ :

$$z = \tilde{z}_0 + \Delta\bar{z} = f(x, y) + \Delta\bar{z} \quad (2.21)$$

The additional rounding error may be zero if the intermediate result of the operation does not need rounding. In practice, to obtain an exactly rounded result, it is necessary to perform the basic operations using at least 3 additional binary digits [26]. For non-basic operations, the error on the results could be larger and depends on how the operations are implemented.

Hence, the total error in the result of an operation is the sum of the propagation error and the additional rounding error:

$$\Delta z = \frac{\partial f}{\partial x}(x_0, y_0)\Delta\bar{x} + \frac{\partial f}{\partial y}(x_0, y_0)\Delta\bar{y} + \Delta\bar{z} \quad (2.22)$$

Using Widrow's model for numerical errors  $\Delta\bar{x}$ ,  $\Delta\bar{y}$ , and  $\Delta\bar{z}$ , the total error  $\Delta z$  is the sum of three uncorrelated white random variables and its statistical properties derive from the characteristics of each round-off error:

- Mean value:

$$E[\Delta z] = \frac{\partial f}{\partial x}(x_0, y_0) E[\Delta\bar{x}] + \frac{\partial f}{\partial y}(x_0, y_0) E[\Delta\bar{y}] + E[\Delta\bar{z}] = 0 \quad (2.23)$$

- Maximum absolute value:

$$\begin{aligned} \Delta z_{\max} &= \left| \frac{\partial f}{\partial x}(x_0, y_0) \right| \Delta\bar{x}_{\max} + \left| \frac{\partial f}{\partial y}(x_0, y_0) \right| \Delta\bar{y}_{\max} + \Delta\bar{z}_{\max} \\ &= \left| \frac{\partial f}{\partial x}(x_0, y_0) \right| \frac{q(x_0)}{2} + \left| \frac{\partial f}{\partial y}(x_0, y_0) \right| \frac{q(y_0)}{2} + \frac{q(z_0)}{2} \end{aligned} \quad (2.24)$$

- Variance:

$$\begin{aligned}\sigma_{\Delta z}^2 &= \left(\frac{\partial f}{\partial x}(x_0, y_0)\right)^2 \sigma_{\Delta x}^2 + \left(\frac{\partial f}{\partial y}(x_0, y_0)\right)^2 \sigma_{\Delta y}^2 + \sigma_{\Delta z}^2 \\ &= \left(\frac{\partial f}{\partial x}(x_0, y_0)\right)^2 \frac{q(x_0)^2}{12} + \left(\frac{\partial f}{\partial y}(x_0, y_0)\right)^2 \frac{q(y_0)^2}{12} + \frac{q(z_0)^2}{12}\end{aligned}\quad (2.25)$$

## 2.3 The Numerical Error Model

### 2.3.1 Differenced-Range Doppler Formulation

According to Moyer's DRD formulation, the unramped two-way ( $F_2$ ) or three-way ( $F_3$ ) Doppler observable is proportional to the mean time variation of the round-trip light-time (i.e. the mean range-rate divided by  $c$ ), during the count time interval centered in the observable's time-tag [51]:

$$F_{2,3}(TT) = M_2 f_T \frac{\rho(TT + T_c/2) - \rho(TT - T_c/2)}{T_c} \quad (2.26)$$

where:

- $TT$  is the observable's time-tag.
- $M_2$  is the spacecraft transponder turnaround ratio, which is the ratio of the transmitted frequency to the received frequency at the spacecraft.
- $f_T$  is the transmitted frequency of the signal at the transmitting antenna.
- $T_c$  is the count time interval on which the Doppler shift is computed.
- $\rho(t_3(\text{ST}))$  is the round-trip light-time, i.e. the time interval between the reception time  $t_3(\text{ST})$  and the corresponding transmission time  $t_1(\text{ST})$ , both referred to the ground station electronics and expressed in Station Time<sup>1</sup>:

$$\rho(t_3(\text{ST})) = t_3(\text{ST}) - t_1(\text{ST}) \quad (2.27)$$

$t_3$  is the reception time in Ephemeris Time<sup>2</sup> ( $T_{eph}$ ) [62]. It is computed from the reception time in ST,  $t_3(\text{ST})$ , through different time transformations, while the reflecting time at the spacecraft  $t_2$  and the transmission time  $t_1$  are computed from  $t_3$  solving for the down-link and the up-link light-time problems, respectively.

Neglecting second order terms, such as relativistic light-time delays, time scale transformations, electronic delays, and transmission media delays, the round-trip light-time can be written as:

$$\rho(t_3) \simeq \frac{r_{12}}{c} + \frac{r_{23}}{c} = \frac{\sqrt{(\mathbf{r}_2 - \mathbf{r}_1) \cdot (\mathbf{r}_2 - \mathbf{r}_1)}}{c} + \frac{\sqrt{(\mathbf{r}_3 - \mathbf{r}_2) \cdot (\mathbf{r}_3 - \mathbf{r}_2)}}{c} \quad (2.28)$$

where:

<sup>1</sup>Station Time is a realization of the proper time at the Earth ground station.

<sup>2</sup>Ephemeris Time is the coordinate time of the Solar System barycentric space-time frame of reference used in the adopted celestial ephemeris.

- $\mathbf{r}_1$  is the position vector of the transmitting ground station at  $t_1$ , with respect to the Solar System barycenter.
- $\mathbf{r}_2$  is the position vector of the spacecraft at the reflecting  $t_2$ , with respect to the Solar System barycenter.
- $\mathbf{r}_3$  is the position vector of the receiving ground station at  $t_3$ , with respect to the Solar System barycenter.
- $r_{12}$  is the Newtonian distance between the transmitting ground station at  $t_1$ , and the spacecraft at  $t_2$ .
- $r_{23}$  is the Newtonian distance between the spacecraft at  $t_2$ , and the receiving ground station at  $t_3$ .

All state vectors are expressed in the Solar System barycentric space-time frame of reference.

In Eq. 2.28 the position vectors  $\mathbf{r}_3$  and  $\mathbf{r}_1$  are computed from the planetary and lunar ephemeris and from the Earth-centered position of the ground station antenna:

$$\mathbf{r}_3 = \mathbf{r}_{\mathbf{A}3}^{\mathbf{C}}(t_3) = \mathbf{r}_{\mathbf{B}}^{\mathbf{C}}(t_3) - \frac{\mathbf{r}_{\mathbf{M}}^{\mathbf{E}}(t_3)}{1 + \mu_E/\mu_M} + \mathbf{r}_{\mathbf{A}3}^{\mathbf{E}}(t_3) \quad (2.29)$$

$$\mathbf{r}_1 = \mathbf{r}_{\mathbf{A}1}^{\mathbf{C}}(t_1) = \mathbf{r}_{\mathbf{B}}^{\mathbf{C}}(t_1) - \frac{\mathbf{r}_{\mathbf{M}}^{\mathbf{E}}(t_1)}{1 + \mu_E/\mu_M} + \mathbf{r}_{\mathbf{A}1}^{\mathbf{E}}(t_1) \quad (2.30)$$

where:

- $\mathbf{r}_j^i$  is the position vector of body  $j$  with respect to body  $i$ .
- $\mu_i$  is the gravitational parameter of the body  $i$ .

Superscripts and subscripts designating bodies are explained in Table 2.2.

Table 2.2: Abbreviations for all bodies participating in the light-time problem.

Abbreviation	Body
C	Solar System Barycenter
S	Sun
B	Earth-Moon system barycenter
M	Moon
E	Earth
A1	Transmitting ground station's antenna
A3	Receiving ground station's antenna
P	Probe
O	Center Of Integration of the spacecraft trajectory

$\mathbf{r}_2$  is computed from the spacecraft ephemeris, obtained by integrating the equations of motion with respect to the center of integration, and from the planetary and satellite ephemeris:

$$\mathbf{r}_2 = \mathbf{r}_{\mathbf{P}}^{\mathbf{C}}(t_2) = \mathbf{r}_{\mathbf{O}}^{\mathbf{C}}(t_2) + \mathbf{r}_{\mathbf{P}}^{\mathbf{O}}(t_2) \quad (2.31)$$

### 2.3.2 Sources of Numerical Errors and Order of Magnitude Considerations

Using the DRD formulation, the Doppler observable is computed as the difference of two round-trip light-times (Eq. 2.26). Qualitatively, this formulation has a high sensitivity to round-off errors because, as it is well known, the difference between two large and nearly equal values substantially increases the relative error, causing a loss of significance [26]. Hence, errors in the round-trip light-time have a large influence on the Doppler observables.

The main sources of numerical errors in the round-trip light-time are:

- Representation of times: rounding errors in the time variables.
- Representation of distances: rounding errors in the position vectors.
- Additional rounding errors: rounding errors in the result of each operation.

To evaluate the order of magnitude effect of the numerical errors a simple expression can be used. At first approximation, the numerical errors  $\Delta\rho$  in the round-trip light-time at the start and at the end of the count time can be considered independent. From Eq. 2.26, an order of magnitude estimation of the corresponding effect in the Doppler observable is:

$$\Delta F_{2,3} \simeq M_2 f_T \sqrt{2} \frac{\Delta\rho}{T_c} \quad (2.32)$$

The three error sources are described in the following sections.

#### 2.3.2.1 Representation of Times

The rounding errors in time epochs  $t_3$ ,  $t_2$ , and  $t_1$  propagate only indirectly into the round-trip light-time. An error  $\Delta t_k$  in time epoch  $t_k$  affects the computation of a position vector  $\mathbf{r}_j^i(t_k)$ , through the corresponding velocity vector  $\dot{\mathbf{r}}_j^i$ :

$$\Delta \mathbf{r}_j^i = \dot{\mathbf{r}}_j^i \Delta t_k \quad (2.33)$$

The most important orbit determination programs use different representation of the time variables  $t_k$ :

- The ODP represents a time variable as a single double-precision value of seconds past J2000 (January 1st 2000, 12:00) [51].
- AMFIN represents a time variable as a single double-precision value of days past January 1st 2000, 00:00 [17].
- MONTE represents a time variable as a pair of two double-precision values of seconds past J2000. Using two double-precision values is a fast software method to implement an extended precision, called double-double arithmetics. Using double-double precision However, double-double arithmetics does not follow the IEEE-754 standard.

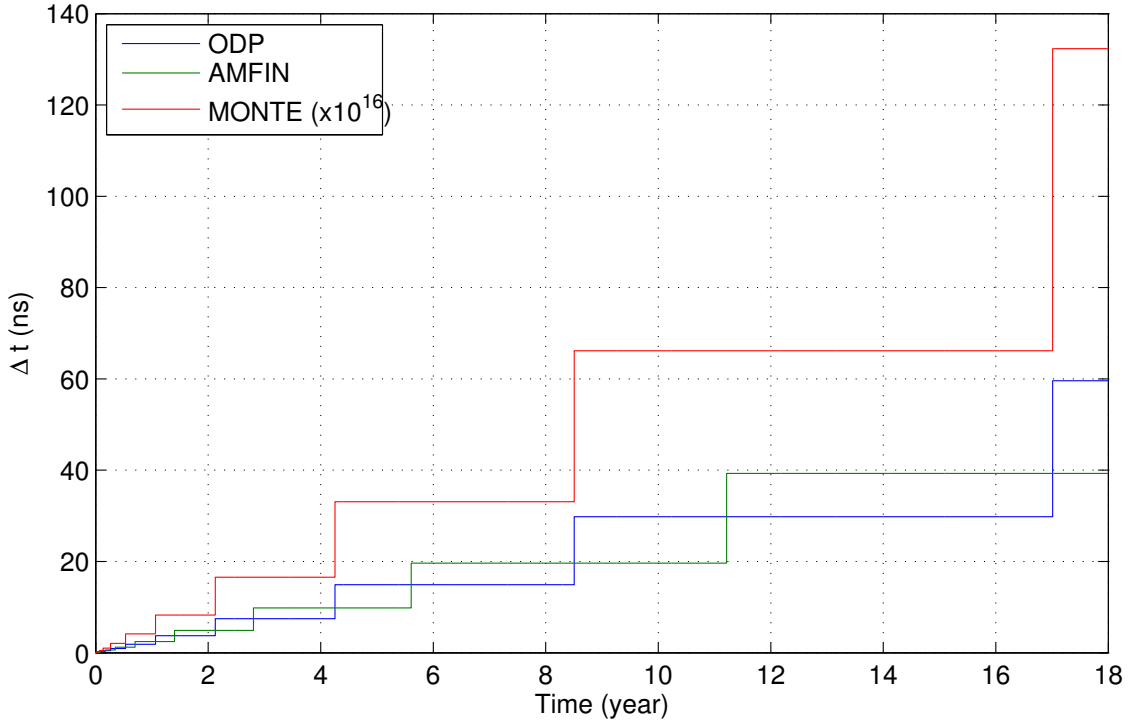


Figure 2.1: Maximum absolute round-off errors in time variable for the time representations adopted in the ODP, AMFIN and MONTE. When the time variable increases relative to the reference epoch, the maximum rounding error increases with a piecewise trend, because it doubles when the binary order of magnitude  $p(t)$  increases by one.

ODP and AMFIN use the same number of bits to represent time variables. Moreover the difference of 12 hours in the reference epochs is negligible, so with good approximation the only difference between ODP and AMFIN is the measurement unit adopted. Hence, as discussed in Chapter 2.2, the time round-off errors in these two orbit determination codes are not exactly the same, but they have the same average magnitude, on a large enough time interval.

MONTE uses the same reference epoch of the ODP, but the double-double arithmetics provide  $2 \times 52 = 104$  bits to represent the fractional part of the mantissa. The corresponding machine epsilon is  $2^{-105} \simeq 2.5 \times 10^{-32}$ , 256 times the machine epsilon of the quadruple precision but about 16 orders of magnitude smaller than the simple double precision.

Figure 2.1 shows the maximum absolute round-off error in time variables, for the ODP, AMFIN and MONTE. Between July 2008 and January 2017, the maximum round-off error for the ODP-like time representation is about 30 ns. The approximate effect on the two-way range and range-rate can be computed using Eq. 2.33 and Eq. 2.32, considering a range-rate of 30 km/s. For the ODP, the effect of the time error on the two-way range has an order of magnitude of 2 mm, and the approximate effect on the two-way range-rate is about  $4 \times 10^{-2}$  mm/s, for a count time of 60 s. This corresponds to a significant ASDEV of about  $1.4 \times 10^{-13}$  at 60 s integration time. As stated above, for AMFIN the effect of the numerical errors in time variables has the same order of magnitude than the ODP. However, for MONTE

the numerical errors in the time variables are about 16 orders of magnitude smaller, so the corresponding effects on the two-way range and range-rate measurements are completely negligible.

### 2.3.2.2 Representation of Distances

The rounding errors in each component of the position vectors propagate into the precision round-trip light-time directly, because the position vectors are used in the computation of the Newtonian distances  $r_{12}$  and  $r_{23}$ , but also indirectly, because the position vectors are used also in the computation of  $t_2$  and  $t_1$ . However, the indirect effects are much smaller, by a factor  $1/c$ , than the direct ones and can be neglected.

All the three most important orbit determination programs, ODP, AMFIN, and MONTE, express a single component of a position vector as a double-precision value, in km. At 1 AU the maximum round-off error in the two-way range is about 0.03 mm and at 10 AU it is about 0.24 mm. From Eq. 2.32, the approximate effect on the two-way range-rate is about  $7 \times 10^{-4}$  mm/s at 1 AU and  $6 \times 10^{-3}$  mm/s at 10 AU, for a count time of 60 s.

### 2.3.2.3 Additional Rounding Errors

The rounding errors in the result of each operation propagate into the round-trip light-time. In this analysis, the following steps in the computation of the round-trip light-time  $\rho$  were considered:

$$\mathbf{r}_B^E(t_i) = \mathbf{r}_M^E(t_i)/(1 + \mu_E/\mu_M) \quad i = 1, 3 \quad (2.34)$$

$$\mathbf{r}_E^C(t_i) = \mathbf{r}_B^C(t_i) - \mathbf{r}_B^E(t_i), \quad i = 1, 3 \quad (2.35)$$

$$\mathbf{r}_i = \mathbf{r}_{A_i}^C(t_i) = \mathbf{r}_E^C(t_i) + \mathbf{r}_{A_i}^E(t_i), \quad i = 1, 3 \quad (2.36)$$

$$\mathbf{r}_2 = \mathbf{r}_P^C(t_2) = \mathbf{r}_O^C(t_2) + \mathbf{r}_P^O(t_2) \quad (2.37)$$

$$\mathbf{r}_{ij} = \mathbf{r}_j - \mathbf{r}_i = [x_{ij} \quad y_{ij} \quad z_{ij}]^T, \quad (i, j) = (1, 2), (2, 3) \quad (2.38)$$

$$xx_{ij} = x_{ij}^2, \quad (i, j) = (1, 2), (2, 3) \quad (2.39)$$

$$yy_{ij} = y_{ij}^2, \quad (i, j) = (1, 2), (2, 3) \quad (2.40)$$

$$zz_{ij} = z_{ij}^2, \quad (i, j) = (1, 2), (2, 3) \quad (2.41)$$

$$xy_{ij} = xx_{ij} + yy_{ij}, \quad (i, j) = (1, 2), (2, 3) \quad (2.42)$$

$$rr_{ij} = xy_{ij} + zz_{ij}, \quad (i, j) = (1, 2), (2, 3) \quad (2.43)$$

$$r_{ij} = \sqrt{rr_{ij}}, \quad (i, j) = (1, 2), (2, 3) \quad (2.44)$$

$$t_{ij} = r_{ij}/c, \quad (i, j) = (1, 2), (2, 3) \quad (2.45)$$

$$\rho = t_{12} + t_{23} \quad (2.46)$$

The effect of the rounding errors in the computations is difficult to evaluate using a simple expression. However, as most of the computations involve position vectors, as a first approximation the effect can be considered of the same order of magnitude of the representation of distances.

The position vectors  $\mathbf{r}_j^i$  used in Eqs. 2.34, 2.35, 2.36, and 2.37 are computed using the astronomical ephemeris (given as an input to the program), the integration of

the equations of motion and the Earth-fixed location of the ground station antenna. For simplicity, the numerical errors introduced in these computational steps are neglected. This assumption was verified *a posteriori* through the validation of the numerical errors model.

### 2.3.3 Numerical Error Preliminary Model

As discussed in Chapter 2.2.3, a numerical error  $\Delta\bar{x}$  in a generic variable  $x$  propagates into the output variable  $z$  through the partial derivative  $\partial z/\partial x$ . Hence, the numerical noise in the round-trip light-time  $\rho$  at reception time  $t_3$  can be computed through the partial derivative of  $\rho$  with respect to each considered error source. Neglecting second order terms, the resulting expression for the total numerical error on  $\rho$  is:

$$\begin{aligned}
\Delta\rho(t_3) = & \frac{\dot{r}_{12} + \dot{r}_{23}}{c} \Delta\bar{t}_3 + \frac{\dot{r}_{12} - \dot{p}_{23}}{c} \Delta\bar{t}_2 - \frac{\dot{p}_{12}}{c} \Delta\bar{t}_1 \\
& + \frac{\hat{\mathbf{r}}_{12} - \hat{\mathbf{r}}_{23}}{c} \cdot [\Delta\bar{\mathbf{r}}_{\mathbf{P}}^{\mathbf{O}}(t_2) + \Delta\bar{\mathbf{r}}_{\mathbf{O}}^{\mathbf{C}}(t_2) + \Delta\bar{\mathbf{r}}_{\mathbf{P}}^{\mathbf{C}}(t_2)] \\
& + \frac{\hat{\mathbf{r}}_{23}}{c} \cdot \left[ \Delta\bar{\mathbf{r}}_{\mathbf{A}3}^{\mathbf{E}}(t_3) + \Delta\bar{\mathbf{r}}_{\mathbf{B}}^{\mathbf{C}}(t_3) - \frac{\Delta\bar{\mathbf{r}}_{\mathbf{M}}^{\mathbf{E}}(t_3)}{1 + \mu_E/\mu_M} \right. \\
& \left. + \Delta\bar{\mathbf{r}}_{\mathbf{A}3}^{\mathbf{C}}(t_3) + \Delta\bar{\mathbf{r}}_{\mathbf{E}}^{\mathbf{C}}(t_3) - \Delta\bar{\mathbf{r}}_{\mathbf{B}}^{\mathbf{E}}(t_3) + \Delta\bar{\mathbf{r}}_{23} \right] \\
& - \frac{\hat{\mathbf{r}}_{12}}{c} \cdot \left[ \Delta\bar{\mathbf{r}}_{\mathbf{A}3}^{\mathbf{E}}(t_1) + \Delta\bar{\mathbf{r}}_{\mathbf{B}}^{\mathbf{C}}(t_1) - \frac{\Delta\bar{\mathbf{r}}_{\mathbf{M}}^{\mathbf{E}}(t_1)}{1 + \mu_E/\mu_M} \right. \\
& \left. + \Delta\bar{\mathbf{r}}_{\mathbf{A}1}^{\mathbf{C}}(t_1) + \Delta\bar{\mathbf{r}}_{\mathbf{E}}^{\mathbf{C}}(t_1) - \Delta\bar{\mathbf{r}}_{\mathbf{B}}^{\mathbf{E}}(t_1) - \Delta\bar{\mathbf{r}}_{12} \right] \\
& + \frac{\Delta\bar{x}x_{12} + \Delta\bar{y}y_{12} + \Delta\bar{z}z_{12} + \Delta\bar{x}y_{12} + \Delta\bar{r}r_{12}}{2cr_{12}} \\
& + \frac{\Delta\bar{x}x_{23} + \Delta\bar{y}y_{23} + \Delta\bar{z}z_{23} + \Delta\bar{x}y_{23} + \Delta\bar{r}r_{23}}{2cr_{23}} \\
& + (\Delta\bar{r}_{12} + \Delta\bar{r}_{23})/c + \Delta\bar{t}_{12} + \Delta\bar{t}_{23} + \Delta\bar{\rho}
\end{aligned} \tag{2.47}$$

where  $\dot{p}_{ij}$  is defined as:

$$\dot{p}_{ij} \triangleq \dot{\mathbf{r}}_i \cdot \hat{\mathbf{r}}_{ij} \quad (i, j) = (1, 2), (2, 3) \tag{2.48}$$

The numerical error in two- or three-way Doppler observables with time-tag  $TT$  can be expressed as:

$$\Delta F_{2,3}(TT) = M_2 f_T \frac{\Delta\rho(TT + T_c/2) - \Delta\rho(TT - T_c/2)}{T_c} \tag{2.49}$$

Adopting the statistical model for each numerical error in Eq. 2.47, it is possible to evaluate the statistical properties of the total numerical error in the round-trip light-time  $\rho$  and Doppler observable  $F_{2,3}$ . It follows that  $\Delta\rho(t_3)$  is a stochastic process with the following characteristics:

- White.
- Non stationary, because the coefficients multiplying every single numerical error are a function of time. However their time variation is typically very slow and, for a typical duration of a tracking pass, the process can be considered stationary.
- Gaussian-like distribution/PDF: from the central limit theorem the sum of  $N$  independent and identically distributed random variables converges to a normally distributed random variable as  $N$  approaches infinity. Because the different numerical errors are a finite number and not identically distributed, the expected PDF is only qualitatively bell-shaped.
- Zero mean.
- Variance: the total variance is the sum of each term's variance. The variance of each numerical error can be computed using the formulation presented in Chapter 2.2.2.

The numerical error  $\Delta F_{2,3}$  has similar characteristics to  $\Delta\rho$  but it is not white, because two consecutive Doppler observables are a function of the round-trip light-time at their mid-time. In fact, the count times are consecutive, so the end of a count time is the start of the next count time:

$$TT_k + T_c/2 = TT_{k+1} - T_c/2 \quad (2.50)$$

Given Eq. 2.50, two consecutive Doppler observables can be written as:

$$\begin{aligned} F_{2,3}(TT_k) &= M_2 f_T \frac{\rho(TT_k + T_c/2) - \rho(TT_k - T_c/2)}{T_c} \\ &= M_2 f_T \frac{\rho(TT_{k+1} - T_c/2) - \rho(TT_k - T_c/2)}{T_c} \end{aligned} \quad (2.51)$$

$$\begin{aligned} F_{2,3}(TT_{k+1}) &= M_2 f_T \frac{\rho(TT_{k+1} + T_c/2) - \rho(TT_{k+1} - T_c/2)}{T_c} \\ &= M_2 f_T \frac{\rho(TT_{k+2} - T_c/2) - \rho(TT_{k+1} - T_c/2)}{T_c} \end{aligned} \quad (2.52)$$

Hence, the rounding error in  $\rho(TT_{k+1} - T_c/2)$  affects both  $F_{2,3}(TT_k)$  and  $F_{2,3}(TT_{k+1})$ . The autocorrelation function of  $\Delta F_{2,3}$  is:

$$\begin{aligned} R_{\Delta F}(\tau) &\triangleq \frac{\mathbb{E}[(\Delta F(t)) (\Delta F(t + \tau))]}{\sigma_{\Delta F(t)} \sigma_{\Delta F(t+\tau)}} \\ &\simeq \frac{2R_{\Delta\rho}(\tau) - R_{\Delta\rho}(\tau - T_c) - R_{\Delta\rho}(\tau + T_c)}{2[1 - R_{\Delta\rho}(T_c)]} \\ &= \begin{cases} 1, & \text{if } \tau = 0, \\ -1/2, & \text{if } |\tau| = T_c, \\ 0, & \text{if } |\tau| > T_c. \end{cases} \end{aligned} \quad (2.53)$$

The variance of  $\Delta F_{2,3}$  is proportional to the variance of  $\Delta\rho$ :

$$\begin{aligned}\sigma_{\Delta F_{2,3}}^2(TT) &= \left(\frac{M_2 f_T}{T_c}\right)^2 \left[ \sigma_{\Delta\rho}^2(TT + T_c/2) + \sigma_{\Delta\rho}^2(TT - T_c/2) \right] \\ &\simeq 2 \left(\frac{M_2 f_T}{T_c}\right)^2 \sigma_{\Delta\rho}^2(TT)\end{aligned}\tag{2.54}$$

recalling that  $\Delta\rho$  is a white noise.

Thus, the standard deviation of  $\Delta F_{2,3}$ , representing the numerical noise level in Doppler observables, depends on:

- Floating point word's length: the number of bits used for the fractional part of the mantissa defines the amplitude of all round-off errors. At present, almost all hardware and compilers implement the IEEE-754 standard.
- Time: the time at which the orbit determination problem is settled defines the order of magnitude of all time epochs, thus defining the quantization step and the amplitude of the round-off errors in each time variable.
- Geometry: the state vectors of all participants to the orbit determination problem define two critical factors:
  - The order of magnitude of the three components of each position vector, from which the range and the additional round-off errors derive.
  - The velocities of the participants that define the influence of time round-off errors in the observables.
- Count time:  $\Delta\rho$  does not depend upon  $T_c$ , hence  $\Delta F_{2,3}$  (and its standard deviation) varies with  $T_c^{-1}$ . As a reference a typical white-phase reference noise varies with  $T_c^{-1/2}$ .

However, the numerical noise does not depend upon the measurements band, because it is proportional to the uplink frequency  $f_T$ : increasing the frequency of the carrier increases the numerical noise in the Doppler, but the value remains constant in terms of fractional frequency.

### 2.3.4 Validation of the Widrow's Model

The most delicate assumption on which the preliminary numerical noise model is based is the statistical characterization of the round-off errors using Widrow's model. In order to verify this assumption and to study in detail the numerical errors, a Radiometric Observables Generator (ROG) computer code was developed. The program computes the two-way Doppler observables on the basis of Moyer's DRD formulation, with the following simplifications:

- The states of the celestial bodies, the ground stations and the spacecraft were computed using the SPICE kernels and toolkit [1].
- In the solution of the light-time problems and in the computation of the precision light-times only the Newtonian terms were considered.

All steps in the computations were performed using both the quadruple and double-precision floating point representation. Because the quadruple-precision machine epsilon is about 18 orders of magnitude smaller than the double-precision one, the numerical error in the quadruple-precision values can be neglected and the computed quantities can be considered as infinitely precise reference values. Hence, a very good estimation of the “real numerical errors” in each double-precision quantity can be obtained as the difference between the double-precision values and the quadruple-precision ones.

The ROG program was used to study the statistical properties of all the elementary round-off errors appearing in Eq. 2.47. As a result of the analysis, Widrow’s model was proven to be a good description of all round-off errors but  $\Delta\bar{t}_3$ , which cannot be considered a white random process, because its autocorrelation  $R_{\Delta\bar{t}_3}(t, T_c)$  is not a Dirac delta function. An example of the autocorrelation of  $\Delta\bar{t}_3$ , computed at two different passes, is shown in Figure 2.2.

The non applicability of the Widrow’s model to the rounding error  $\Delta t_3$  derives from how  $t_3$ , the receiving time in  $T_{eph}$ , is computed within the orbit determination program:  $t_3$  is computed from  $t_3(\text{ST})$ , the receiving time in ST, through a series of time transformations, of which only the transformation from International Atomic Time (TAI) [64, 65] to  $T_{eph}$  is relevant, from the point of the numerical errors. In fact, the difference between the timescales  $T_{eph}$  and TAI is given by a number of relativistic terms and it is mainly a function of the Earth’s orbital motion around the Sun. Hence,  $(T_{eph} - \text{TAI})$  is approximately a sinusoid with mean value 32.184 s, peak-to-peak amplitude of about 3.3 ms and period of nearly 1 year:

$$(T_{eph} - \text{TAI})_t \simeq 32.184 \text{ s} + (1.65 \text{ ms}) \cos\left(\frac{2\pi}{T_{\text{sid}}}t\right) \quad (2.55)$$

Using the DRD formulation, the computation of a two-way or three-way Doppler observable requires the computation of two round-trip light-times  $\rho$ , separated by the count time  $T_c$ . During this time interval the maximum variation of  $(T_{eph} - \text{TAI})$  is about 20 ns:

$$\begin{aligned} \Delta(T_{eph} - \text{TAI}) &\simeq (1.65 \text{ ms}) \left(\frac{2\pi T_c}{T_{\text{sid}}}\right) \cos\left(\frac{2\pi}{T_{\text{sid}}}t\right) \\ &\leq (1.65 \text{ ms}) \left(\frac{2\pi T_c}{T_{\text{sid}}}\right) \simeq 20 \text{ ns} \end{aligned} \quad (2.56)$$

This value is of the same order of magnitude than the least significant bit of  $t_3$ , so the Widrow’s model cannot longer be applied with sufficient accuracy [41] to  $\Delta\bar{t}_3$ . This error can still be described using an immediate extension of Widrow’s model, obtained neglecting the whiteness property.  $\Delta\bar{t}_3$  is modeled as a random process:

- Non-white.
- Wide-sense stationary (on a single pass).
- Uniformly distributed with zero mean.

It can be shown that the numerical error in  $t_3$  is the rounding error of the quantity  $(T_{eph} - \text{TAI})_{t_3}$  considering the quantization step of  $t_3$ :

$$\Delta\bar{t}_3 = \text{round}[(T_{eph} - \text{TAI})_{t_3}/q(t_3)] \cdot q(t_3) - (T_{eph} - \text{TAI})_{t_3} \quad (2.57)$$

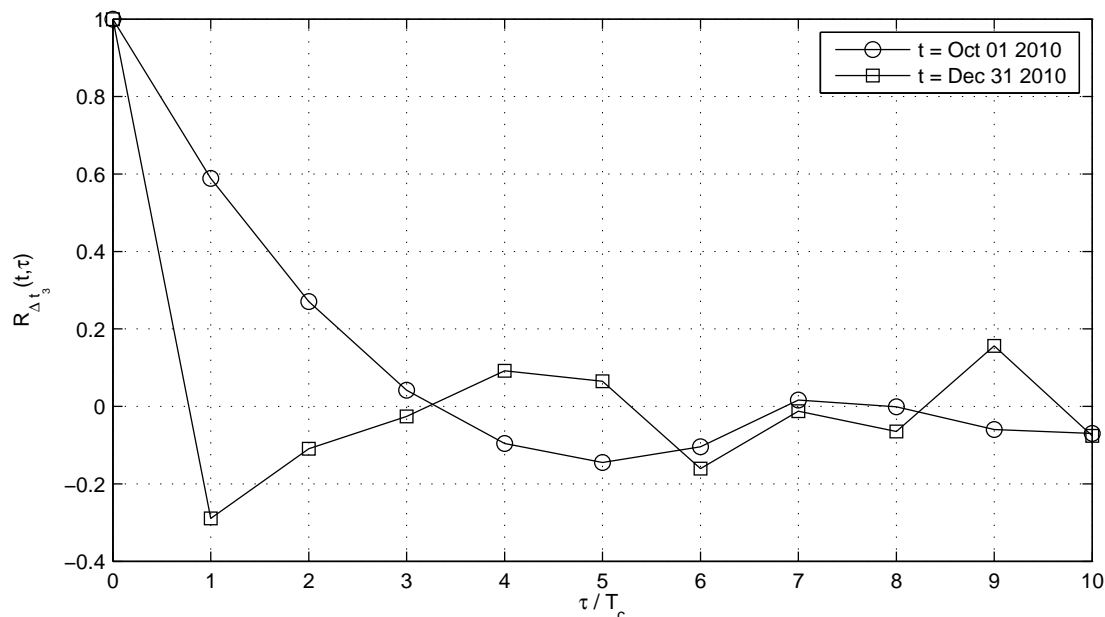


Figure 2.2: Autocorrelation of  $\Delta\bar{t}_3$ , computed on different tracking passes.

Hence,  $\Delta\bar{t}_3$  is function of  $(T_{eph} - \text{TAI})$  and of the quantization step of  $t_3$ ,  $q(t_3)$ , that is a piecewise constant function of time.

The autocorrelation  $R_{\Delta\bar{t}_3}(t, \tau)$  can be computed using the real error  $\Delta\bar{t}_3$  obtained from Eq. 2.57. Figure 2.3, representing  $R_{\Delta\bar{t}_3}(t, T_c)$  using  $T_c = 60$  s, shows a periodicity of 1/2 year that derives from  $(T_{eph} - \text{TAI})_t$  and, at about the middle of 2008, a discontinuity caused by the sudden doubling of  $q(t_3)$ .

### 2.3.5 Numerical Error Complete Model

Dropping the whiteness property of  $\Delta\bar{t}_3$ , the mathematical model of the numerical errors described in Chapter 2.3.3 must be slightly changed. In particular, the expressions of  $\Delta\rho$  and  $\Delta F_{2,3}$  remain the same, but their expected statistical characteristics change.  $\Delta\rho$  has almost the same properties described in Chapter 2.3.3, except that now it is a non-white random process, and its autocorrelation is a function of the autocorrelation of  $\Delta\bar{t}_3$ :

$$R_{\Delta\rho}(t, \tau) = \left( \frac{\dot{r}_{12} + \dot{r}_{23}}{c} \right)^2 \left( \frac{\sigma_{\Delta\bar{t}_3}}{\sigma_{\Delta\rho}} \right)^2 R_{\Delta\bar{t}_3}(t, \tau) \quad (2.58)$$

$\Delta F_{2,3}$  is a random process with the following characteristics:

- Non-white, with a non-stationary autocorrelation  $R_{\Delta F_{2,3}}(t, \tau)$ .
- Distribution: because of the autocorrelation of  $\Delta\bar{t}_3$ , the distribution may be very different from a bell-shaped curve. The expected probability density function of  $\Delta F_{2,3}$  was not computed in this study, due its complexity and its very low practical utility.
- Zero Mean.

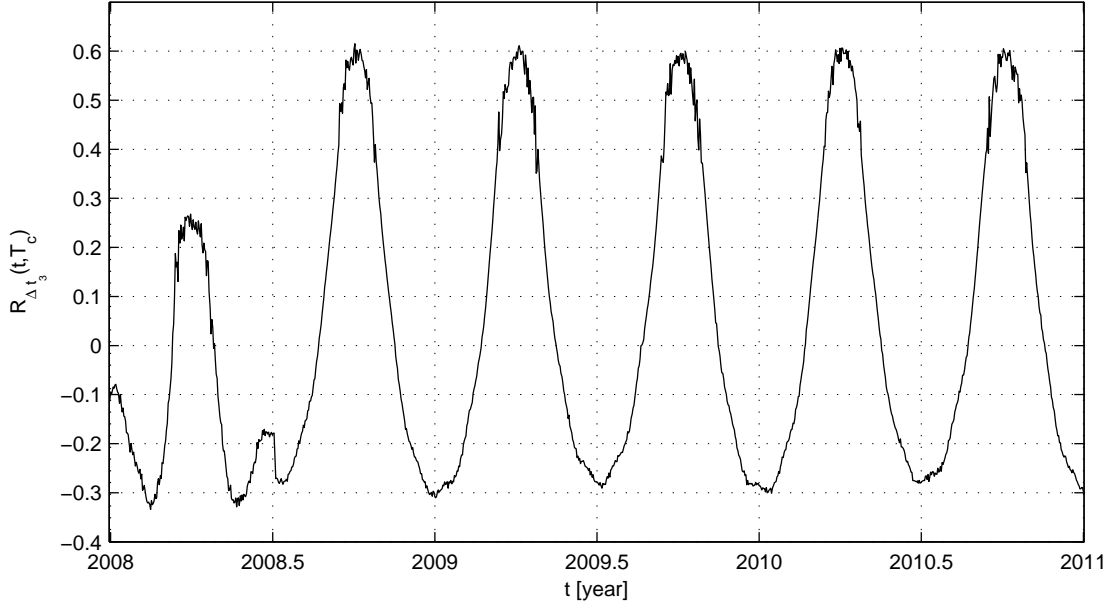


Figure 2.3: Time variation of the autocorrelation of  $\Delta\bar{t}_3$  after  $T_c = 60$  s.

- Standard Deviation: Eq. 2.54 must be changed to account for the autocorrelation of  $\Delta\bar{t}_3$  after  $T_c$  seconds:

$$\sigma_{\Delta F}^2(TT) \simeq \left(\frac{M_2 f_T}{T_c}\right)^2 \left[ 2\sigma_{\Delta\rho}^2(TT) - 2\left(\frac{\dot{r}_{12}(TT) + \dot{r}_{23}(TT)}{c}\right)^2 \cdot \sigma_{\Delta\bar{t}_3}^2(TT) \cdot R_{\Delta\bar{t}_3}(TT, T_c) \right] \quad (2.59)$$

## 2.4 Model Validation

### 2.4.1 Validation Procedure

The complete numerical error model described in Chapter 2.3.5 was validated by analyzing the real numerical noise in the Doppler observables computed by both the ODP and MONTE.

For the purpose of this study, two real-world scenarios were considered:

- Cassini mission, from January 2011 to the planned end of the mission on September 2017.
- Juno mission, from the launch at August 2011, to the planned end of the nominal mission on October 2017.

For each mission scenario the following steps were performed:

- Identification of the tracking passes: using an external program, all the tracking passes from the station DSS-25 of the NASA's Deep Space Network were identified. The program, developed in Fortran90, detect the time

intervals when the spacecraft elevation is greater than a minimum value using the spice kernel of the nominal trajectory of the mission as reference.

- Trajectory integration: for each tracking pass, ODP and MONTE were used to integrate the spacecraft trajectory over the time interval covered by the tracking pass. The initial state is retrieved from the spice kernel of the nominal trajectory. To simplify the simulation, a reduced dynamical model was used, which considers only the gravitational accelerations.
- Observables computation: for each tracking pass, ODP and MONTE were used to compute the corresponding two-way Doppler observables with respect to the ground station, using the X-band and a typical count time of 60 s.
- Numerical noise extraction: the numerical noise was extracted from the computed observables using the so-called “six-parameter fit” on each tracking pass.
- Numerical noise characterization: for each tracking pass the statistical properties of the numerical noise were computed and compared to the expected values generated by the complete model. In particular, the analysis focused on the standard deviation, which defines the numerical noise magnitude.

### 2.4.2 The Six-Parameter Fit

The numerical noise was extracted from the computed observables using the so-called “six-parameter fit”, a well known and simple method usually employed to estimate the noise content of Doppler observed observables [13, 19]. The fit is based upon a simplified formulation of the range-rate between the spacecraft and the Earth ground station [69]:

$$\dot{r}_P^{Ai}(t) = \dot{r}_P^E(t) + \omega_e r_s \cos \delta(t) \sin(\omega_e t + \alpha_0 + \lambda_s - \alpha(t)), \quad i = 1, 3 \quad (2.60)$$

where:

- $\omega_e$  is the Earth mean rotation rate.
- $r_s$  is the distance of the ground station from the Earth spin axis.
- $\alpha$  is the spacecraft right ascension.
- $\delta$  is the spacecraft declination.
- $\alpha_0$  is the right ascension of the prime meridian at the adopted epoch.
- $\lambda_s$  is the longitude of the ground station.

To take into account the Earth-spacecraft relative motion during the tracking pass,  $\dot{r}_P^E(t)$ ,  $\delta(t)$ , and  $\alpha(t)$  are expanded to a first-order Taylor time series centered at the start of the pass. Then, following [19], from Eq. 2.60 the range-rate can be expressed as a linear combination of the following six functions:

$$1, \quad t_p, \quad \sin \omega_e t_p, \quad \cos \omega_e t_p, \quad t_p \sin \omega_e t_p, \quad t_p \cos \omega_e t_p \quad (2.61)$$

From Eq. 2.26, the two-way and three-way Doppler observable is proportional to the mean range-rate during the count-time. Hence, during a single tracking pass, the six functions in Eq. 2.61 can be used to fit  $F_{2,3}$ , in a least-squares sense. The six estimated parameters, which define the fitting function, are related to the spacecraft geocentric state.

Due to the first-order approximation, the six-parameter fit can be successfully applied only when the spacecraft does not experience significant accelerations. Hence, during the numerical noise extraction, tracking passes corresponding to fly-bys were neglected.

In the absence of artificial additive random quantities, the numerical errors are the only non-negligible source of noise in the computed observables. Hence, the analysis is based upon the assumption that the six-parameter fit is capable of approximating (in a least-squares sense) the theoretical, infinitely precise, computed Doppler observables, leaving only the numerical errors as the fit's residuals.

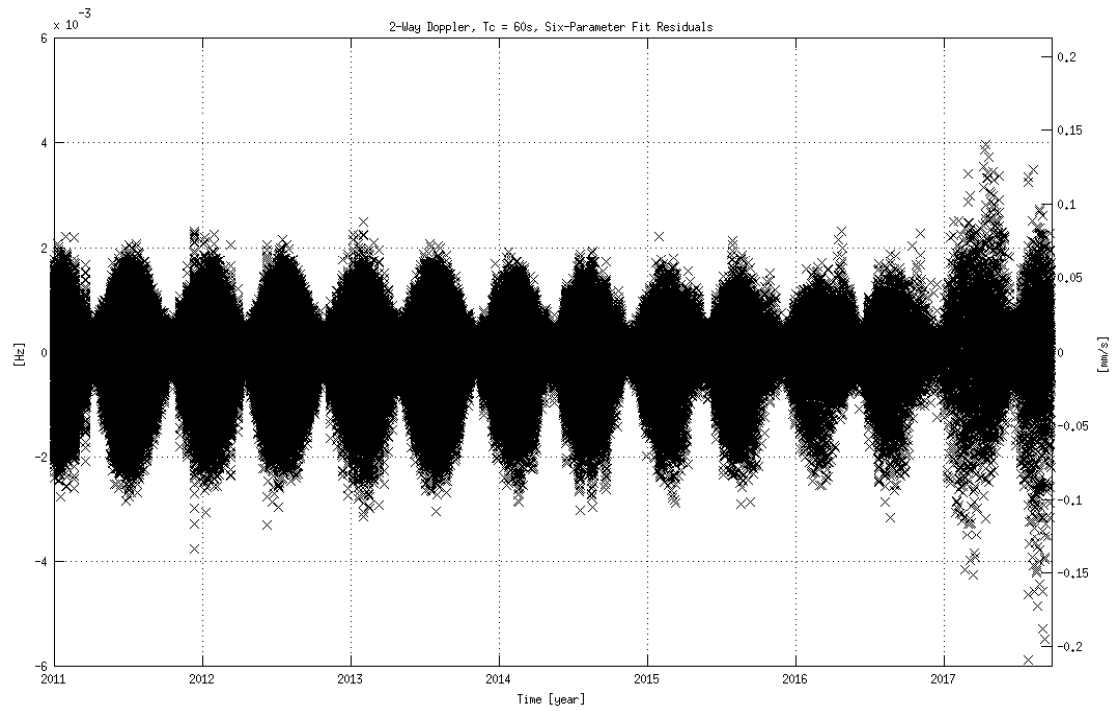
### 2.4.3 Validation Results

In this section the results of the different analyses are collected.

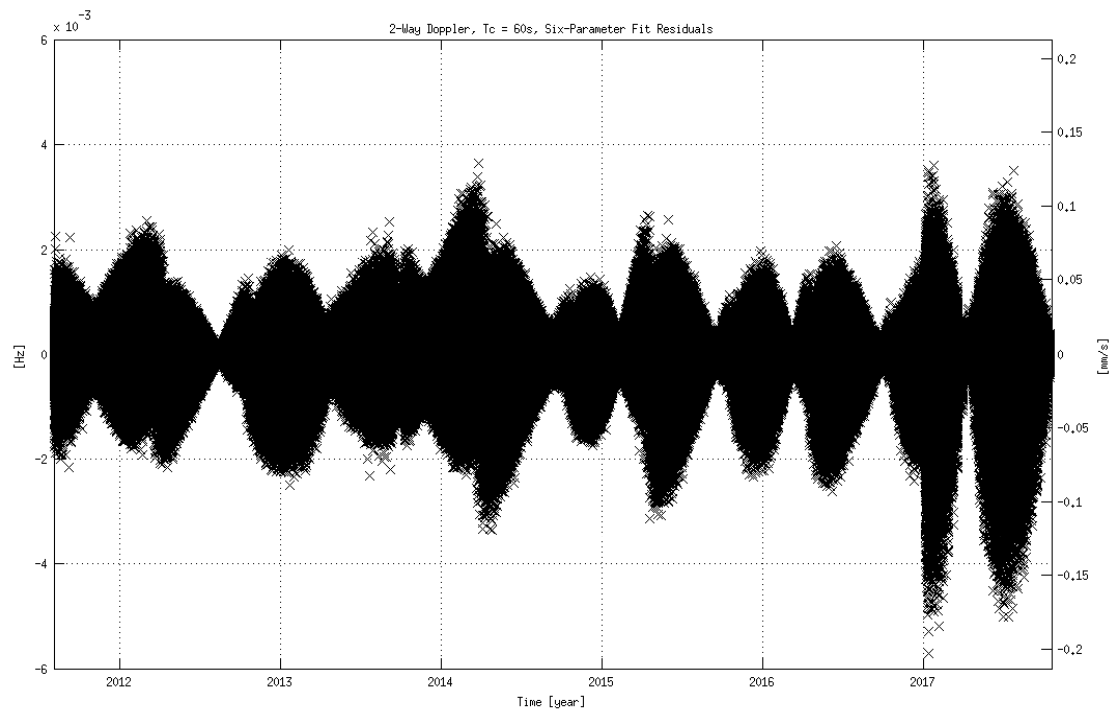
#### 2.4.3.1 ODP

Figure 2.4 reports the six-parameter fit residuals for the Cassini and Juno scenarios. For both the scenarios, the residuals have zero mean but they present a peculiar distribution, significantly different from a Gaussian distribution. This is due to the autocorrelation of  $\Delta t_3$  described in Chapter 2.3.4. For each tracking pass, the numerical noise extracted by the six-parameter fit from the two-way Doppler observables computed by the ODP was compared to the model described in Chapter 2.3.5, in terms of:

- Mean: for all analyzed tracking passes the ratio of the residuals' mean to their standard deviation remains bounded within  $3 \times 10^{-8}$ , so it can be considered zero for practical purposes, as predicted by the model.
- Standard deviation: Figure 2.5 and Figure 2.6 show that there is an optimal agreement between the model predictions and the real numerical error:
  - Juno scenario: the relative error is most of the time below 5% and always smaller than 15%. No significant trends are visible.
  - Cassini scenario: the relative error is most of the time below 10%, and always smaller than 40%. The standard deviations' ratio is noisier than in the Juno scenario, most likely due to the difficulties of the six-parameter fit to filter faster dynamics. The 1-sigma interval of the ratio, computed on a moving window of 100 days, is always around 1 and increases from about 1.05, at the beginning of the simulation, to about 1.15 at the end.

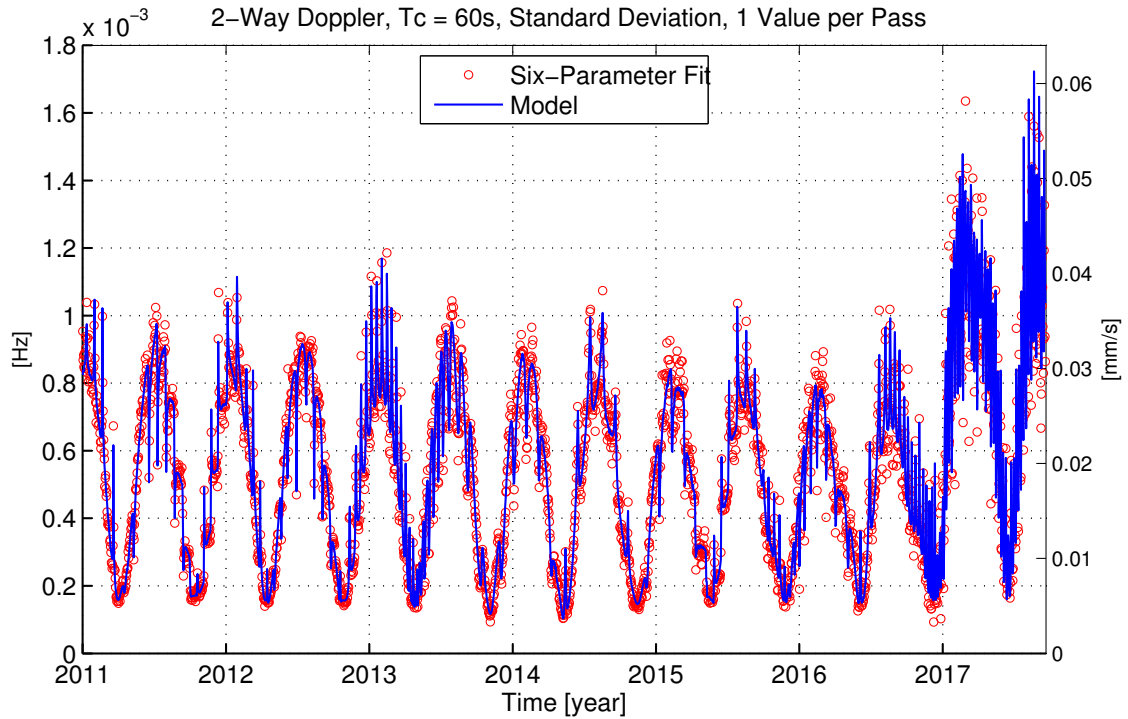


(a) Cassini mission from January 2011 to September 2017.

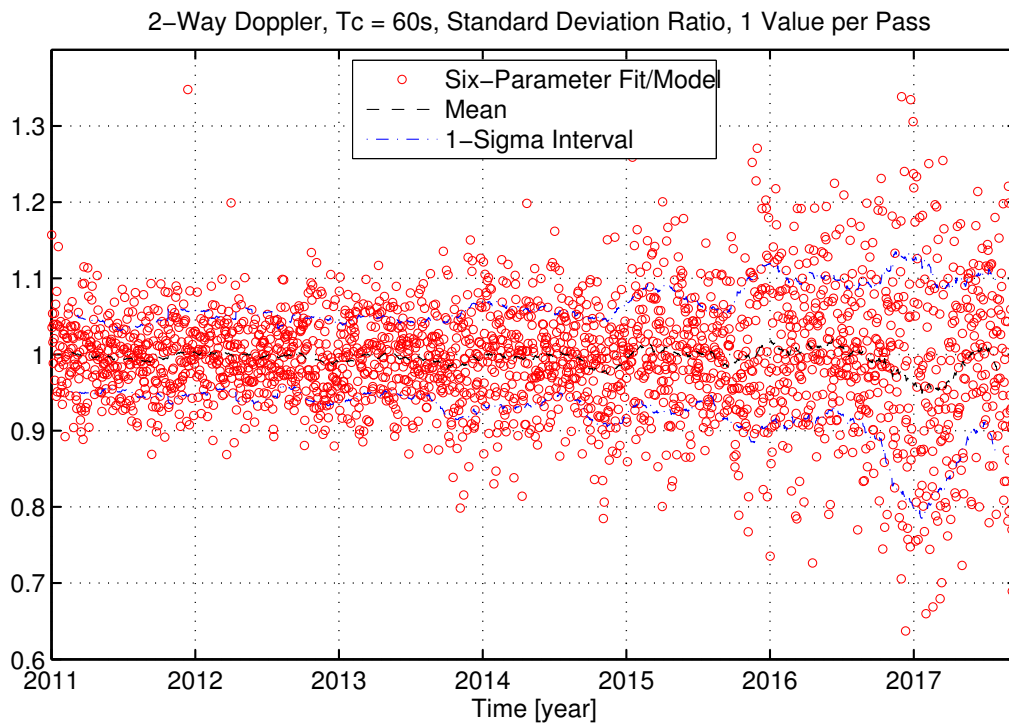


(b) Juno mission from August 2011 to October 2017.

Figure 2.4: Six-parameter fit applied to two-way Doppler observables computed by the ODP: fit's residuals in Hz and mm/s.



(a) Standard deviation in Hz and mm/s



(b) Standard deviation ratio.

Figure 2.5: Six-parameter fit applied to two-way Doppler observables computed by the ODP for the Cassini scenario: comparison between the standard deviation of the fit's residuals, computed on each tracking pass, and the predicted value of the numerical noise model.

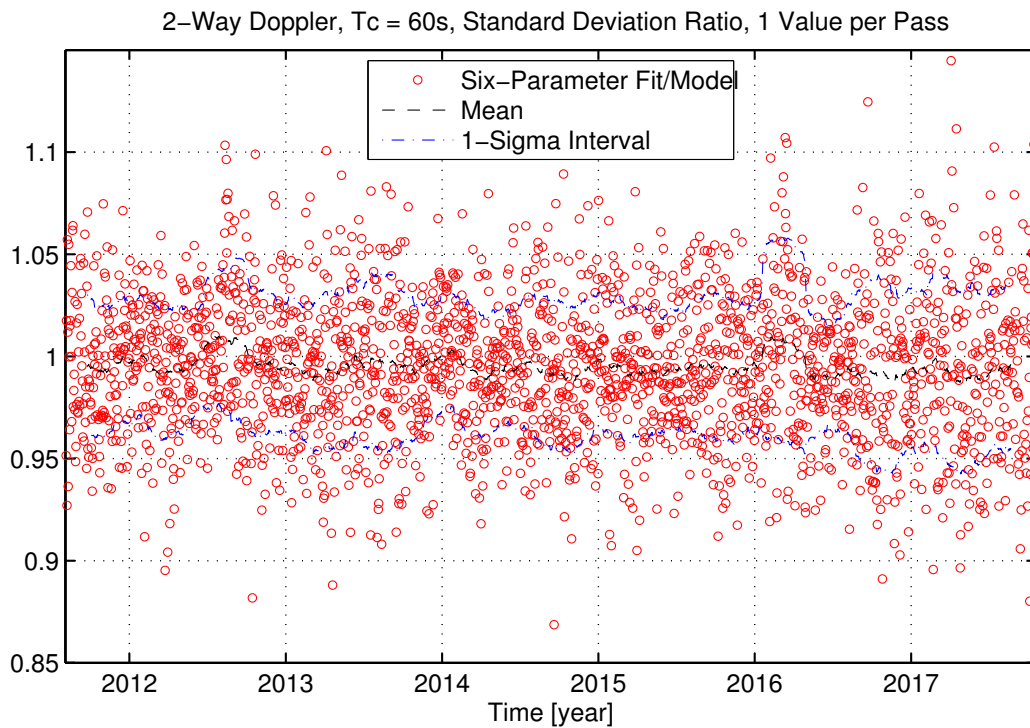
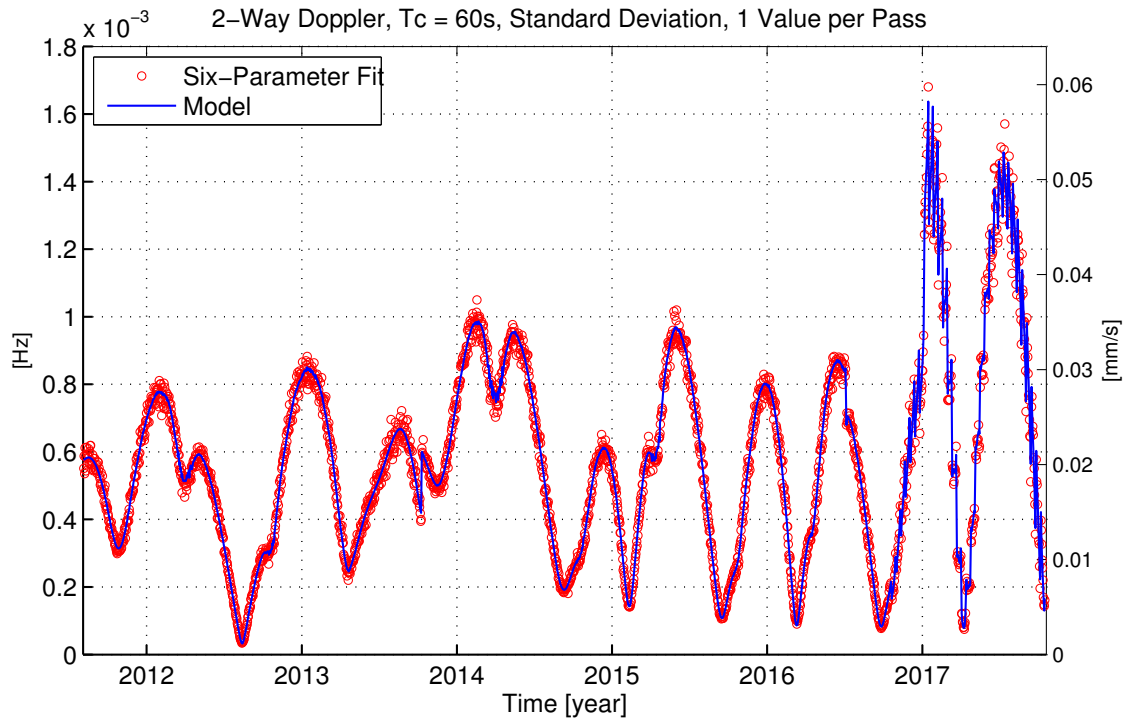


Figure 2.6: Six-parameter fit applied to two-way Doppler observables computed by the ODP for the Juno scenario: comparison between the standard deviation of the fit's residuals, computed on each tracking pass, and the predicted value of the numerical noise model.

### 2.4.3.2 MONTE

Figure 2.7 reports the six-parameter fit residuals for both the scenarios:

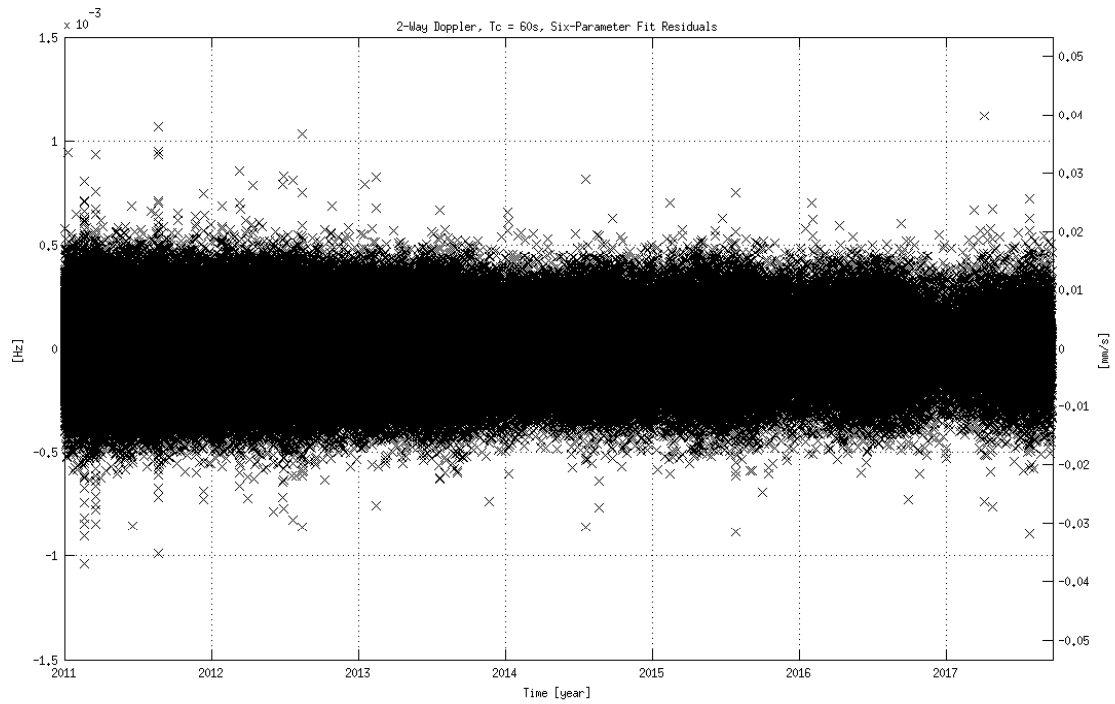
- Cassini scenario: the residuals appear good, with zero mean and without signatures.
- Juno scenario: the residuals have zero mean and most of the time they do not present signatures. However, on limited time intervals strange signatures appear, as shown by Figure 2.8. A more detailed analysis found that the signatures are caused by the so-called “bad points”.

The bad points are single measurements characterized by a numerical error much larger than the other measurements of the pass. On the affected tracking passes, the number of bad points per pass is small, always less than 5, and they are located near the beginning and the end of the tracking pass. The cause of the bad points is unknown, but it is most likely a software bug. However, as the source code of Monte is unavailable, a more detailed investigation cannot be performed. A bug report for the Monte developers team was open but, at present, no action was taken to investigate and fix this issue. For these reasons, for the validation of the numerical noise model, the bad points were removed from the residuals.

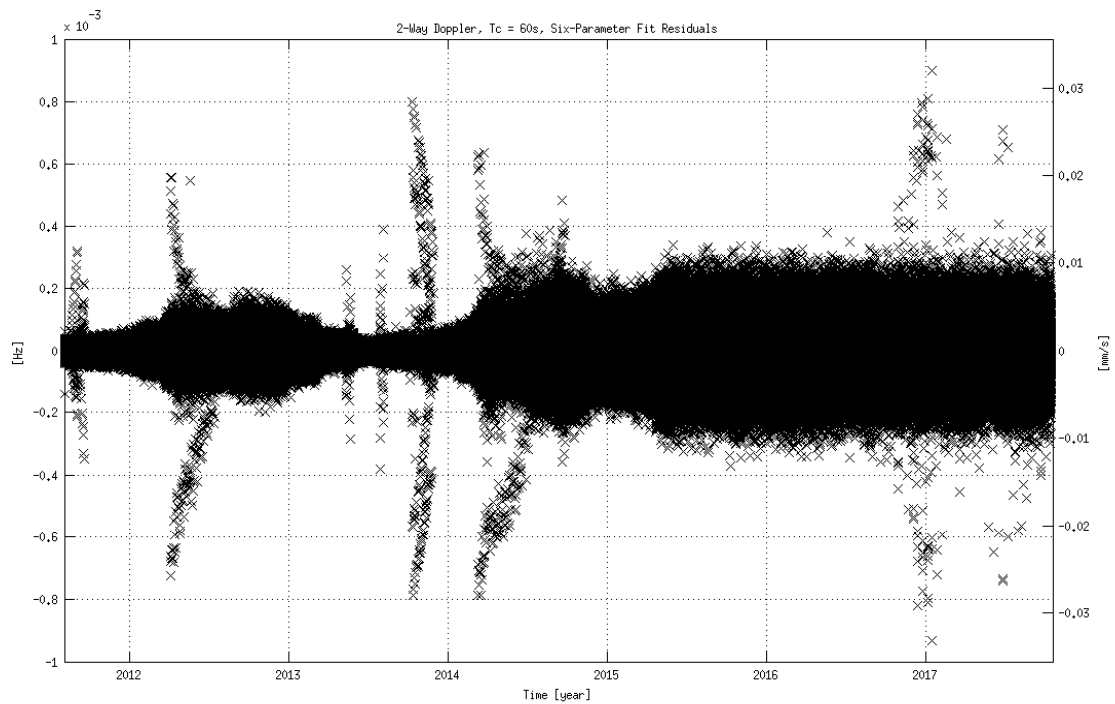
For each tracking pass, the numerical noise extracted by the six-parameter fit was compared to the model described in Chapter 2.3.5, in terms of:

- Mean: for all analyzed tracking passes the ratio of the residuals’ mean to their standard deviation remains bounded within  $5 \times 10^{-6}$ , so it can be considered zero for practical purposes, as predicted by the model.
- Standard deviation:
  - Cassini scenario: Figure 2.9 shows that there is a quite good agreement between the real numerical error and the model predictions. The relative error is most of the time below 20%, and always less than 50%. The standard deviations’ ratio becomes noisier with time, most likely due to the difficulties of the six-parameter fit to filter faster dynamics.
  - Juno scenario: Figure 2.10 shows that the numerical noise model follows quite well the time variation of the real numerical errors, being capable to replicate the sudden step variations of the noise, a typical behavior of the rounding errors. After the middle of 2015, when the numerical noise settles down to the highest values, the relative error is most of the time below 10%. Before this phase, when the total numerical noise is smaller, the relative error increases up to 50% . This increase is likely due to the approximations and simplifications introduced when developing the prediction model: the neglected rounding errors and the second order terms in the computation of the partial derivatives become non-negligible for small values of the errors.

To validate the numerical noise model, the analysis of the Juno scenario was performed removing the bad points from the six-parameter fit’s residuals. The numerical error of the bad points can be 2-3 orders of magnitude larger than the expected standard deviations.

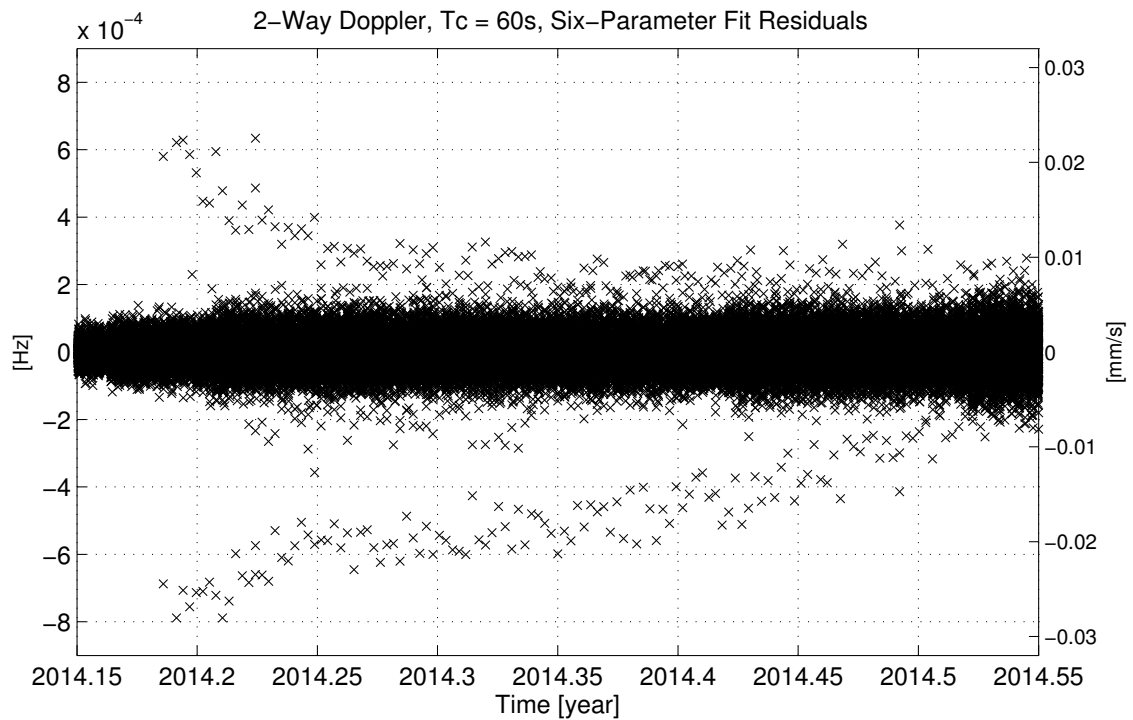


(a) Cassini mission from January 2011 to September 2017.

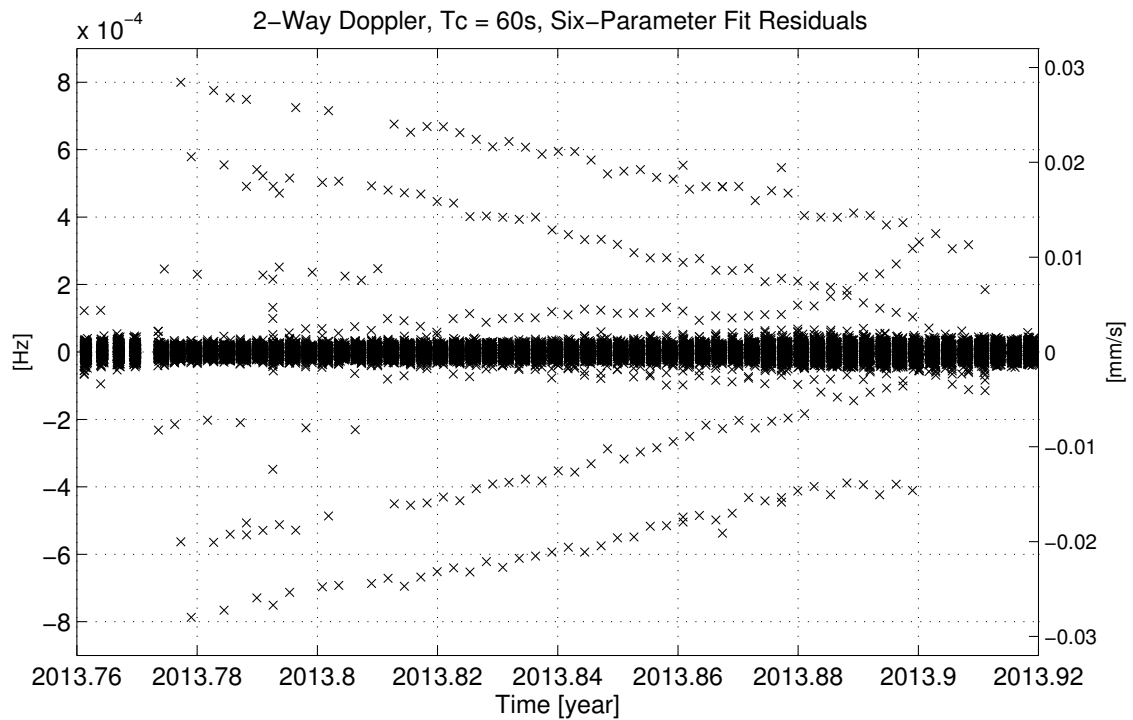


(b) Juno mission from August 2011 to October 2017.

Figure 2.7: Six-parameter fit applied to two-way Doppler observables computed by MONTE: fit's residuals in Hz and mm/s.

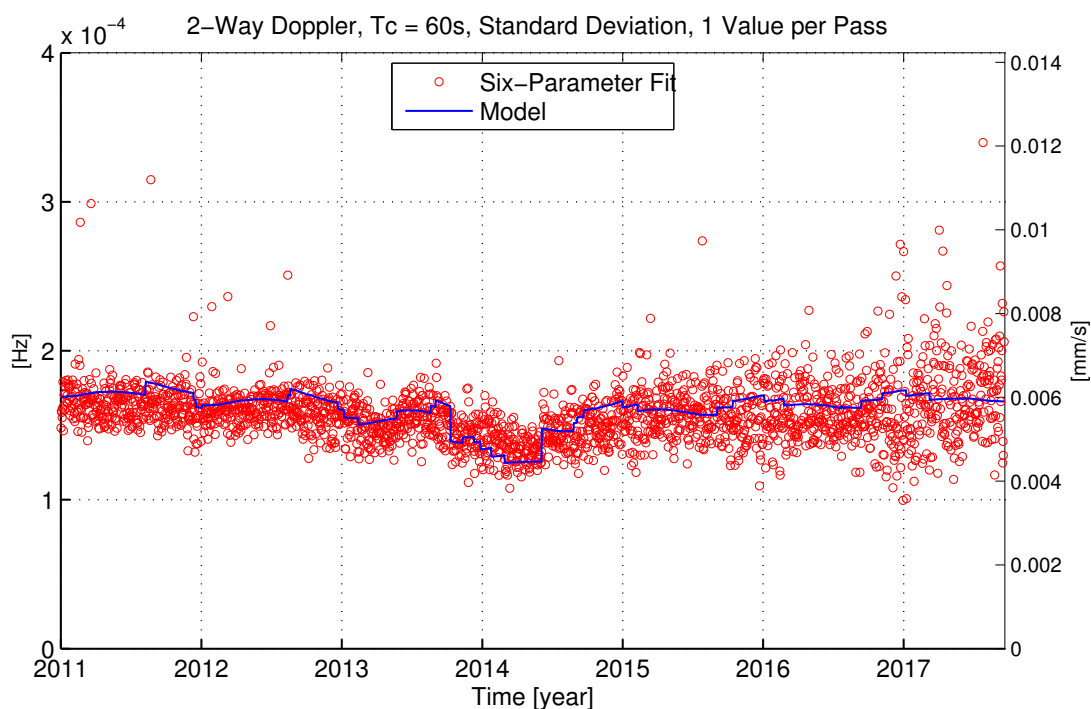


(a) Cassini mission from January 2011 to September 2017.

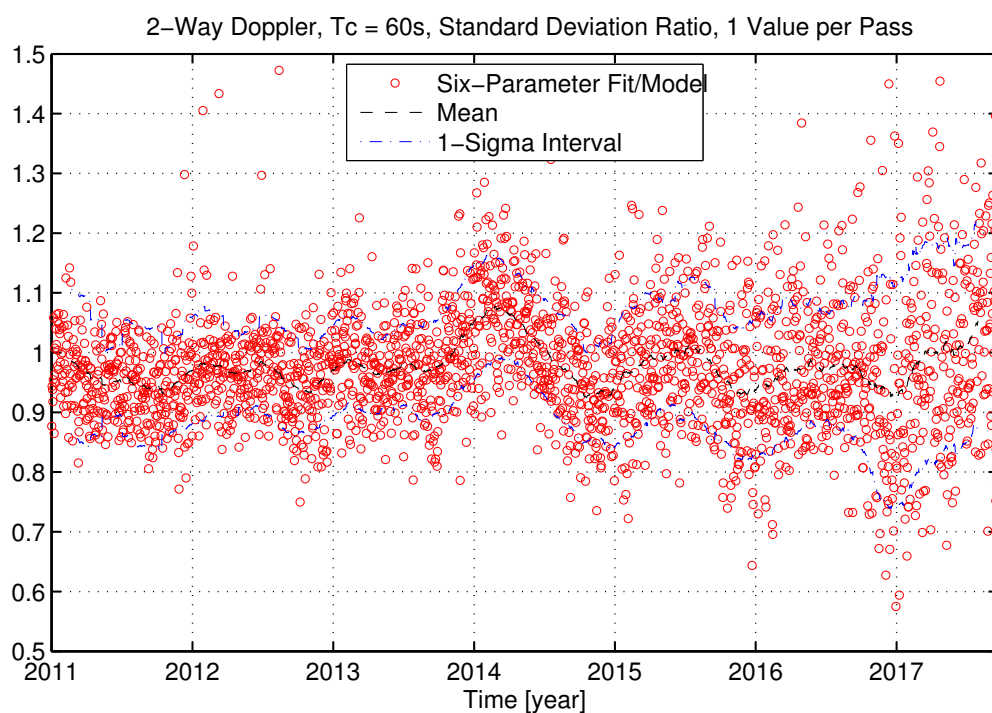


(b) Juno mission from August 2011 to October 2017.

Figure 2.8: Six-parameter fit applied to two-way Doppler observables computed by MONTE for the Juno scenario: fit's residuals in Hz and mm/s. Details at different levels of zoom to highlight the presence of the “bad points”.



(a) Standard deviation in Hz and mm/s



(b) Standard deviation ratio (zoom).

Figure 2.9: Six-parameter fit applied to two-way Doppler observables computed by the MONTE for the Cassini scenario: comparison between the standard deviation of the fit's residuals, computed on each tracking pass, and the predicted value of the numerical noise model.

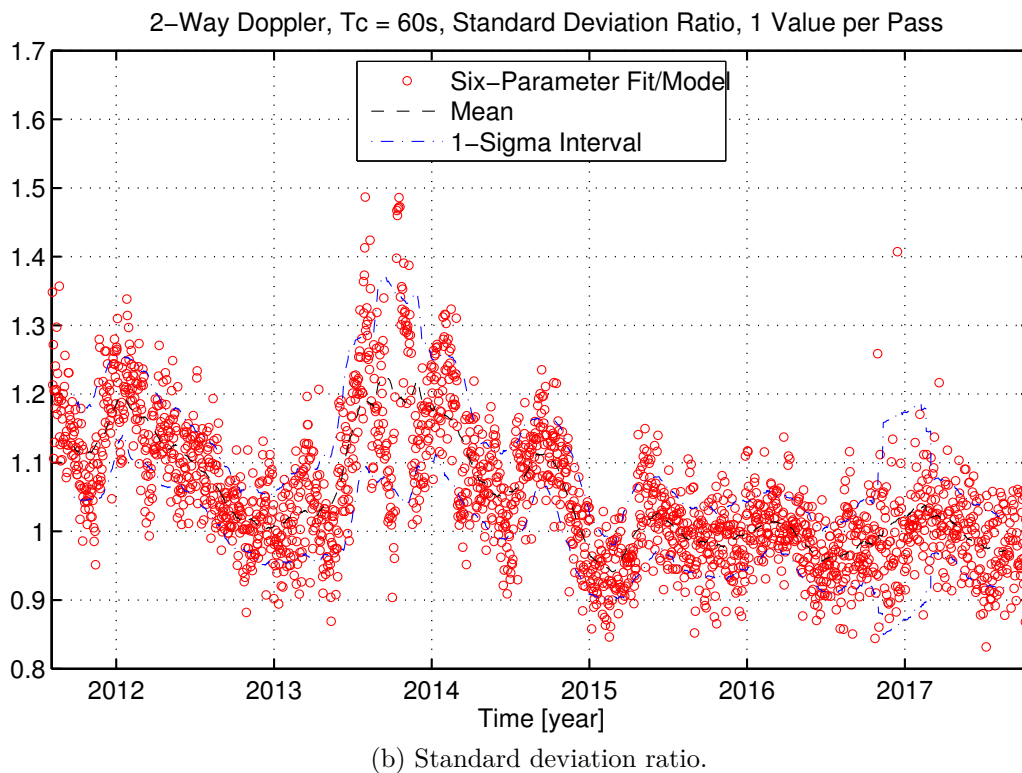
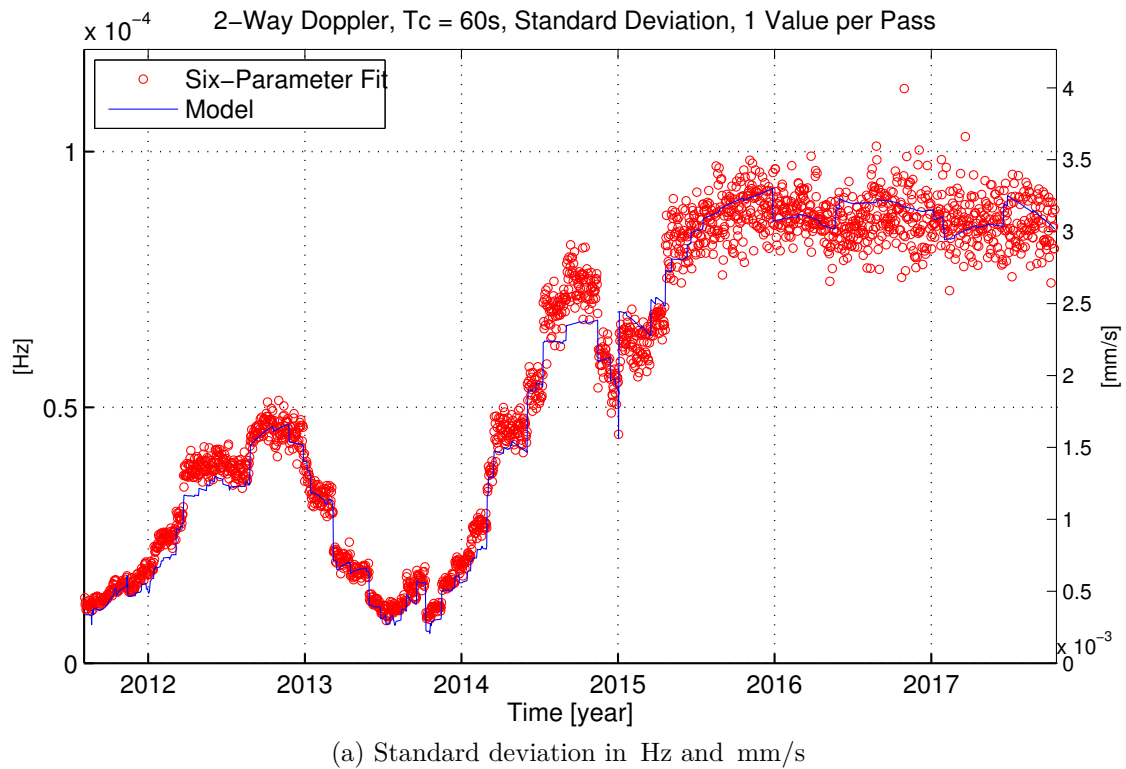


Figure 2.10: Six-parameter fit applied to two-way Doppler observables computed by the MONTE for the Juno scenario, without the “bad points”: comparison between the standard deviation of the fit’s residuals, computed on each tracking pass, and the predicted value of the numerical noise model.

### 2.4.4 Validation Conclusions

Summarizing, the developed model provides quantitative predictions of the different properties of the numerical noise in the Doppler observables. These predictions were compared to the actual characteristics of the numerical noise of the ODP and MONTE:

- ODP numerical noise: the analysis highlighted an optimal global agreement between the model and the experimental data, with typical relative errors below 10% and always smaller than 40%.
- MONTE numerical noise: the analysis highlighted the presence of the so-called “bad points” a limited number of measurements characterized by much higher numerical errors. Their origin is unknown, but most likely they are caused by a software bug. The numerical error of the bad points can be up to 3 orders of magnitude larger than the noise of the remaining measurements. Removing the bad points, the numerical noise model proved to follow quite well the experimental data, with typical relative errors below 15% and always smaller than 50%.

Hence, the numerical error model can be considered as fully validated at a level of accuracy adequate to *a priori* characterize the expected numerical noise of a real orbit determination scenario. Moreover, as said in Chapter 2.3, while developing the model, many assumptions were made and different sources of numerical errors were neglected. These simplifications may degrade the model accuracy when the total numerical noise is small. Given the obtained results, these simplifications were proved not to affect significantly the accuracy of the model predictions.

## 2.5 Numerical Noise Analysis

Using the numerical noise model described in Chapter 2.3 and validated in Chapter 2.4, a qualitative and quantitative characterization of the numerical noise was performed, for both the ODP and MONTE orbit determination programs.

Two real-world case studies were considered:

**The Cassini mission:** Cassini is a joint NASA/ESA/ASI mission to study the Saturn’s planetary system, formed by the planet Saturn, its moons and its ring system. Cassini was launched in 1997 and reached Saturn in 2004. After 4 years of successful science investigations, the mission was extended a first time in 2008 and a second time in 2010. In November 2016 Cassini is planned to be inserted into low altitude orbits, characterized by a periapsis of about 1.1 Saturn radii, just inside the D ring. After about 42 orbits the spacecraft will impact the Saturn atmosphere in September, 2017 [59]. Due to the very low periapsis altitude, during this end of mission phase the expected scientific return of Gravity Radio Science Experiments is very relevant.

**The Juno mission:** Juno is a NASA New Frontiers interplanetary mission to study the origin, interior structure, and evolution of the planet Jupiter [43].

Juno was launched on August 15, 2011, and, after two Deep Space Maneuvers (DSM) and an Earth gravity assist, will reach Jupiter in July 2016. In August 2016, through the Jupiter Orbit Insertion (JOI) maneuver, it will be placed in a highly eccentric polar orbit around Jupiter. The nominal mission will end in September 2017, with an impact on Jupiter after a de-orbiting maneuver. The mission will consist of 31 science orbits, 25 of which will be dedicated to gravity radio science experiments. In fact, one of the main scientific objectives of the Juno mission is to map the Jupiter gravity field with unprecedented accuracy. During gravity orbits, a dual-frequency (at X- and Ka-band) two-way Doppler link will be established between the Goldstone Deep Space Network (DSN) complex<sup>3</sup> and the spacecraft Juno, with a nominal observing interval of about 6 hours around perijove. This configuration, along with state-of-the-art troposphere calibration techniques, is expected to reach a two-way accuracy of  $3.0 \times 10^{-3}$  mm/s at 1000 s integration time or better, during the entire mission [23].

### 2.5.1 ODP Numerical Noise

Figures 2.11 to 2.14 show the expected ODP numerical noise during the Cassini and Juno missions, for two-way Doppler observables at X-band and 60 s of count time. The plots represent the total numerical noise, plus the noise level due to each of the three error sources: representation of time (Time), position vectors (Range), and additional round-off errors (Additional). Note that the total noise curve is the square root of the sum of the three squared components.

The following considerations about ODP numerical noise can be made:

- The Range and Additional components have a similar trend and increase with spacecraft's distance from the Earth, reaching almost constant values with the arrival at Saturn's and Jupiter's orbit distance. For Juno the Range and Additional components have less influence on the total noise with respect to Cassini, because of the shorter distance from the Solar System Barycenter (about 5.4 AU for Jupiter, about 10 AU for Saturn).
- The time variation of the Time component is a function of the relative velocity between the ground station and the spacecraft, while the noise amplitude, and the mean level, are a function also of the time elapsed since J2000. Hence, the amplitude of the Time component has the minimum value at J2000, and increases from J2000 becoming dominant. The instantaneous amplitude variation due to the time quantization step changes is clearly visible, for example at the beginning of 2002 and 2004, at the middle of 2008 and at the beginning of 2017. During the cruise phase of the missions the trend of the Time component of the numerical noise clearly shows an approximately half-year periodicity due to Earth's orbital motion. After the Saturn and Jupiter orbit insertion, at the middle of 2004 for Cassini and at the middle of 2016 for Juno, the trend of the Time component is the superposition of

---

<sup>3</sup>At present, only the Deep Space Station (DSS) 25 of the Goldstone site is capable of transmitting at Ka-band.

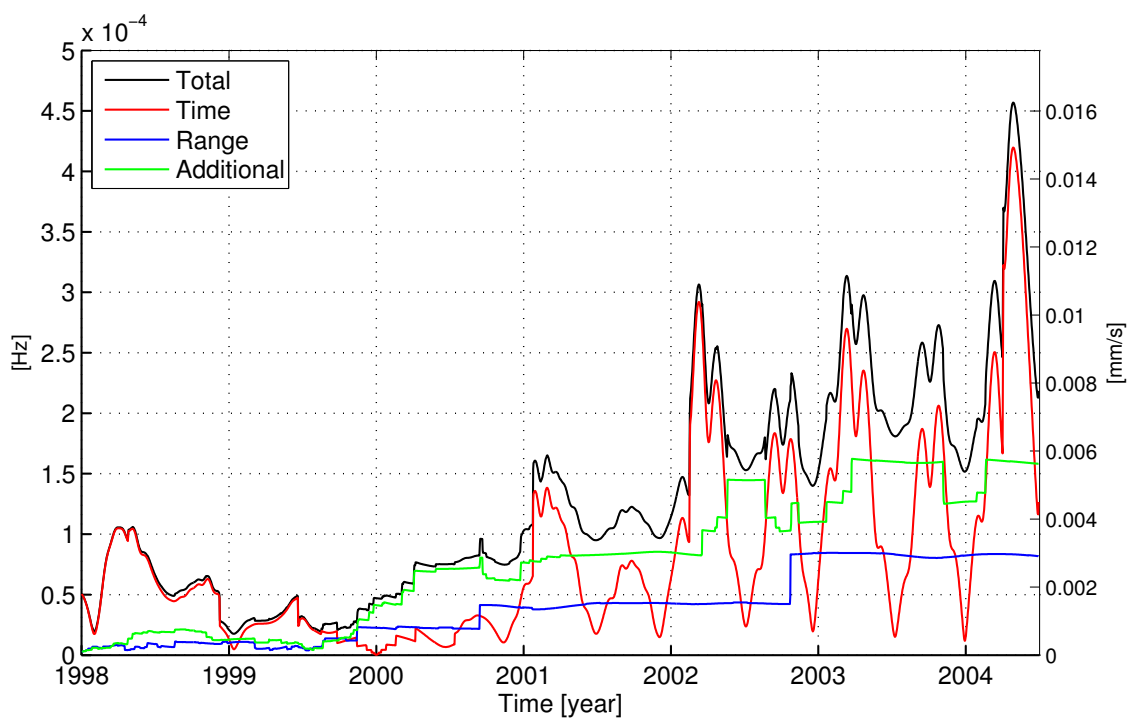


Figure 2.11: Numerical noise in Cassini's two-way Doppler observables ( $T_c=60$  s) during the cruise phase, from the beginning of 1998 to the middle of 2004.

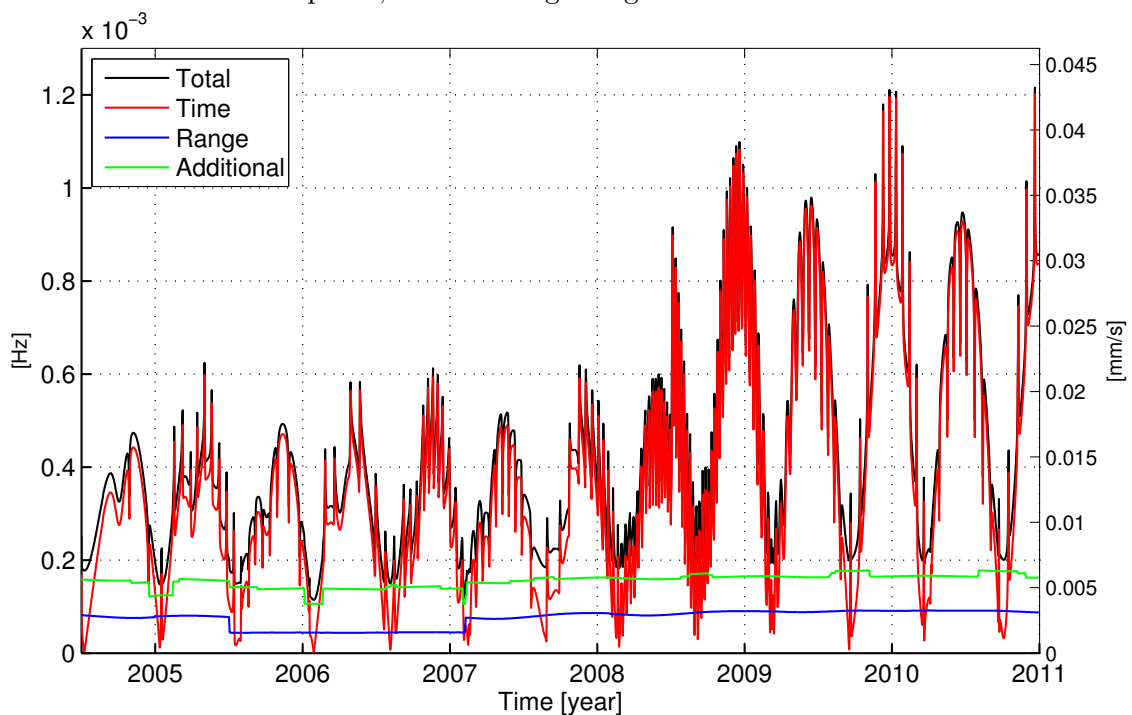


Figure 2.12: Numerical noise in Cassini's two-way Doppler observables ( $T_c=60$  s) during the Nominal Mission (from the middle of 2004 to the middle of 2008) and the Equinox Mission (from the middle of 2008 to the end of 2010).

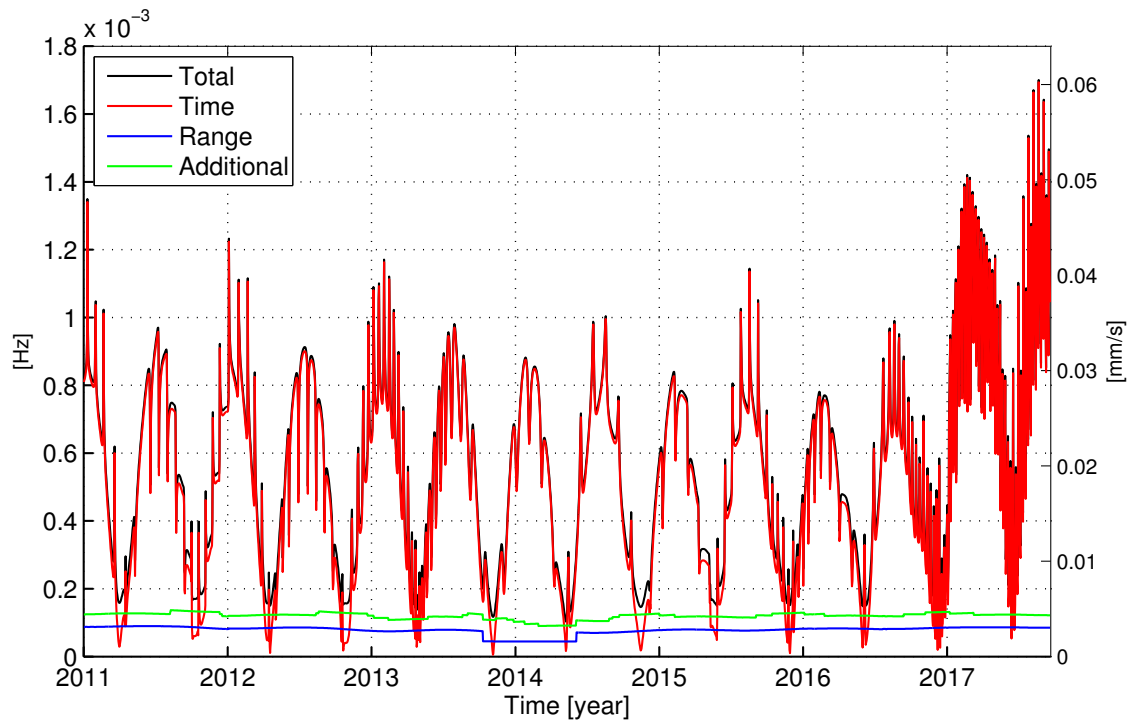


Figure 2.13: Numerical noise in Cassini's two-way Doppler observables (X-band,  $T_c=60$  s) during the Solstice Mission, from the end of 2010 to the end of 2017.

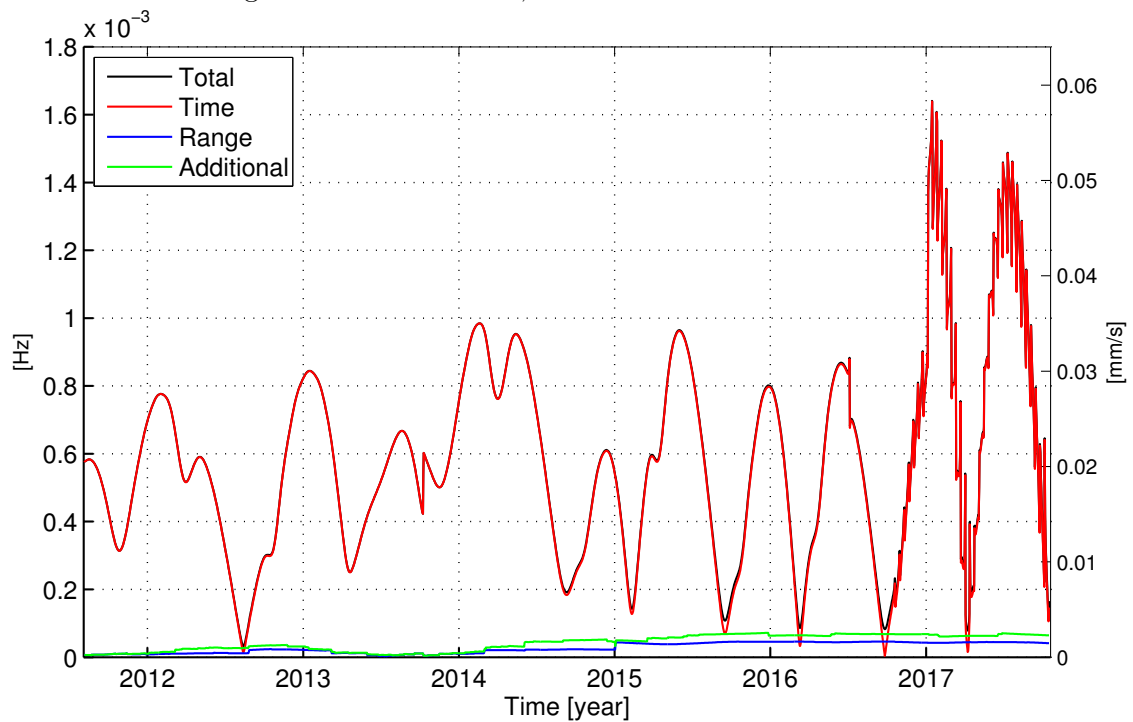


Figure 2.14: Numerical noise in Juno's two-way Doppler observables (X-band,  $T_c=60$  s) during the cruise phase, from the end of 2011 to the end of 2016.

the low-frequency Earth-planet relative motion and the higher frequency spacecraft orbital motion around the planet.

- Considering the Cassini mission, during the cruise phase until the beginning of 2004, the three components of the numerical noise had, on average, about the same order of magnitude. Since about the beginning of 2004, the Time component has increased and became dominant over the other sources, in almost the entire residual mission.
- Considering the Juno mission, the numerical noise is dominated by the Time component during almost the entire mission duration. Comparing the Juno mission to the Cassini Solstice mission, the time variable assumes approximately the same values.
- The maximum numerical noise during the Cassini mission is about  $60 \mu\text{m/s}$ , reached near the end of the mission. The best accuracy in Cassini two-way Doppler tracking, with proper state-of-the-art calibrations and under favorable conditions, is about  $9 \times 10^{-4} \text{ mm/s}$  with a count time of 1000 s, and it was achieved during the Gravitational Wave Experiment (GWE), performed during the 2001-2002 solar opposition [6]. As another reference, during the Solar Conjunction Experiment (SCE) at the middle of 2002, a two-way fractional frequency stability of about  $4.3 \times 10^{-3} \text{ mm/s}$  was achieved, with a count time of 300 s [14]. Assuming white phase noise, the corresponding noise level at 60 s integration time is about  $3.7 \times 10^{-3} \text{ mm/s}$  for the GWE and about  $9.5 \times 10^{-3} \text{ mm/s}$  for the SCE. The expected numerical noise, with the same count time, has been of the same order of magnitude since about the beginning of 2001, and becomes up to 15 times larger at the beginning of 2017, near the end of mission.<sup>4</sup> However, the best accuracy was achieved under the most favorable conditions: the spacecraft was in cruise at solar opposition, the dispersive noise was removed using the state-of-the-art full multi-frequency link technique [12, 42], and the troposphere noise was calibrated using Advanced Water-Vapor Radiometers (AWVR) measurements [27]. In 2003 the KaT transponder suffered an unrecoverable failure, so the multi-frequency link was not available during the Saturn tour. At present, the best accuracy achievable by two-way Doppler measurements of Cassini is about  $15 \mu\text{m/s}$ , with 60 s of integration time. The ODP numerical noise is still larger than this value, thus remaining the dominant noise source.
- The expected two-way Doppler measurement accuracy of Juno is  $1.2 \times 10^{-2} \text{ mm/s}$  at 60 s integration time [23]: for a large portion of the mission the total numerical noise is significantly larger than this value. Hence, in order to fully exploit the capabilities of the high performance Juno Doppler link, it is

---

<sup>4</sup>Note that this comparison does not reflect the numerical noise level experienced during the SCE and GWE experiments, because they were performed using higher count times. White phase noise scales with  $T_c^{-\frac{1}{2}}$ , while the numerical noise scales with  $T_c^{-1}$ . For example, during GWE an accuracy of about  $9 \times 10^{-4} \text{ mm/s}$  was achieved, with a count time of 1000 s. At this count time the corresponding expected numerical noise is  $4 \times 10^{-3} \cdot 60/1000 = 2.4 \times 10^{-4} \text{ mm/s}$ .

necessary to reduce the numerical noise impact in the Doppler observables computed by the orbit determination program.

Summarizing, for the ODP the numerical noise is a very important source of error in the orbit determination of current interplanetary missions.

## 2.5.2 MONTE Numerical Noise

Figures 2.15 to 2.18 show the expected MONTE numerical noise during the Cassini and Juno missions, for two-way Doppler observables at X-band and 60 s of count time. The plots represent the total numerical noise, plus the noise level due to each of the three error sources: representation of time (Time), position vectors (Range), and additional round-off errors (Additional). Note that the total noise curve is the square root of the sum of the three squared components.

The following considerations about MONTE numerical noise can be made:

- Due to the extended precision used for the representation of time variables, the Time component of the numerical noise in the radiometric observables becomes completely negligible. However, the Range and Additional components remain unchanged, with the Additional rounding errors as the most important sources of numerical noise.
- Considering the Cassini mission, the MONTE numerical noise increases with the spacecraft's heliocentric distance, reaching the maximum value of about  $7 \mu\text{m/s}$  at Saturn's arrival, at the middle of 2004. This value is about one order of magnitude smaller than the maximum ODP numerical noise, but is still larger than the best Cassini measurement accuracy of about  $4 \mu\text{m/s}$ , achieved during GWE [6]. Even considering the current best accuracy achievable by Cassini, which is about  $15 \mu\text{m/s}$  at 60 s integration time, the MONTE numerical noise is smaller but only by a factor of 2.
- Considering the Juno mission, the maximum value of the MONTE numerical noise is about  $3.5 \mu\text{m/s}$ , reached at Jupiter's arrival, at the middle of 2005. This value is about 20 times smaller than the maximum ODP numerical noise, but it is still comparable to the expected Juno measurement accuracy of  $1.2 \times 10^{-2} \text{ mm/s}$  at 60 s integration time [23].

Summarizing, MONTE numerical noise is more than one order of magnitude smaller than the ODP numerical noise, but it remains an important source of error in the precise orbit determination of current interplanetary missions.

## 2.6 Possible Strategies to Mitigate the Numerical Noise

On the basis of the developed model, three main strategies were identified to mitigate the numerical errors in the generation of the computed values of radiometric observables:

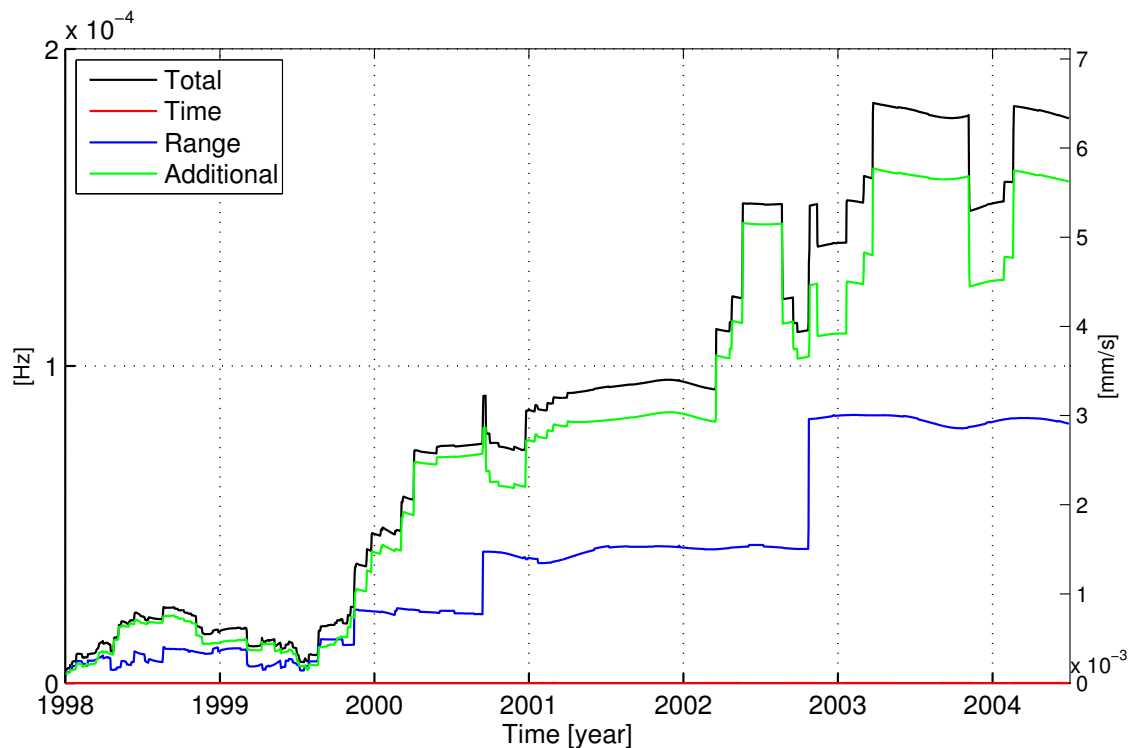


Figure 2.15: Numerical noise in Cassini's two-way Doppler observables ( $T_c=60$  s) during the cruise phase, from the beginning of 1998 to the middle of 2004.

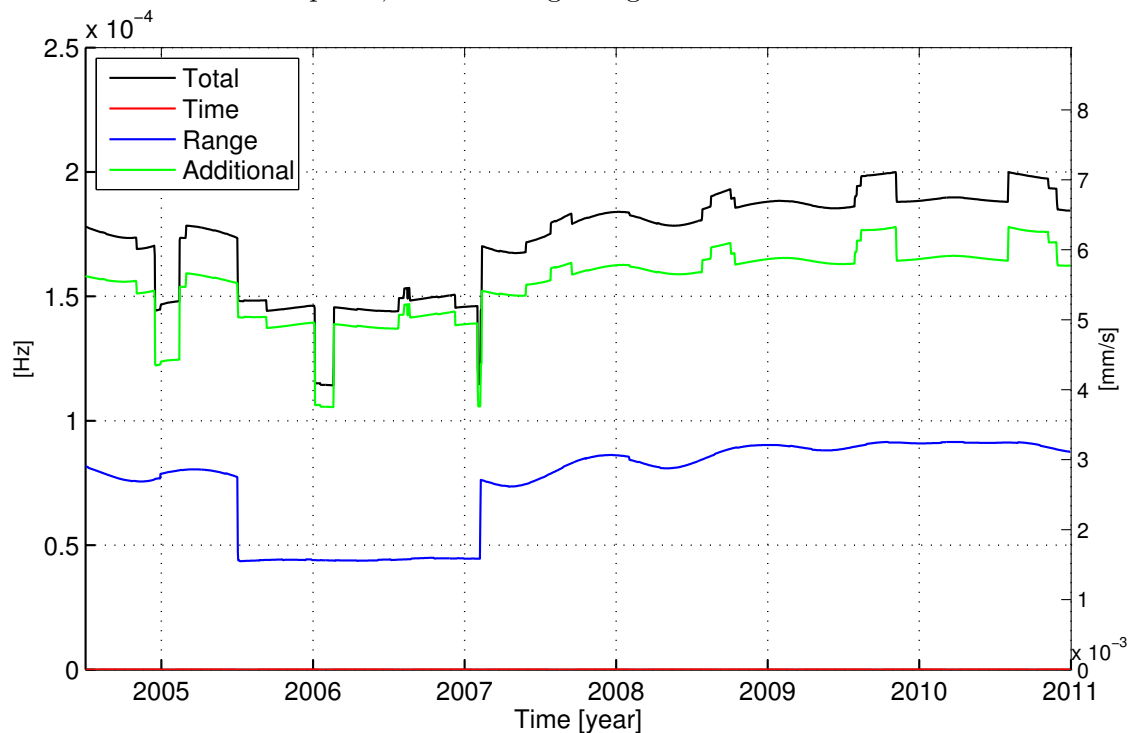


Figure 2.16: Numerical noise in Cassini's two-way Doppler observables ( $T_c=60$  s) during the Nominal Mission (from the middle of 2004 to the middle of 2008) and the Equinox Mission (from the middle of 2008 to the end of 2010).

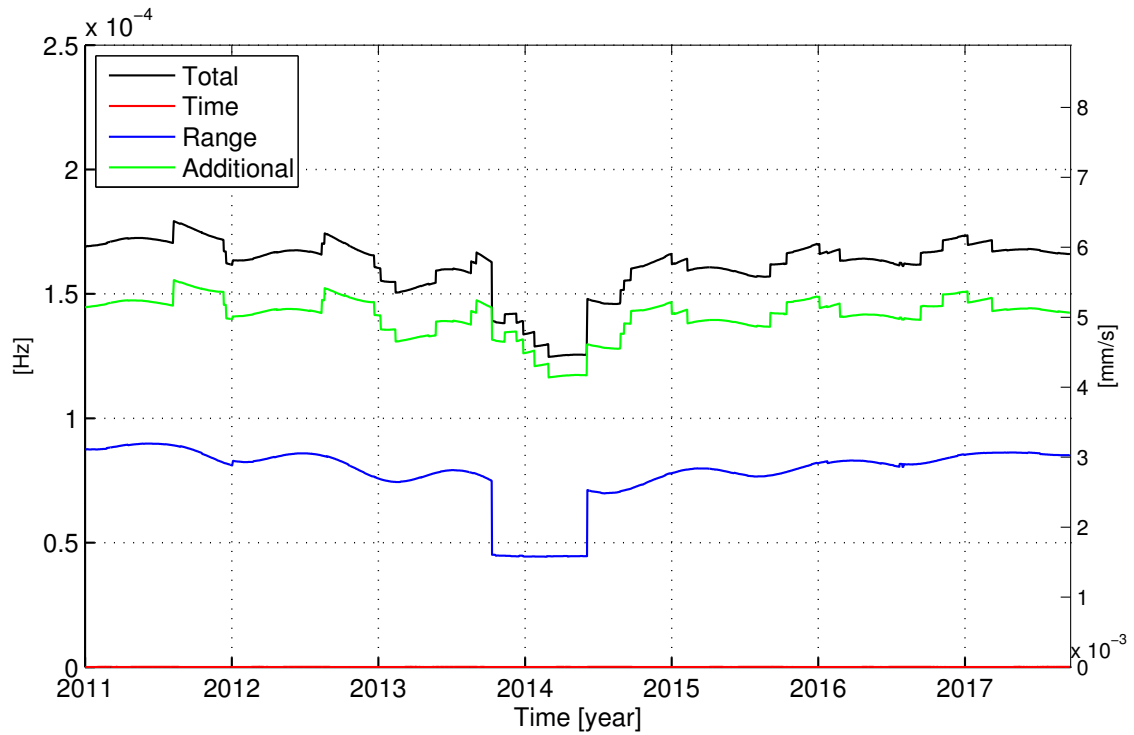


Figure 2.17: Numerical noise in Cassini's two-way Doppler observables (X-band,  $T_c=60$  s) during the Solstice Mission, from the end of 2010 to the end of 2017.

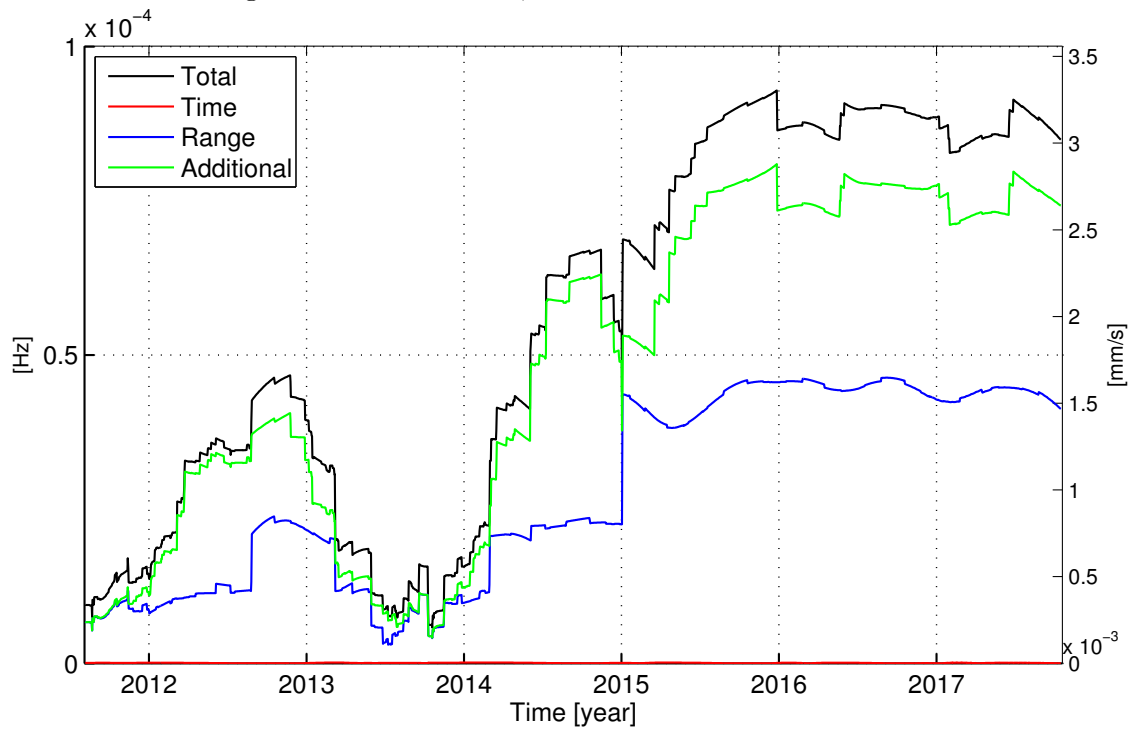


Figure 2.18: Numerical noise in Juno's two-way Doppler observables (X-band,  $T_c=60$  s) during the cruise phase, from the end of 2011 to the end of 2016.

- Compile the orbit determination program using a higher precision floating point representation. For example, moving from the double-precision to quadruple-precision representation, all round-off errors decrease by about a factor of  $10^{18}$ , becoming completely negligible. As a side effect, the execution time of the orbit determination process increases. However, because of the high complexity of the orbit determination codes, the increase in the execution time cannot be evaluated *a priori*, but must be assessed through dedicated experimental tests. Several approaches to reduce the execution time can be applied, like parallelization or recompilation in quadruple-precision of a limited subset of procedures, with further effects of increasing the complexity of the source code.
- Use an extended precision for the representation of variables. As a side effect, each operation explicitly involving time variables must be performed using custom functions, increasing the complexity of the source code. As an example, MONTE uses a double-double representation for the time variables. As shown in Chapter 2.5 for the Cassini and Juno missions, the Time component of numerical noise represents the most important contribution in interplanetary orbit determination problems. Hence, the numerical noise can be reduced by about one-order of magnitude changing only the time representation. However, this reduction may not be sufficient to support present missions like NASA's Juno, and future missions, like ESA's BepiColombo and JUICE, which are expected to reach accuracies of about  $12 \mu\text{m/s}$  at 60 s integration time or better, during most of their operational life.
- Use the Integrated Doppler formulation, which is much less influenced by numerical errors [49]. According to this formulation, the Doppler observable is computed expanding the Doppler frequency shift in a Taylor time series. Averaging over the count time, terms proportional to the odd powers of  $T_c$  become zero. Hence, retaining only terms up to  $T_c^2$ , the intrinsic error of the ID formulation increases with  $T_c^4$ . The maximum allowable count time depends on the specific orbit determination problem: for a desired accuracy of  $10^{-2} \text{ mm/s}$ , the count time has to be less than 1-10 s if the spacecraft is close to a planet or a satellite, while in heliocentric cruise much longer count times can be used, up to 1000 s [49]. On the contrary, the DRD formulation is theoretically exact, but is very sensitive to numerical errors, which increase as  $T_c^{-1}$  when reducing the count time. Hence, the numerical noise could be reduced using the ID formulation, but only at small count times. Moreover, the ID formulation can be only used with a constant uplink frequency. For most modern and future interplanetary missions, the uplink carrier frequency is varied in order to minimize the Doppler frequency shift observed by the spacecraft. The ID formulation is currently implemented only in AMFIN. It was implemented in older versions of the ODP, but it was then replaced by the DRD formulation.

## 2.7 Conclusions

In this chapter a study of numerical errors in two-way and three-way Doppler observables computed using the Moyer differenced-range Doppler formulation was described. This formulation is currently implemented in the most important interplanetary orbit determination programs: NASA/JPL's ODP (Orbit Determination Program) and MONTE (Mission-analysis, Operations, and Navigation Toolkit Environment), and ESA's AMFIN (Advanced Modular Facility for Interplanetary Navigation). A mathematical model of the numerical noise was developed. The model was validated analyzing directly the numerical noise in Doppler observables computed by the ODP and MONTE, extracted using a simplified fitting function, which was referred to as the "six-parameter fit". In particular, the model showed a relative error always smaller than 50%, with typical values better than 10%.

An accurate prediction of numerical noise can be used to compute a proper noise budget in Doppler tracking of interplanetary spacecraft. This represents a critical step for the design of future interplanetary missions, both for radio science experiments, requiring the highest level of accuracy, and spacecraft navigation. Moreover, the accurate prediction of numerical noise can also be used to identify enhancements in past radio science experiments, if an improved orbit determination code, less affected by numerical errors, could be used to reprocess past archived data.

As real-world scenario case studies, the expected numerical noise in the two-way Doppler link of the Cassini and Juno interplanetary missions was analyzed, both for the ODP and MONTE. As a result, the numerical noise proved to be, in general, an important source of noise in the orbit determination process and, in some conditions, it may become the dominant noise source. Hence, the application of dedicated strategies to reduce the numerical noise impact is considered mandatory, not only for future interplanetary missions, but also for the currently operational Juno, and to a lesser extent, for the Cassini missions. On the basis of the numerical errors characterization, three different approaches to reduce the numerical noise were proposed.

# Chapter 3

## A Multi-Arc Toolkit for MONTE

### 3.1 Introduction

MONTE is the new orbit determination software developed by the NASA/JPL to replace the old Orbit Determination Program (ODP). MONTE is based upon the same mathematical formulation of the ODP, with several differences in how the time variables are represented to reduce the numerical noise, as described in Chapter 2. However, the application of MONTE to the analysis of radio science gravity experiment is very recent, so new set-ups, toolkits and procedures were developed to perform this task. In particular, to analyze the data acquired during the Cassini gravity radio science experiments the use of a multi-arc procedure is fundamental while, at present, MONTE supports only a single-arc orbit determination approach. The multi-arc approach allows to improve the estimation of bias parameters with scientific relevance through the joint analysis of measurements acquired during non-contiguous orbital arcs. The `multiarc` library is a MONTE-Python library developed to extend the Monte capabilities to perform a multi-arc orbit determination.

The library provides a series of scripts and functions to easily:

- Set-up a multi-arc analysis, starting either from the correspondent single-arc analyses or from a generic already available MONTE-UI set-up.
- Adding more arcs to an already available multi-arc analysis, modifying all the necessary input files.
- Execute a multi-arc analysis, in a fully automatic and consistent way.

The `multiarc` library was developed and tested during the analysis of the Cassini radio science gravity experiments of Rhea, described in details in Chapter 4.

### 3.2 The Single-Arc Approach

Within the orbit determination, the first way to increase the accuracy and reliability of the estimation is to process more measurements, increasing the time span of the observations.

Within the gravity radio science, the estimation of the gravity field of a celestial body is performed analyzing data acquired during multiple fly-by, or “gravity experiments”. The fly-bys are usually separated by long time intervals, from months in the most favorable conditions, up to several years. As an example, during the entire Cassini-Huygens mission, only two fly-bys were dedicated to the gravity investigations of Rhea: R1, held in November, 2005, and R4, performed in March, 2013, after almost 8 years.

In principle, the trajectory of the spacecraft can be always considered as a single orbit, starting from a single set of initial conditions, no matter how long is the time interval. Using the standard single-arc approach, more observations are added increasing the length of the spacecraft orbit to reconstruct, from a single set of initial conditions that all the measurements contributes to estimate. In practice the single-arc approach has several limitations:

- Accumulation of modelization errors: the forces acting on a spacecraft are in general extremely complex, and usually they can be described by a deterministic model only over a limited time span, on which the modelization errors remain “small” with respect to the observational accuracy of the orbit determination. In particular, the main difficulty is the proper modelization of the non-gravitational forces acting on the spacecraft: in essence, there is no a single deterministic model capable to accurately model the non-gravitational perturbations [45]. Increasing the time span of the integration, the modelization errors accumulate and the reconstructed trajectory diverges from the real one. After a sufficiently long time, the model errors grow beyond observational errors becoming non-negligible and degrading the estimation. The modelization errors are usually absorbed through the so-called “stochastic parameters”, as a part of a batch-sequential filter-smoother. The stochastic parameters are parameters modeled as correlated random processes: they are constant over a so-called batch time interval, but their value and statistical properties are correlated to the other batches. At the end, after the smoothing process, for each batch a different estimate of the stochastic parameters is generated, but the estimation is a function of the measurements of all the batches. The main drawback of this approach is that the stochastic parameters are not real physical quantities, so that in the end the “stochastic” orbit determination is based on tuning a set of parameters without physical bases. Moreover, the stochastic parameters may adsorb also the observation errors and introduce a bias in the estimation of the other parameters.
- Increase of the number of parameters to estimate, with consequently degradation of the covariance matrix. In general, to reconstruct the trajectory over the entire time span of the spacecraft, additional parameters must be estimated, for example maneuver and range biases.
- Increase of the number of observations on which the parameters of interest are not observable. For example, the gravity field of a body is observable only around the closest approach of a limited number of fly-bys. In a single arc approach the tracking data between the fly-bys do not carry information of the gravity field, but are added only to estimate the trajectory itself.

An mathematically equivalent approach to the single-arc method is the batch-sequential method: the time span of the observations is divided into contiguous intervals called batches. Each batch is analyzed as a single arc, but using as apriori information the mapped solution and covariance matrix of the previous batch. A small variation of the pure batch-sequential method is the “fading memory” batch-sequential method, that consists in increasing the a priori covariance matrix of each batch by a scale factor. This corresponds to a single-arc approach on which the older observations are gradually de-weighted to conservatively increase the covariance matrix, to take into account modelization errors and too optimistic covariance models.

### 3.3 The Multi-Arc Approach

In the multi-arc approach the time span of the observations is divided into shorter, non-overlapping and non-contiguous intervals called arcs.

The parameters to be estimated are divided into two groups:

**Global parameters** , which do not vary with time and affect the measurements of all the arcs.

**Local parameters** , that affect only the measurements of an arc. In general, any parameter can be treated as local.

The spacecraft state at the beginning of arc is always considered a set of local parameters. In other words, the spacecraft trajectory of different arcs are considered as completely uncorrelated, as if they were different spacecrafts.

Hence, adding an arc results in:

- Increasing the number of estimated parameters, because of the new local parameters of the arc. This results in an over-parameterization that can absorb the models errors.
- Increasing the number of observations that depends upon the global parameters. This results in an improvements of their estimation.

Moreover, the arcs can be selected to maximize the accuracy and the reliability of the estimation of a set of global parameters, preferring arcs characterized by high information content:

- Favorable orbital geometry (fly-by).
- Low noise level.
- Less disturbing effects, like maneuvers.
- Limited length, in order to limit the model errors below the observational error.

As a drawback, the output of the multi-arc is not a continuous trajectory over the entire time span, but a series of unrelated, non-contiguous trajectory segments. The deterministic coherence of the spacecraft trajectory of the single-arc approach is replaced with a statistical-only type of coherence. Hence, the multi-arc cannot be used for operational navigation of the spacecraft.

From a mathematical point of view, the multi-arc method is just a simplified case of the general orbit determination problem, where the partial derivatives of the measurements of an arc with respect to the local parameters of the other arcs are zero. This results in a simple block structure of the filter matrices, which can be easily assembled from the single-arc corresponding matrices [60].

## 3.4 The Multi-Arc Monte Library

### 3.4.1 Implementation

Currently, as of version 089, Monte does not support the multi-arc approach. As stated before, the single-arc approach cannot be applied to analyze the radio science gravity experiments, because the different fly-bys are separated typically separated by long time intervals. The `multiarc` Monte-Python library was developed to extend the Monte capabilities to perform a multi-arc analysis. For the implementation, different approaches were analyzed and tested

#### 3.4.1.1 The “external” approach

The first method analyzed to implement the multi-arc method was the “external” approach [56]: for each separate arc Monte is used to integrate the spacecraft trajectory, compute the observables, the residuals and the partial derivatives of the residuals with respect to the parameters. Then, an external software reads the Monte outputs, extract the residuals and partials, properly build the multi-arc matrices and compute the multi-arc estimation and the corresponding covariance matrix through accurate numerical methods. The new estimation is then inserted in Monte to re-iterate the process. However, the basic idea of the development was to make use as much as possible of the tools and functions of Monte, without re-writing routines already available, tested and maintained by the JPL. For these reasons an “external” approach was discarded.

#### 3.4.1.2 The “multi-spacecraft” approach

Another approach analyzed to implement the multi-arc method was the “multi-spacecraft” approach, already developed and used with the ODP [46]: for each arc the spacecraft is considered as a different spacecraft, with a different name and, in general, different dynamical model. Monte is used to integrate all the spacecraft trajectories, compute the residuals and the partials, and to filter the measurements obtaining the multi-arc estimation. The difference between local and global parameters is “automatic”, because the different spacecrafts have different names.

A multi-arc filter must handle and estimate multiple state vectors. At present Monte implements a current state or pseudo-epoch state batch Kalman filter [47]. This formulation of the Kalman filtering equations is explained in [16]. The Monte filter supports different types of parameters:

- Parameters to estimate: parameters that the filter is allowed to change. The filter starts with an initial value and uncertainty (the covariance) for these parameters and will compute new values and their uncertainties. There are three types of estimated parameters:
  - Dynamic parameters: parameters that changes with time, i.e. parameters whose transition matrix is not the identity matrix. The dynamic parameters normally include body positions and velocities, masses, and attitudes for any number of bodies.
  - Bias parameters: parameters that are constant with time, i.e. parameters whose transition matrix is the identity matrix.
  - Stochastic parameters: bias parameters that are allowed to change over a known time interval. For a pseudo-epoch state batch filter, a stochastic parameter is treated as a piecewise constant parameter over some batch interval.
- Parameters to consider: parameters that the filter is not allowed to change, remaining constant during the analysis. The covariance of the consider parameters is included in the final, smoothed covariance of the estimated parameters. Usually they are parameters whose estimation cannot be improved through data, but whose uncertainty affects in a non-negligible way the uncertainty of the estimated parameters. Consider parameters may not be stochastic.

Hence, Monte supports an unlimited number of dynamical parameters, as required by the “multi-spacecraft” approach. However, this method cannot be implemented because, even if the Monte filter supports multiple spacecrafts, they must have the same reference epoch, i.e. they must be integrated from the same epoch.

#### 3.4.1.3 The “hybrid” approach

At present, as a part of the operational orbit determination process, the Cassini navigation team uses Monte also to update the Saturn’s satellites ephemerides, estimating new values of the satellite states. Unlike the Cassini state, the satellite states are always referred to a fixed reference epoch, changed every few years. At present the reference epoch is 01-OCT-2010 00:00 ET. The updated satellites ephemerides are generated numerically integrating the equations of motion using a Cowell’s method [53]. Also the partials of the satellite states are computed, numerically integrating the variational equations. To update the ephemerides, Monte must compute the partials of the residuals with respect to the satellite states at the reference epoch. For the filter, these parameters are dynamical parameters, but their partials are referred to a different epoch. To overcome this situation, the Monte filter handles these dynamical parameters as bias parameter. This is the same

approach of the classical epoch state batch filter, in which all the partials are always referred to a reference epoch. Using Monte nomenclature, the classical dynamical state parameters are identified using the model “State”, while the bias-dynamical parameters are identified with the “Ref State” model.

In the `multiarc` library, “Ref State” parameters were exploited to introduce dynamical parameters referred to different epochs, like the spacecraft states of the various arcs. Hence, an “hybrid” approach was used: as in the “external” approach, for each arc Monte is used to integrate the spacecraft trajectory and compute the residuals and the partials, which are processed from external routines. Then, as in the “multi-spacecraft” approach, the measurements are merged and processed by the standard Monte filter. This approach has the following advantages:

- The multi-arc analysis is well integrated with Monte, making use of the Monte routines to perform the most difficult and “delicate” phases of the orbit determination: trajectory integration, observables and partials computation, and filtering. The strict integration may be also a disadvantage: future updates of the software may break-up the `multiarc` library.
- The computations of the residuals and partials of each arc are separated and completely independent. In this way it is possible to easy remove, or modify a single arc, or even add a new arc from a single arc analysis already implemented. However, to correctly combine the single-arc residuals and partials, the dynamical models of all the arcs must be consistent. A special care must be dedicated to this problem, because the `multiarc` library is not able to verify the consistency of the arcs.

More details about the multi-arc procedure that was implemented are given in Chapter 3.4.2.

### 3.4.2 The Multi-Arc Analysis Procedure

The implemented multi-arc procedure is based upon the the basic idea of keeping conceptually and physically separate the single-arc and the multi-arc functions. Two “layers” are defined:

- The single-arc layer, inside which the residuals and the partials of each arc are computed. Each arc resides in a specific single-arc directory, that must contain a working Monte-UI set-up. Each arc can be considered as a standalone single-arc orbit determination analysis, without the filtering phase. The arcs are completely unrelated with each other.
- The multi-arc layer, inside which the residuals are combined and filtered. The multi-arc layer resides in a multi-arc directory, which usually contains also the single-arc directories. The multi-arc directory must contain a Monte-UI set-up defining the models necessary to perform the filtering phase and the global satellite ephemerides update, if requested.

A schematics of the multi-arc procedure implemented in the `multiarc` library is depicted in Figure 3.1. During the multi-arc orbit determination procedure the following steps are performed:

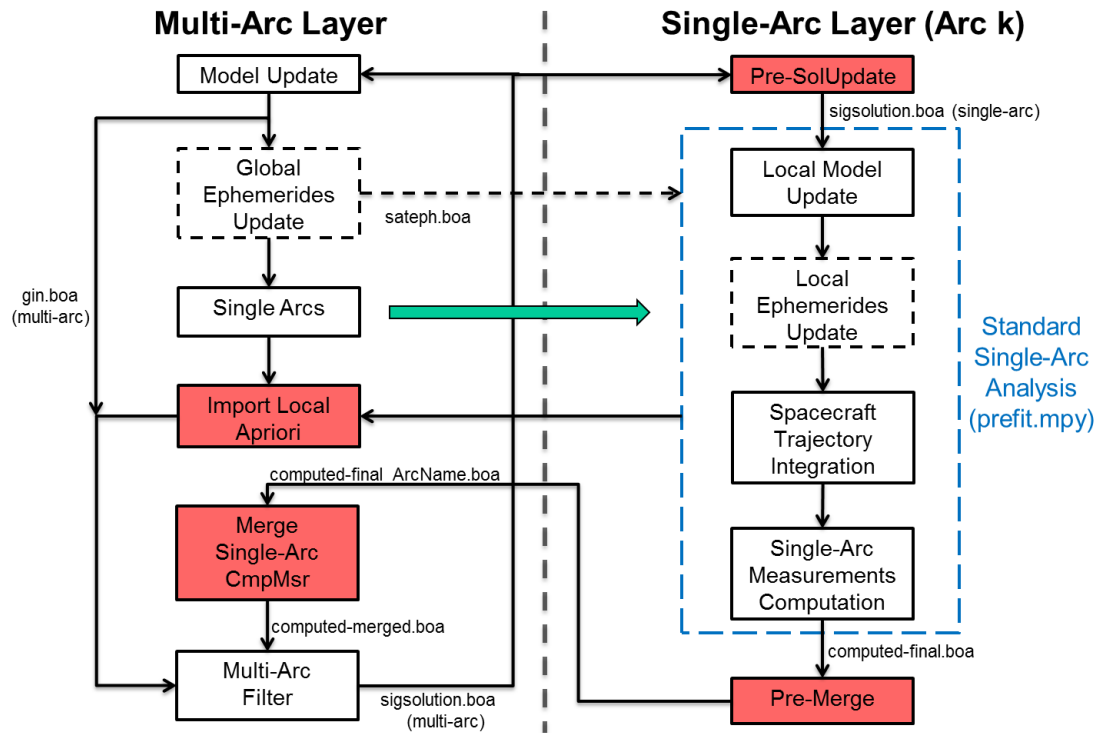


Figure 3.1: Block diagram of the multi-arc procedure implemented in the `multiarc` Monte-Python library. The red blocks are the original developed routines of the library.

1. Global dynamical model update, using the input namelists (only at the first iteration) or the multi-arc solution of the previous iteration.
2. Global satellite ephemerides update, if requested.
3. Single-arc residuals and partials computation. Inside each single-arc layer, the following steps are performed:
  - (a) Pre-solupdate: the global multi-arc solution is transformed to a single-arc solution for the corresponding arc (only after the first iteration).
  - (b) Local dynamical model update, using the input namelists (only at the first iteration) or the multi-arc solution of the previous iteration.
  - (c) Local satellite ephemerides update, if requested.
  - (d) Spacecraft trajectory propagation.
  - (e) Residuals and partials computation.
  - (f) Local editing and weighting of the single-arc residuals (optional).
  - (g) Pre-merge of the residuals: this original routine changes the name of the local parameters with respect to the partials are computed:
    - “State” parameters become “Ref State” parameters.
    - The spacecraft’s name is changed adding a suffix which identify the arc.

4. Import a priori values of the local parameters from the single arcs.
5. Merge of the single-arc residuals and partials.
6. Global editing and weighting of the merged residuals.
7. Estimation of local and global parameters.

### 3.4.3 Set-Up of a Multi-Arc Analysis

This section describes, from an operative point of view, the procedure to set-up a multi-arc analysis. To prepare a multi-arc analysis the following steps should be performed:

1. Create the multi-arc directory.
2. Add and configure the single arcs.
3. Configure the multi-arc `Options.mpy`.
4. Configure the multi-arc setup file.
5. Configure the filter.

Each step will be described in details in the following sections.

#### 3.4.3.1 Create the Multi-Arc Directory

The first step of the set-up is create a “multi-arc directory”, inside which the entire analysis will reside. At the end of the set-up phase the directory will contain:

- The single-arc directories (see Chapter 3.4.3.2).
- The multi-arc `Options.mpy`, based upon the specifications of the Cassini OD library 2.0, but with small modifications to control the multi-arc process (see Chapter 3.4.3.3).
- The multi-arc setup file (see Chapter 3.4.3.4).
- The filter configuration files (see Chapter 3.4.3.5).
- Other input files specified in the multi-arc `Options.mpy`.

The multi-arc directory can be created automatically using the command line script `prep_multiarc.py`. By default, the script will:

- Create a standard basic multi-arc directory.
- Create an empty `Options.mpy`, to be used as a template.
- Create an empty `multiarc_setup.mpy`, to be used as a template.
- Create an empty `filter_setup.mpy`, to be used as a template.

Optionally, it is possible to provide a source Monte working directory to use as a reference. This can be useful to define a dynamical model for global integrating the satellite ephemerides. In this case the script will also:

- Copy the content of the source `Options.mpy` inside the basic multi-arc `Options.mpy`.
- Copy all the needed input files.

In both cases the user must review and complete all the configuration files.

### 3.4.3.2 Add and Configure the Single Arcs

The second step of the set-up is to add and configure all the single arcs. For a correct multi-arc analysis at least two arcs are needed. However, a full multi-arc analysis can be completed without errors with only one arc. This can be useful for testing.

Each arc must reside entirely in a “single-arc directory”, placed inside the multi-arc directory. The single-arc directory must be a standard Monte-UI working directory. It must contain:

- The single-arc `Options.mpy` file, formatted according the specifications of the Cassini OD library 2.0.
- The necessary input files specified in the `Options.mpy`.

Each arc can be considered as a standalone single-arc orbit determination analysis, so it can be copied directly from an already configured Monte-UI case. In this case, the command line script `add_arc.py` can be used to automatically add a new arc from the source directory. The script must be executed inside the multi-arc directory. By default, the script will:

- Create the single-arc directory.
- Copy the source `Options.mpy`.
- Copy all the needed input files.
- Insert the basic arc information in the multi-arc `Options.mpy` (see Chapter 3.4.3.3).
- Insert the basic arc information in the multi-arc setup file (see Chapter 3.4.3.4).

Optionally, it is possible to provide a case number  $n$  of the source analysis to use as a lockfile. In this case the script will:

- Create the single-arc directory.
- Copy the `gin.boa.n` from the source `outputs/` directory to the target `lockfile/` directory.
- Copy all the needed input files.

- Create a custom `Options.mpy`.
- Insert the basic arc information in the multi-arc `Options.mpy` (see Chapter 3.4.3.3).
- Insert the basic arc information in the multi-arc setup file (see Chapter 3.4.3.4).

In both cases the user must review and complete all the configuration files.

### 3.4.3.3 Configure the Multi-Arc `Options.mpy`

The computation of the residuals and partials is performed in the single arcs. Hence, the multi-arc `Options.mpy` is used to set-up only the information needed for the multi-arc layer of the analysis:

- A dynamical model for the global satellite ephemerides update, if requested.
- The multi-arc setup file (see Chapter 3.4.3.4).
- Global editing and weighting commands for the merged residuals.
- The filter configuration.
- The a priori covariances, for both the global and local parameters.
- The a priori values of the global parameters only. The a priori values of the local parameters are automatically imported from the single arcs.

Moreover, the following variables must be defined in the multi-arc `Options.mpy`:

- `ARC_EPOCH`: the epoch of the first arc, in string format.
- `ARC_END`: the end of the last arc, in string format.

If an arc is added using the command line script `add_arc.py`, these variables are automatically updated.

### 3.4.3.4 Configure the Multi-Arc Setup File

The multi-arc setup file specifies the basic information of the single arcs needed to perform the multi-arc analysis. It must define a Python list named `ARCS` that, for each arc, contains a list with the following data:

- A name to identify the arc, without spaces or special characters.
- The name of the single-arc directory, relative to the multi-arc directory.
- The epoch of the arc, in string format.
- The end of the arc, in string format.
- A list of the local parameters of the arc, in string format.

If an arc is added using the command line script `add_arc.py`, the basic arc information will be automatically added to the list `ARCS` inside the file `multiarc_setup.mpy`, if present. The list of the local parameters will include only the initial state of the spacecraft. After adding the arc the user must review and if necessary complete the multi-arc setup file.

### 3.4.3.5 Configure the Multi-Arc Filter

The next step of the multi-arc set-up is the configuration of the filter. To jointly process the residuals and the partials of multiple arcs, the name of the single-arc parameters is changed before the merging:

- All the “State” parameters are renamed to “Ref State”. Hence, all the dynamical parameters, both global or local, will be treated as bias in the filter.
- The second key of the local parameters is renamed, adding as suffix the identification string of the arc provided by the multi-arc setup file.

Due to the changes described above, the filter must be configured using a standard Monte-UI setup, but with the following differences:

- The list of dynamical parameters must be empty.
- The parameters, both bias and considered, must be inserted with their modified name.

At present the `multiarc` library does not support the stochastic parameters. No stochastic parameters must be added to the filter.

For each parameter in the filter state, the a priori value and the covariance must be provided:

- The a priori value of the global parameters must be defined in the multi-arc model, through the multi-arc `Options.mpy`.
- The a priori value of the local parameters will be automatically imported from the single arcs. At present the a priori value of the local parameters can be automatically imported from the single arcs only for the following parameters:
  - Initial integration states: `'State/Body/Center/Frame/Param'`.
  - Mass parameters: `'Mass/Body'`.
  - Gravitational parameters: `'Gm/Body'`.
  - Spherical Harmonics: `'Gravity/Body/Param'`.

For the other parameters a model with the a priori values must be provided in the multi-arc `Options.mpy`.

- The apriori covariance of both global and local parameters must be defined in the multi-arc model. The apriori covariance of the local parameters will not be imported from the single arcs.

### 3.4.4 Analysis Execution

Completed the set-up phase, the multi-arc analysis will be performed executing the command line script `estim_ma.mpy` inside the multi-arc directory. This script executes `prefit_sa.mpy` to generate the observables of the single arcs, then combines these observables and perform a global filter. The user can specify:

- the number of iterations to perform.
- the type of satellite ephemerides update.

For each arc, the outputs and log files will be created in the `outputs/` folder of the corresponding single-arc directory. The outputs and log files of the multi-arc process will be created in the `outputs/` folder of the multi-arc directory.

### 3.4.5 Current Limitations

At present, the `multiarc` library has the following limitations:

- The stochastic parameters are not supported.
- The a priori value of the local parameters can be automatically imported from the single arcs only for the following parameters:
  - Initial integration states: `'State/Body/Center/Frame/Param'`.
  - Mass parameters: `'Mass/Body'`.
  - Gravitational parameters: `'Gm/Body'`.
  - Spherical Harmonics: `'Gravity/Body/Param'`.

For the other parameters a model with the a priori values must be provided in the multi-arc `Options.mpy`.

- The filter does not support mappings.
- The center of integration of the spacecraft and satellites must be constant. This is because currently “Ref State” parameters do not support arbitrary center mappings [47].

## 3.5 Conclusions and Future Work

Monte, the orbit determination software developed by the JPL, does not support natively the multi-arc method (as of version 089). The `multiarc` Monte-Python library was developed to extend the standard Monte capabilities to perform a multi-arc analysis.

The `multiarc` library has the following characteristics:

- Developed in python programming language.

- Strictly integrated with Monte, because it uses the Monte routines, developed, tested and maintained by the JPL, to perform the most important phases of the orbit determination:
  - Spacecraft trajectory integration.
  - Satellites ephemerides update.
  - Residuals and partials computation.
  - Residuals filtering and estimation.
- The `multiarc` library provides a series of routines to easily:
  - Set-up a multi-arc analysis, from an already working set-up or from empty standard templates.
  - Add more arcs to a multi-arc analysis from an already available single-arc analysis.
  - Configure the single-arc layer and the multi-arc layer.
  - Perform the analysis, automatizing all the multi-arc procedure.

The `multiarc` library was developed and successfully tested during the analysis of the Cassini radio science gravity experiments of Rhea, described in details in Chapter 4.

Regarding the future work, the development and testing of the `multiarc` library is still ongoing. In particular, the following desired features are identified:

- Support for stochastic parameters.
- Support for variable centers of integration.
- Native support for more local parameters.
- Easy implementation of custom observables.
- Application to other missions than Cassini, like Juno of NASA, Bepi Colombo, and JUICE of ESA.



# Chapter 4

## Rhea Gravity Field from Cassini Data Analysis

### 4.1 Introduction

Discovered on December 23, 1672 by Giovanni Domenico Cassini, Rhea is the second largest moon of Saturn, given a mean radius of about 764 km. The main orbital and physical characteristics of Rhea are presented in Table 4.1[68][37].

Table 4.1: Orbital and physical characteristics of Rhea.

Semi-major axis	( km)	527108
Orbital Period	( d)	4.518
Rotation Period		synchronous
Eccentricity		0.0012583
Inclination	( deg)	0.345
GM	( km <sup>3</sup> /s <sup>2</sup> )	153.9426 ± 0.0037
Mean Radius	( km)	764.30 ± 1.10
Mean Density	( kg/m <sup>3</sup> )	1233 ± 5
Geometric Albedo		0.949 ± 0.003

The first pictures of Rhea were taken by Voyager 1 and Voyager 2 probes, in 1980 and 1981. Images showed that the surface of Rhea can be divided into two regions: the leading hemisphere is uniformly bright and is heavily cratered, while the trailing hemisphere is darker, with smaller craters. The difference may indicate that a major resurfacing event occurred some time in past Rhea's history.

Before the Cassini arrival to Saturn, only the gravitational parameter GM was estimated, from an analysis of Pioneer and Voyager data, obtaining  $GM = 154 \pm 4 \text{ km}^3/\text{s}^2$  [18]. Considering a mean radius of  $764 \pm 4 \text{ km}$ , the mean density was  $1236 \pm 4 \text{ kg/m}^3$ , relatively small and compatible with a mixture of about 75% water ice (density  $1000 \text{ kg/m}^3$ ) and 25% rock-metal (density  $3000 \text{ kg/m}^3$ )[2].

During its mission in the Saturn's system, Cassini encountered Rhea four times, but only two flybys were devoted to gravity investigations. The first gravity flyby, referred to as R1 according to the numbering scheme used by the project Cassini, was performed on November 26, 2005, during the main mission. R1 was characterized

by a very low inclination, about 17 deg at the C/A, and an altitude of about 502 km at the C/A, which corresponds to a radius of about 1.6 Rhea radii ( $R_R$ ). The main orbital and geometrical characteristics of R1 are summarized in Table 4.2.

The radiometric data acquired during this encounter were used to estimate the gravity field of Rhea. A first estimate was published by [3]. This solution was obtained with the assumption of hydrostatic equilibrium, i.e. constraining  $J_2$  and  $C_{22}$  to a ratio of 10/3. From the estimation, applying the Radau-Darwin relation the authors obtained a normalized moment of inertia of about  $0.3911 \pm 0.0045$ , where a value of 0.4 derives from a constant density interior. The authors concluded that the satellite’s interior is a homogeneous, undifferentiated mixture of ice and rock, with possibly some compression of the ice and transition from ice I and ice II at depth.

Moreover, the radiometric data acquired during R1 were independently analyzed by the Cassini Navigation team [39] and by the Cassini Radio Science team [31]. Both analysis estimated the moon’s  $GM$  and quadrupole gravity coefficients  $J_2$  and  $C_{22}$ , obtaining different solutions, but consistent at the  $2\sigma$  level, as the result of different analysis approaches. The two approaches were then combined to obtain a joint “best” unconstrained estimation of the quadrupole field [40]. The solution obtained was not statistically compatible with the hydrostatic equilibrium, hence no useful constraint on Rhea’s interior structure could be imposed. Moreover, the application of the hydrostatic constraint led to a significant degradation of the orbital fit at the closest approach. To explain the non-hydrostatic ratio  $J_2/C_{22}$  the authors theorized that a large collision occurred after the completion of the thermal evolution of the satellite could have created a mass redistribution and a reorientation of the tidal bulge.

Finally, [4] stated that the differences in the previously published gravity fields are probably caused by a mis-modeling of the non-gravitational acceleration acting on Cassini caused by the anisotropic thermal emission. To avoid this issue, the authors restricted the analysis to a subset of data around the closest approach, where the information of Rhea’s quadrupole field is not negligible. They obtained a new solution in agreement with [3], using the hypothesis of hydrostatic equilibrium. Moreover, the authors concluded that the non hydrostaticity is not supported by the data.

The different estimations of  $J_2$  and  $C_{22}$  published to date are showed in Figure 4.1.

To resolve these discrepancies, a second and last gravity fly-by, referred to as R4, was planned in the Solstice mission and performed on March 9, 2013. No other gravity flybys of Rhea are scheduled up to the end of the mission in 2017. To de-correlate the estimation of  $J_2$  and  $C_{22}$  R4 was designed to be nearly polar, with a high inclination at the C/A, about 106 deg. However, the altitude at the C/A was about 999 km, which corresponds to a radius of about  $2.3 R_R$ , which is smaller than R1. The main orbital and geometrical characteristics of R4 are summarized in Table 4.2, while Figure 4.2 presents the ground track of the two fly-bys, for a time interval of about 4 h around the closest approaches. The Sun-Earth-Probe (SEP) angle was greater than 110 deg during both the encounters, thus the solar plasma noise was not a dominant source of noise on range rate measurements.

This chapter presents the estimation of the Rhea’s gravity field obtained from

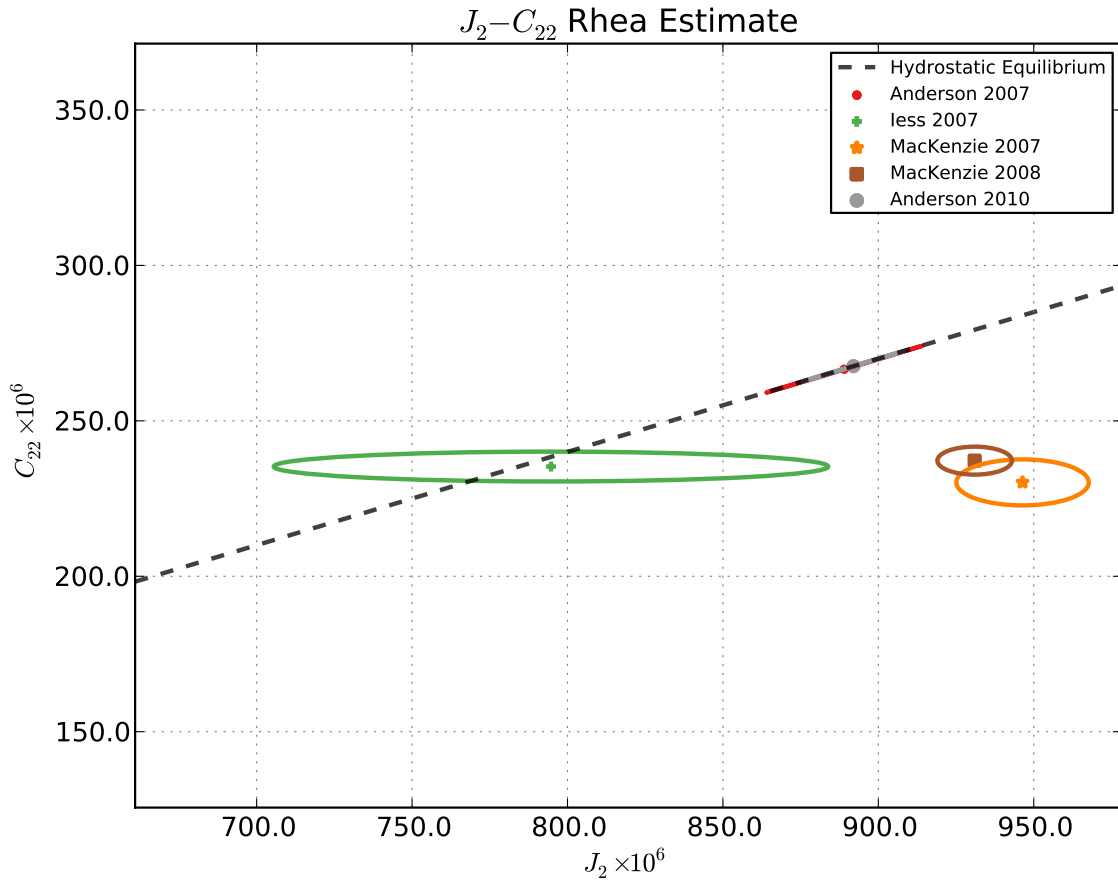
Figure 4.1: Estimations of Rhea  $J_2$  and  $C_{22}$  published to date.

Table 4.2: Main orbital and geometrical characteristics of R1 and R4.

		<b>R1</b>	<b>R4</b>
<b>Date (ERT)</b>	(UTC)	26-NOV-2005, 23:50	09-MAR-2013, 19:40
<b>Altitude</b>	(km)	502	999
<b>Radius</b>	(km)	1266	1763
<b>Radius</b>	( $R_R$ )	1.6	2.3
<b>Relative Velocity</b>	(km/s)	7.3	9.3
<b>Inclination</b>	(deg)	17	106
<b>Latitude</b>	(deg)	-10.2	18.8
<b>Longitude</b>	(deg)	-91.5	-176.2
<b><math>\beta</math> Angle</b>	(deg)	106	117
<b>SEP Angle</b>	(deg)	113	128

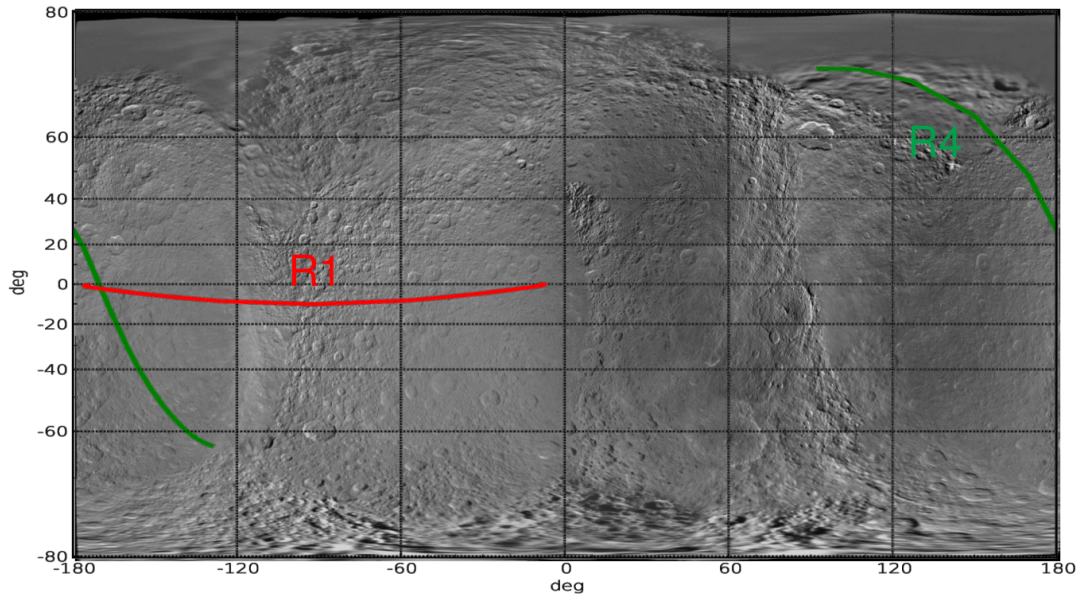


Figure 4.2: Ground tracks of R1 and R4 Cassini fly-bys of Rhea.

a joint analysis of the two flybys. The analysis was carried out using Mission-analysis, Operations, and Navigation Toolkit Environment (MONTE), the new orbit determination software developed by the Jet Propulsion Laboratory (JPL) to replace the old Orbit Determination Program (ODP). MONTE is based upon the same mathematical formulation of the ODP, with several differences in how the time variables are represented to reduce the numerical noise, as described in Chapter 2. However, the use of MONTE in the analysis of radio science gravity experiment is new: completely new scripts, work methods and set-ups were produced during this work. At first a single arc, independent, analysis of R1 was performed. In this way, the new MONTE setup of the gravity analysis was tested comparing the estimated gravity field with the published results available in literature. Then, a second solution was obtained through a single arc analysis of R4. A second independent solution, based on different data, is useful to check the correctness of the set-up, because it may highlight systematic modelization errors that can be absorbed analyzing a single, short, data arc. Finally, data from both R1 and R4 were combined into a multi-arc solution. The multi-arc analysis was carried out using the newly developed multi-arc toolkit for MONTE, described in details in Chapter 3. To test the stability of the solution, different multi-arc analysis were performed, varying the data set, the strategy for the update of the satellite ephemerides and the dynamical model.

## 4.2 Dynamical Model

To correctly estimate the orbit of Cassini, the dynamical model implemented in the orbit determination program must take into account all the non-negligible accelerations acting on the spacecraft. In this section a brief description of all the non-negligible forces acting on Cassini during a satellite fly-by is given.

### 4.2.1 Gravitational Accelerations

The implemented dynamical model includes the gravitational acceleration from all the main solar system bodies and from the main satellites of Saturn. In particular, the following effects were activated:

- Newtonian point-mass gravity acceleration from the Sun, the planets, the Moon and Pluto.
- Newtonian point-mass gravity acceleration from the Saturn's satellites Mimas, Enceladus, Tethys, Dione, Rhea, Titan, Hyperion, Iapetus, Phoebe.
- Newtonian gravity acceleration due to spherical harmonics of Saturn and Rhea.
- The Newtonian gravitational accelerations due to the Saturn's rings are included in the Saturn's gravity field.
- Relativistic point-mass gravity acceleration caused by the Sun, Jupiter, Saturn and its main satellites.

The periodic tidal effects of Saturn on Rhea were not activated, because the eccentricity of Rhea's orbit is very small: in this condition the tidal bulge is almost constant, function of the secular Love's number  $k_f$  [38], while the elastic response, function of the tidal Love's number  $k_2$ , cannot be determined, at least with only two fly-bys available.

The gravitational parameters and state vectors of the planets, the Sun, the Moon and Pluto were obtained from JPL planetary ephemerides DE430 [24]. The gravitational parameters and a priori state vectors of Saturn and its main satellites were obtained from the Saturn's satellites ephemerides SAT355 provided by the Cassini Navigation Team by fitting a large number of radio and optical and data<sup>1</sup>. The satellite ephemerides provide also the Saturn's even zonal spherical harmonics from  $J_2$  up to  $J_8$  and an updated model of the Saturn's rotation.

The a priori values for Rhea's GM and spherical harmonics were retrieved from [40]. However, a large a priori uncertainty was used, in order to not constrain the solution.

#### 4.2.1.1 Rhea Rotation Model

Given the very small eccentricity (about 0.001), Rhea is supposed to be in synchronous rotation around Saturn, with the rotation axis normal to the orbital plane and prime meridian always oriented toward Saturn. The rotational model adopted was based on the latest coordinate orientations adopted by the IAU [5], with small corrections were applied to obtain a better fit of Cassini and other astrometric data [36]. The adopted Rhea rotational model is reported in Eq. 4.1.

---

<sup>1</sup>Available at <ftp://ssd.jpl.nasa.gov/pub/eph/satellites/>.

$$\alpha_0(\text{deg}) = 40.347 - 0.17089132T - 2.958 \sin S7 + 0.076 \sin S12 \quad (4.1)$$

$$\delta_0(\text{deg}) = 83.550 - 0.01277063T - 0.332 \sin S7 + 0.004 \sin S12 \quad (4.2)$$

$$W(\text{deg}) = 235.16 + 79.69005069d + 2.941 \sin S7 - 0.077 \sin S12 \quad (4.3)$$

Where:

- $\alpha_0$ : right ascension of the north pole with respect to EME2000.
- $\delta_0$ : declination of the north pole with respect to EME2000.
- $W$ : angle measured easterly along the body's equator between the prime meridian and the ascending line of nodes.
- $T$ : time measured in Julian centuries (36525 days) past J2000.
- $d$ : time measured in days past J2000.
- $\sin Si$ : nutation-precession terms, whose argument is given by Eq. 4.4.

$$S7(\text{deg}) = 9.151048 + 1004.6342250T \quad (4.4)$$

$$S12(\text{deg}) = 18.302096 + 2009.2684500T \quad (4.5)$$

A dynamically defined, perfectly synchronous, rotational model was also used, but the solution was not affected significantly.

## 4.2.2 Non-Gravitational Accelerations

The most important non-gravitational forces acting on Cassini are:

- Orbital maneuvers, used to change the trajectory of Cassini within the Saturn's system.
- Unbalanced thrust during attitude and reaction wheel desaturation maneuvers implemented with the thrusters.
- Anisotropic thermal emission of Cassini, in particular caused by the RTG and the geometry of the spacecraft.
- Solar radiation pressure.
- Saturn's planetary albedo.
- Drag caused by planetary and satellite atmospheres.

### 4.2.2.1 Maneuvers

During the orbit determination, any maneuver that may affect the spacecraft center of mass must be estimated. Adding additional elements to the state vector degrades the estimation, because of the correlation between the parameters: the formal covariance matrix increases and biases, due to systematic errors, may be added. Hence, to maximize the accuracy of the gravity field estimation, gravity radio science experiments were planned without the presence of any maneuver. Moreover, even when navigation data is added, the data arc used in the analysis never include these kind of forces.

### 4.2.2.2 RTGs

The three onboard Radio-isotopes Thermal Generators (RTG) provides electrical power to Cassini through natural radioactive decay of an isotope of Plutonium. The thermal power generated by the RTGs is radiated into space. The spacecraft BUS is insulated through an insulating blanket and reflects most of the thermal radiation. Other parts of the spacecraft, like the HGA both absorb and reflect the thermal emission. The global thermal emission of the spacecraft is not isotropic, giving rise to an acceleration because the thermal radiation carries momentum. Due to the spacecraft geometry, the main effect is an acceleration along the spacecraft Z body-fixed axis of about  $5 \times 10^{-12} \text{ km/s}^2$  [21]. The asymmetric spacing of the RTGs produces also smaller, by a factor of 3, but non-negligible accelerations along the X-Y plane, mainly along X axis. In the orbit determination software MONTE, the RTG acceleration is modeled as an exponential decaying acceleration, of the form:

$$\ddot{\mathbf{r}} = M_R \left( A_r \hat{\mathbf{Z}} + A_x \hat{\mathbf{X}} + A_y \hat{\mathbf{Y}} \right) e^{-\beta \Delta t} \quad (4.6)$$

where:

- $M_R$ : ratio between the mass at  $t = 0$  and the current mass.
- $A_r$ : acceleration along the spacecraft Z axis at  $t = 0$ .
- $A_x$ : acceleration along the spacecraft X axis at  $t = 0$ .
- $A_y$ : acceleration along the spacecraft Y axis at  $t = 0$ .
- $\beta$ : exponential time scale factor. The value used in this analysis is provided in Table 4.3.

More details about the mathematical modelization of the RTG accelerations can be found in [22] and [21]. In this analysis the coefficients  $A_r$ ,  $A_x$  and  $A_y$  estimated by the Cassini navigation team were used. Their value is presented in Table 4.3. New values for the RTGs acceleration were not estimated, because from only two fly-bys is not possible to improve their estimation. Moreover, the time scale of the acceleration is much greater than the duration of the gravity experiments: during the fly-by the RTG accelerations can be considered constant. Hence, they do not affect the estimation of the gravity field, because the correlation is very low.

Table 4.3: Coefficients defining the Cassini RTG acceleration.

$\beta$	( $s^{-1}$ )	$2.5 \times 10^{-10}$
$A_r$	( $km/s^2$ )	$-3.00e - 12$
$A_x$	( $km/s^2$ )	$-9.33e - 13$
$A_y$	( $km/s^2$ )	$-1.07e - 13$

#### 4.2.2.3 Solar Radiation Pressure

Solar photons carry momentum so, when the solar radiation impacts the surfaces of Cassini it transfers momentum to the spacecraft, generating an acceleration well above Cassini acceleration sensitivity. The value of this acceleration depends upon the amount of incident radiation that is specularly reflected, absorbed and diffusively reflected, which depend upon the spacecraft geometry and the thermo-optical properties of the surfaces. A proper general modelization of the solar pressure is extremely difficult, because the thermo-optical properties are difficult to measure and because of the interaction between the different surfaces. Fortunately, during the tracking passes, Cassini points the HGA toward the Earth: the frontal area is dominated by the two magnetometer booms and the HGA, which alone accounts for the 90% of the total frontal area. The HGA surface is accurately modeled as a parabolic antenna, while the booms are modeled as simple cylinders. The thermo-optical properties of the surfaces were measured and extrapolated during ground tests, while their variation is inferred from temperature readings of two sensors mounted on the HGA back side. More details about the mathematical modelization of the solar radiation pressure can be found in [22] and [21]. As the RTGs accelerations, new values of the solar pressure coefficients were not estimated, because the low observability due to the limited amount of data and the low correlation with the Rhea gravity field.

#### 4.2.2.4 Saturn Albedo

As the solar radiation, the Saturn's thermal radiation incident on Cassini transfers momentum and produces a non-gravitational force. The resulting is of the order of  $10^{-16} km/s^2$ , increasing up to  $5 \times 10^{-15} km/s^2$  near Saturn pericenter [21]. Hence the planetary albedo is absolutely negligible, because its maximum value is three order of magnitude smaller than the RTGs acceleration.

#### 4.2.2.5 Atmospheric Drag

Within the Saturn's system, only Saturn and Titan have a non-negligible atmosphere. Hence, during a Rhea fly-by the drag is not present and the model was not activated.

## 4.3 Satellite Ephemerides Update

Within the orbit determination process Rhea's ephemerides were updated. Rhea is orbiting around Saturn in an almost circular orbit, with a semi-major axis of

527108 km, about  $690 R_R$ . The sphere of influence of Rhea can be estimated using as the Hill's radius  $R_H$ :

$$R_H = a\sqrt{\frac{GM}{3GM_P}} \simeq 5830 \text{ km} \simeq 7.6 R_R \quad (4.7)$$

where  $GM$  and  $GM_P$  are the gravitational parameters of Rhea and Saturn, respectively. During R1 and R4 Cassini is within the Rhea's sphere of influence, where the gravity accelerations can be considered dominated by the satellite, for a time interval of about 40 min and 30 min around the closest approach. Hence, for almost the entire duration of the arcs, the gravitational accelerations of Saturn and Rhea are comparable. The trajectory of Cassini is strictly related to the relative position between Cassini, Rhea and Saturn. The state of Cassini is obtained integrating the spacecraft equations of motion, given the dynamical model described in this section. The state of Rhea, all the other satellites and Saturn is retrieved from the Saturn satellite ephemerides, obtained numerically integrating the satellites equations of motion using the Cowell's method [53]. The Saturn's satellite ephemerides are obtained fitting a large number of astrometric, optical and radiometric measurements, obtained from different sources through a large time span of data. However, the ephemerides of the different satellites have different accuracies, given the different number and accuracy of the observations available. Moreover, the accuracy degrades away from the time span covered by observations. For this reason, to correctly fit the data, both the relative states of Cassini and Rhea with respect to Saturn must be estimated. Given a new state of Rhea, the satellite ephemerides of the Saturn's system have to be updated. The new ephemerides are generated using the same routines used by the JPL team to create the official satellite ephemerides [35].

When multiple fly-bys, separated by a quite long time (8 years for Cassini R1 and R4), are analyzed using a multi-arc method, two approaches are available: the global method and the local method. The global approach is the conventional method, used in the past for all the analysis of the gravity radio science experiments [31, 33, 40]. Using this approach, when generating new ephemerides the satellites states is integrated for the entire time span covered by the data arc, from an epoch prior to the first fly-by, to after the last fly-by. This approach ensures that the satellite trajectory is internally coherent. However, following this conventional procedure, a new state of only one satellite is estimated. Moreover, usually the a priori covariance matrix of the satellite is diagonal: this approach neglects the correlations with all the other satellites. Moving the initial state of only one satellite and integrating the equations of motion, the orbits of all the satellite change, because of the relative gravitational interactions. This could in principle change the fit of all the other data, astrometric, optical and radiometric are completely neglected. Hence, the updated ephemerides do not represent an "improved" version of the satellite ephemerides, but the orbits that allows to better fit only the data under analysis. Moreover, the integration of the updated satellite ephemerides over a long time span is a long process (about 15-20 minutes for a single integration over 8 years), and it slows down the analysis.

For these reasons, a novel local approach was developed and tested. Using this approach, the state of the satellite is treated as a local parameter of a multi arc analysis. For each fly-by, not only a different state of Cassini, but also a

different state of Rhea are estimated. After the estimation, new satellite “local” ephemerides are generated for each fly-by, integrating from the new states for a time span that covers the only corresponding fly-by. This approach does not ensure that the satellite trajectory is strictly coherent but, as for the spacecraft trajectory in the classic multi-arc analysis, the deterministic coherence is replaced by a stochastic coherence. If the differences of the orbits are within the uncertainty of the ephemerides, the two orbits are compatible from a statistical point of view. For the purpose of the estimation of the satellite gravity field the local approach can be considered fully equivalent to the global approach. In fact, as for the global approach, the updated local ephemerides represent only the satellites orbits that provides a better fit of the analyzed data. Moreover, the epoch of the satellite can be chosen just before the fly-by, usually coinciding with the epoch of the spacecraft state, to reduce the time for the integration. For an arc of about 3 days, the satellite integration is almost instantaneous.

## 4.4 Data

### 4.4.1 Data Selection

The main observable quantity used in the gravity estimation was the spacecraft range rate, also called Doppler. The Doppler observable is the frequency shift due to relativistic Doppler effect, averaged over a finite count time, of a highly stable microwave carrier transmitted from an Earth ground station to the spacecraft, that coherently retransmits the signal to Earth by means of a precise transponder. Range observables were not used in the analysis because they have a very limited use in the estimation of gravity fields. In fact, the estimation of the gravity field is strictly related to the reconstruction of the accelerations acting on the spacecraft. Doppler measurements provide a measure of the variation of the spacecraft velocity. The same information can be obtained through range measurements, but with much less accuracy than range rate, due to the random errors. Moreover, while range-rate is a relative measurement, range is an absolute measurement of the light-time, thus is sensitive to systematic errors. At present, for Cassini-era range systems, the accuracy is limited by the interplanetary plasma and the delays of ground station and spacecraft electronics, that can be up to 2 m [69]. For this reason, in spacecraft navigation is a common procedure to estimate a range bias for each tracking pass. However, in gravity radio science, this may introduce biases in the estimation of the gravity field.

During the encounters Doppler data in X (8.4 GHz) and Ka band (32.5 GHz) were acquired by the antennas of the NASA’s Deep Space Network (DSN) at the three complexes of Goldstone, Madrid and Canberra. In addition to data obtained around the closest approach, the analysis used also data obtained up to two day before and after the closest approach, during standard navigation tracking passes. The additional data allow to improve the orbit determination, in particular the estimation of Rhea’s ephemerides and Rhea’s  $GM$ , because of the stronger constraints that impose on the relative trajectories between Cassini, Rhea and Saturn.

The detailed timeline of R1 and R4, showing the elevation with respect to the three DSN complexes and the tracking passes, is presented in Figure 4.3. It is important to note that the closest approach of R1 was tracked only in three-way mode. This represents a sub-optimal condition, due to the possible delay between the reference oscillators of the two different uplink and downlink stations. During R4, the closest approach was tracked in two-way mode.

Dual frequency X-band uplink and Ka-band downlink (X/Ka) Doppler data were preferred to the standard X/X data when available, to reduce the effects of the dispersive noise sources, mainly the solar corona and the the Earth ionosphere. Two-way Doppler data were preferred to three-way data in the same band when both were available, to remove the errors due to the clock synchronization between the uplink and downlink ground stations. When only two-way X/X data and three-way X/Ka data were available, the selection was made on a case by case basis.

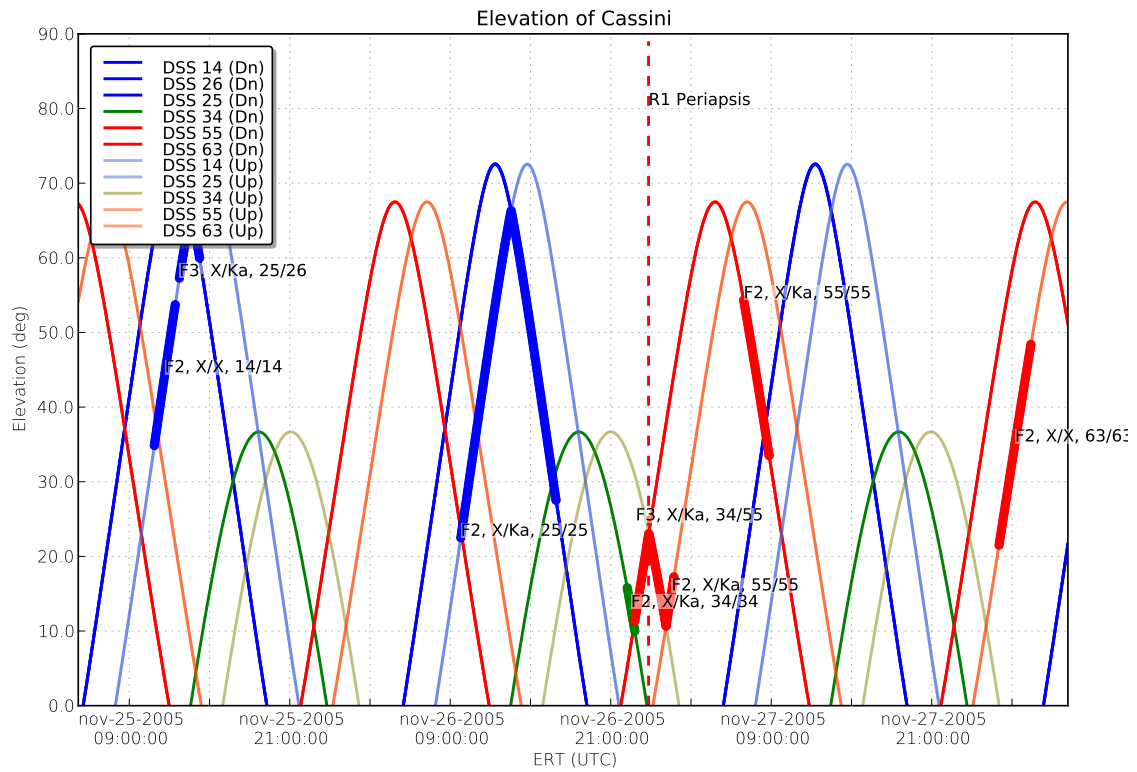
#### 4.4.2 Data Calibration

When available, Advanced Media Calibration system (AMC) data [10], obtained from advanced water vapor radiometers, were used to calibrate the wet path delay due to the Earth's troposphere. When not available, the Earth's troposphere was calibrated using the standard Tracking System Analytical Calibration (TSAC) data, based on a combination of weather data and dual frequency GPS measurements. The TSAC calibration provides good accuracy for the dry component but fails to calibrate the short time scale (60s-1000s) variations of the wet component [27]. However, the AMC calibrations are less reliable, because advanced water vapor radiometers provide not reliable measurements if liquid content is present along the line of sight. For this reason AMC calibrations were applied and generated through an iterative process: starting from a base analysis obtained using only TSAC calibrations, AMC calibrations are applied on a single tracking pass. Then, their effect is evaluated comparing the residuals and the solution obtained. If the residuals show a degradation, the corresponding AMC data are analyzed in detail, re-generated with different options and re-iterating the procedure, or totally discarded. The Earth's ionosphere was calibrated using data generated from dual frequency GPS measurements.

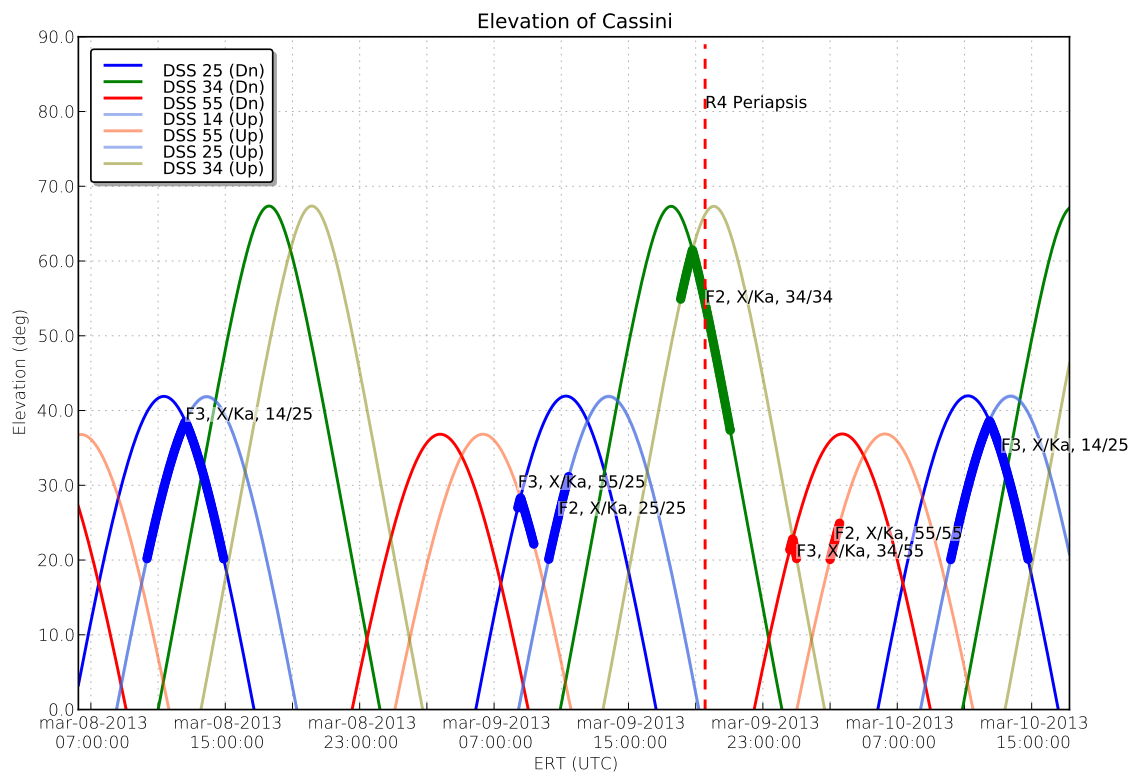
##### 4.4.2.1 Time synchronization of AMC data

During the analysis, an issue regarding the time synchronization of the AMC calibrations was found. In particular, a possible time delay was identified in the AMC data for the DSS-25 tracking station. As a part of the process of AMC application and evaluation, the cross-correlation between the AMC calibrations and the residuals, obtained without troposphere calibrations, was computed. Under normal circumstances, a strong correlation at a zero time-lag is expected, because one, if not the most, of the dominant noise sources in the residuals should be the delay due to the Earth's troposphere. This result was obtained for the AMC calibrations on the DSS-55, as shown in Figure 4.4.

However, for the two tracking passes on the DSS-25, the peak of the cross correlation was found at about  $-20$  s, as shown in Figure 4.5. The data were



(a) R1. The C/A is about at 26-NOV-2005, 23:50 UTC.



(b) R4. The C/A is about at 09-MAR-2013, 19:40 UTC.

Figure 4.3: Cassini elevation with respect to the uplink and downlink stations during R1 and R4, function of the receiving time of the signal. The bold lines represent the minimum elevation between uplink and downlink during the tracking passes used in the analysis.

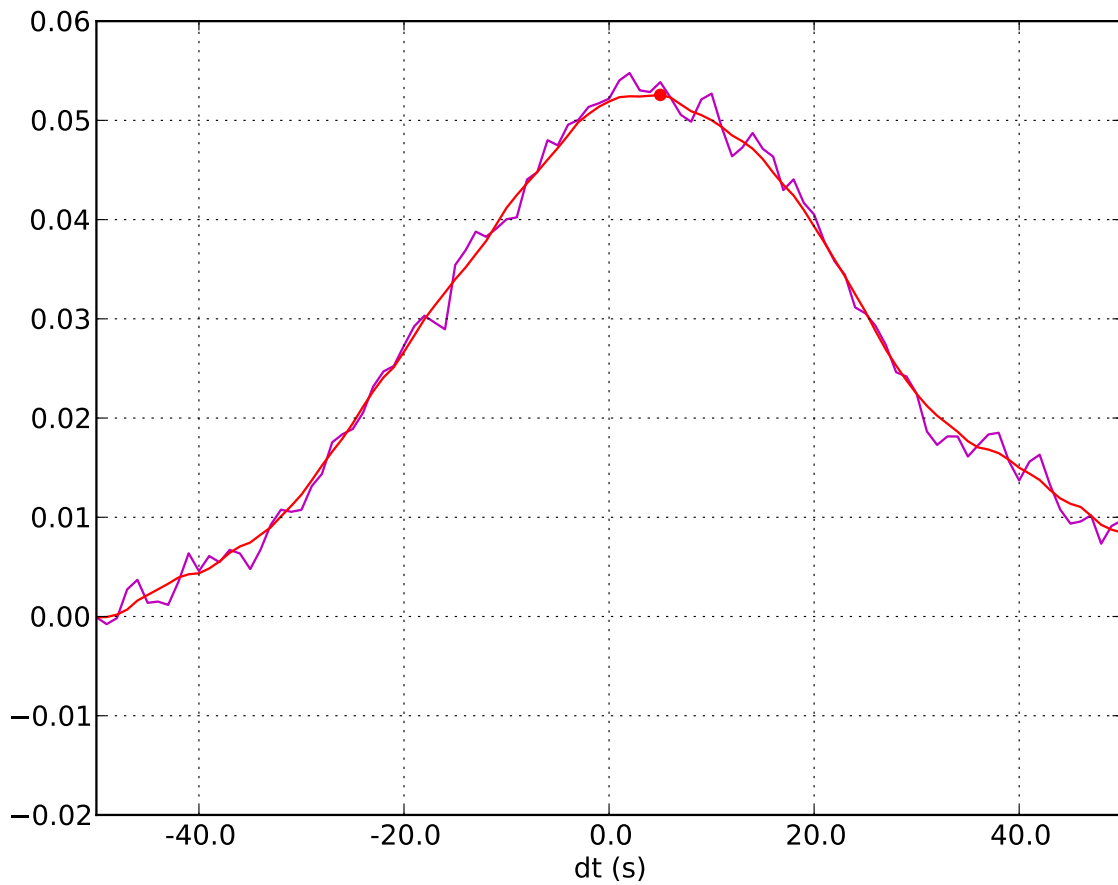


Figure 4.4: Cross correlation between the AMC calibration on DSS-55 and corresponding residuals obtained without tropospheric calibrations. To remove the spikes, the cross-correlation is also low-pass filtered using a simple central moving average on a time interval of 10 s. The peak of the cross correlation is about at zero time lag.

reprocessed inserting this time shift in the AMC calibrations for the DSS-25 only, obtaining a significant improvement: the RMS of the residuals of the corresponding passes reduced by 16%, from  $19 \mu\text{m/s}$  to  $16 \mu\text{m}$ . However, the improvement of the estimation of the gravity field was marginal, because the two passes does not cover the closest approach, where is concentrated the maximum observability.

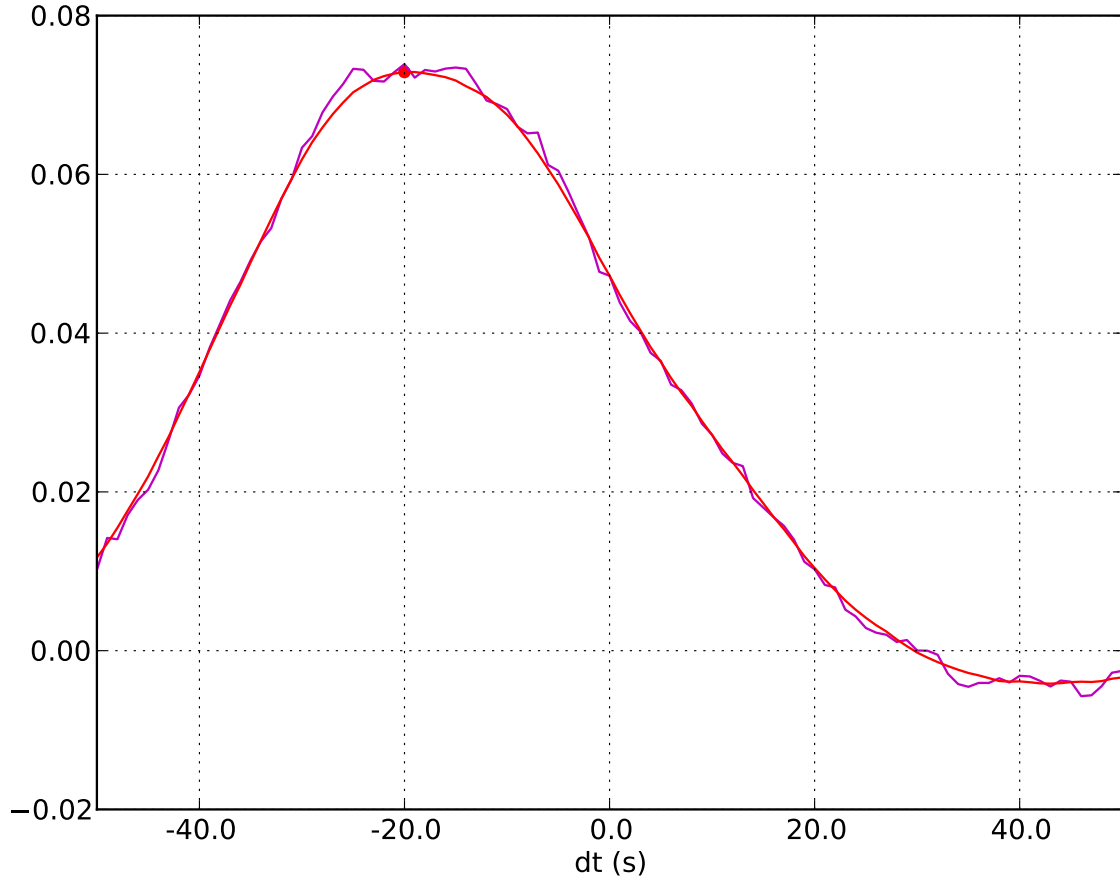


Figure 4.5: Cross correlation between the AMC calibration on DSS-25 and corresponding residuals obtained without tropospheric calibrations. To remove the spikes, the cross-correlation is also low-pass filtered using a simple central moving average on a time interval of 10 s. The peak of the cross correlation is about at a time lag of  $-20$  s.

## 4.5 Estimation

The calibrated data set was analyzed using MONTE. The orbit determination process is a filtering process: the solution is the value of the solve-for parameters that minimizes, in a least square sense, the residuals between the real measurements and the simulated measurements, computed using a mathematical model. Moreover, the corresponding formal covariance matrix, that defines the formal uncertainty of the solution, is computed. The residuals are weighted on a pass-by-pass basis using the RMS of the residuals itself. The RMS of the residuals is not known a priori, so the estimation is an iterative process: at the beginning the weights are chosen on

the basis of past analysis and mathematical models of the noise sources. After the convergence of the estimation, the postfit residuals are weighted using the RMS of the corresponding tracking pass and the estimation is repeated. The convergence is reached when the RMS of the postfit residuals, grouped into the tracking passes, are equal, or a bit less, than the corresponding weights used for the analysis. This weighting strategy is based on the implicit assumption that the postfit residuals, at least on a single pass, represent only a white noise. This assumption is not always verified, but can be considered true in the frequency bands of interest.

To increase the convergence the minimizing function comprises also the distance from an a priori estimate of the state vector, used also at the first iteration to fit the data. This distance is weighted using the a priori covariance matrix, which represents the covariance matrix of the a priori estimate.

In the various analysis the following parameters were estimated:

- Initial state of Cassini. In the joint multi-arc analysis a different initial state was estimated for each arc.
- Initial state of Rhea at the epoch of the first fly-by. In this work the classical “global” approach, described in Chapter 4.3, was chosen.
- The gravitational parameters  $GM$  of Rhea.
- The quadrupole gravity field of Rhea. Different solutions were obtained estimating different sets of the quadrupole coefficients.

**Cassini Initial State** The a priori values for the Cassini states were obtained from the reconstructed trajectory provided by the Cassini Navigation Team<sup>2</sup>. The a priori uncertainty was set conservatively using a diagonal covariance matrix with 1-sigma of 5 km for the X and Y position components, 15 km for the Z position component, 10 mm/s for the X and Y velocity components and 30 mm/s for the Z velocity component. These values are 5-50 times larger than the typical covariance matrices provided by the Cassini navigation team. Moreover, using a diagonal a priori covariance matrix is a conservative assumption, because it neglects all the information, in terms of correlations, derived from the past analysis.

**Rhea Initial State** The a priori values for the Rhea state were retrieved from the Saturn’s satellite ephemerides SAT355<sup>3</sup>. The a priori uncertainty was set conservatively using a diagonal covariance matrix with 1-sigma of 6 km for each component of the position and 60 mm/s for each velocity component. These values are 30-50 times larger than the typical covariance matrices provided by the Cassini navigation team. Moreover, as for the Cassini initial state, using a diagonal a priori covariance matrix is a conservative assumption, because it neglects all the information derived from past data.

---

<sup>2</sup>The updated Cassini trajectory Spice kernels are available at <ftp://naif.jpl.nasa.gov/>.

<sup>3</sup>Available at <ftp://ssd.jpl.nasa.gov/pub/eph/satellites/>.

**Rhea Gravity Field** The a priori values of  $GM$ ,  $J_2$ ,  $C_{22}$  and  $S_{22}$  were retrieved from [40]. The a priori value of  $C_{21}$  and  $S_{21}$  was set to zero. Given the limited amount of data, analyzing a single fly-by with tracking at the closest approach is not possible to obtain a reasonable estimation of the full quadrupole gravity. Hence, in the single-arc analysis  $C_{21}$  and  $S_{21}$  were set to zero. Single-arc analyses were obtained estimating also  $C_{21}$  and  $S_{21}$  but the formal uncertainties of the gravity coefficients increased by more than 2 orders of magnitude. For the same reason, higher degree harmonics, whose estimation is not possible with only two fly-bys, were set to zero in all the analyses. To not constrain the estimation, the a priori uncertainties of the  $GM$  and the estimated quadrupole coefficients were set to be much higher, at least one order of magnitude, than the formal uncertainty.

To assess the stability of the estimated gravity field, different solutions were produced, changing: the sets of estimated parameters, the a priori values, the a priori uncertainties, the data set, the satellite ephemerides, the calibrations. No significant differences were found, hence in this work only the most relevant solutions are reported:

**Sol-R1** : Single-arc solution of R1 fly-by, estimating the  $GM$  and  $J_2$ ,  $C_{22}$  and  $S_{22}$  only.  $C_{21}$  and  $S_{21}$  were set to zero.

**Sol-R4** : Single-arc solution of R4 fly-by, estimating the  $GM$  and  $J_2$ ,  $C_{22}$  and  $S_{22}$  only.  $C_{21}$  and  $S_{21}$  were set to zero.

**Sol-MA-0** : Multi-arc solution of both R1 and R4 fly-bys, estimating the  $GM$  and  $J_2$ ,  $C_{22}$  and  $S_{22}$  only.  $C_{21}$  and  $S_{21}$  were set to zero as in Sol-R1 and Sol-R4 for a direct comparison.

**Sol-MA** : Multi-arc solution of both R1 and R4 fly-bys, estimating the  $GM$  and the full quadrupole gravity field with very large a priori uncertainties.

**Sol-MA-L** : Multi-arc solution of both R1 and R4 fly-bys, estimating the  $GM$  and the full quadrupole gravity field with very large a priori uncertainties. Rhea initial state is treated as a local parameter, using the “local approach”.

**Sol-MA-HE** : Multi-arc solution of both R1 and R4, estimating  $GM$  and the full quadrupole, where the ratio between  $J_2/C_{22}$  was imposed to the hydrostatic equilibrium value of 10/3.

The results of the analyses are summarized in Chapter 4.6.

## 4.6 Results

In this section the results of the different analyses are collected.

### 4.6.1 Residuals

Figure 4.6 to Figure 4.10 report the post-fit residuals of the tracking passes around the closest approaches of R1 and R4 for all the solutions described above. For all the solutions (apart Sol-MA-HE) the residuals do not show any evident

signature around the closest approach and the RMS of the residuals are very similar, about  $77 \mu\text{m/s}$  for R1 and about  $17 \mu\text{m/s}$  for R4. The only exception is Sol-MA-HE: the residuals of R1 show an evident signature around the closest approach, while for R4 the signature is not evident. For R1 the RMS of the residuals is about  $90 \mu\text{m/s}$ , larger than the other solutions by 17%, while for R4 the RMS is about  $17.8 \mu\text{m/s}$ , an increases only by 4%.

## 4.6.2 Rhea Gravity Field

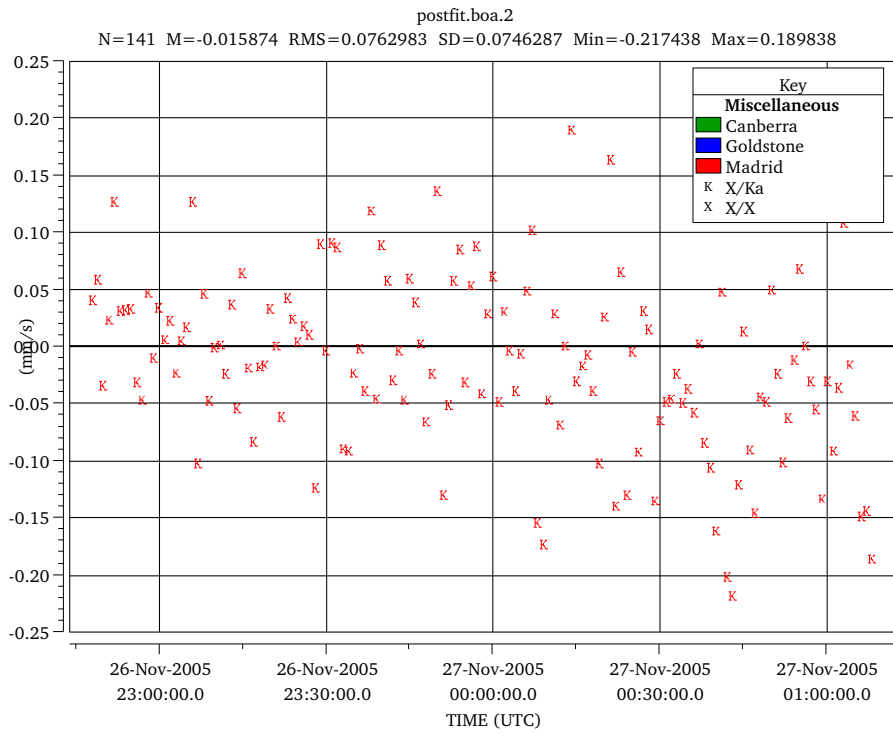
Figure 4.11 shows the different estimations of Rhea's  $GM$ , along with their 1-sigma errorbars, while Figure 4.12 shows  $J_2$  and  $C_{22}$  in the  $J_2$ - $C_{22}$  plane, along with their 1-sigma error ellipses. Where applicable, the estimations are compared to the value published in the literature. For sake of clarity, only the results published in [4] and [40] were considered. Finally, as reference, Table 4.4 collects all the estimated gravity coefficients for all the different solutions described in this work.

## 4.6.3 Comments

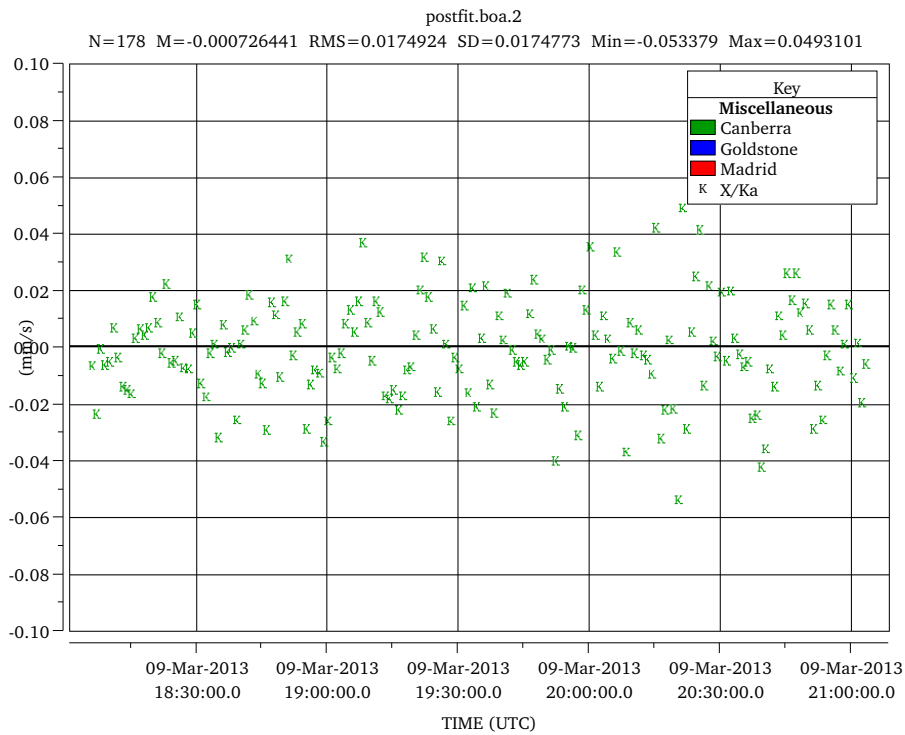
### 4.6.3.1 MONTE Set-Up Validation

In this work all the analyses were produced using MONTE, the new orbit determination software developed in the latest years by JPL. Before this work, MONTE was never used to analyze radio science gravity experiments. A first validation of the set-up can be made comparing the results of these analyses with each others and with the values available in literature. The following considerations can be made:

- Sol-R1 is compatible at 1-sigma level with [40]. The formal uncertainties are larger because quite conservative a priori diagonal covariance matrices for the Cassini and Rhea states were chosen, while [40] used the full covariance matrices provided by the Cassini navigation team. As expected from an almost equatorial fly-by,  $C_{22}$  is estimated with better accuracy than  $J_2$ .
- Sol-R1 is not compatible at 3-sigma level with [4]. However the solutions cannot be directly compared, because [4] constrained a priori the hydrostatic equilibrium.
- Sol-R4 and Sol-R1 are compatible at 1-sigma level (2-sigma for  $S_{22}$ ). However, Sol-R4 has significantly larger uncertainties than Sol-R1, even though the RMS of the residuals at the closest approach is more than 4 times smaller. The reasons is a smaller sensitivity to  $J_2$  and  $C_{22}$  because of the less favorable orbital geometry: the R4 fly-by is characterized by a larger distance and a larger relative velocity at the closest approach than R1. Moreover the inclination introduces a strong correlation between  $J_2$  and  $C_{22}$  that increases the uncertainties.
- All the multi-arc solutions are compatible at 1-sigma level with each others and with the single-arc solutions. The only exception is Sol-MA-HE, that cannot be directly compared with the other solutions because it was obtained

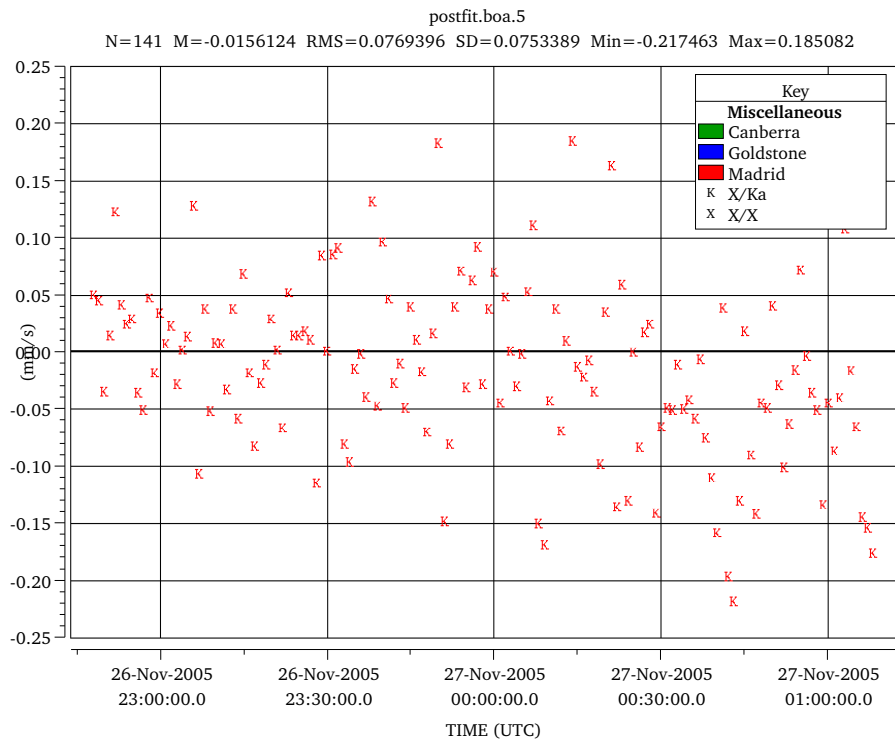


(a) R1. The C/A is about at 26-NOV-2005, 23:50 UTC.

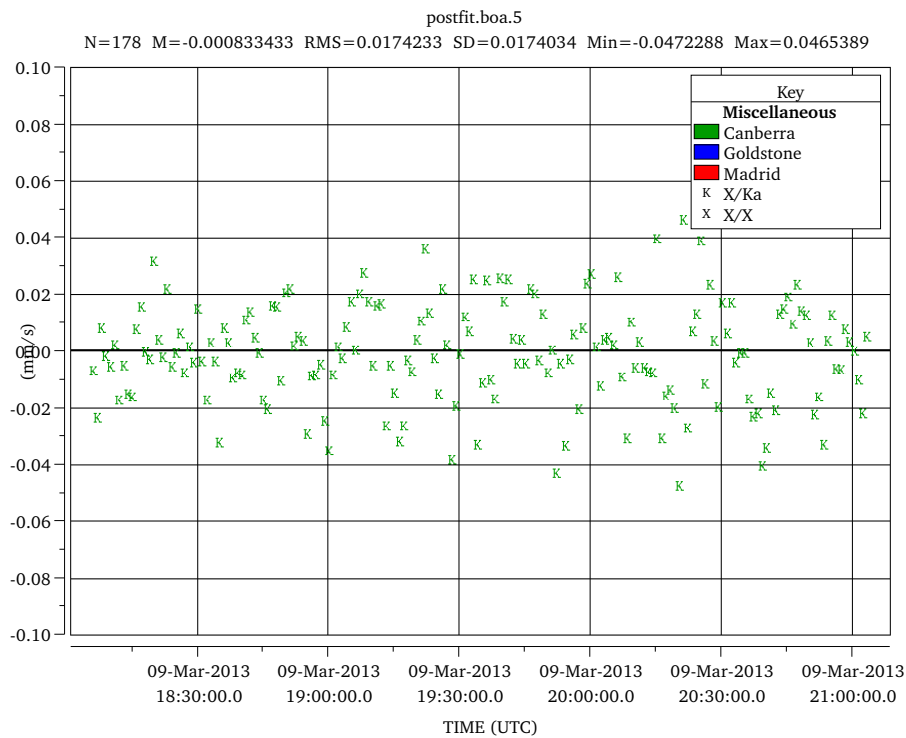


(b) R4. The C/A is about at 09-MAR-2013, 19:40 UTC.

Figure 4.6: Sol-R1 and Sol-R4: range-rate residuals around the closest approach of R1 and R4 in mm/s.

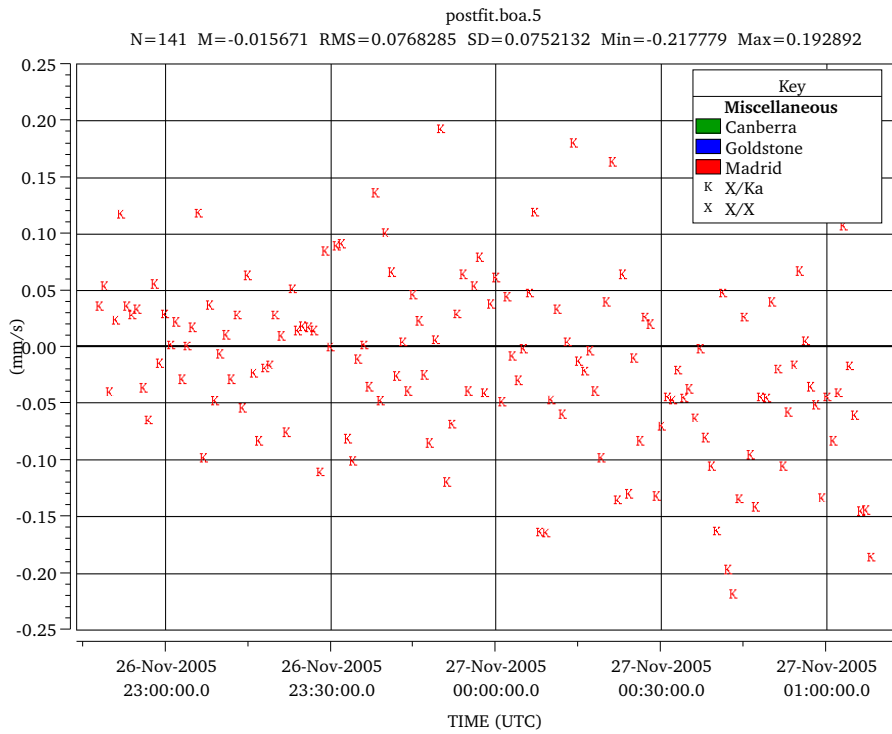


(a) R1. The C/A is about at 26-NOV-2005, 23:50 UTC.

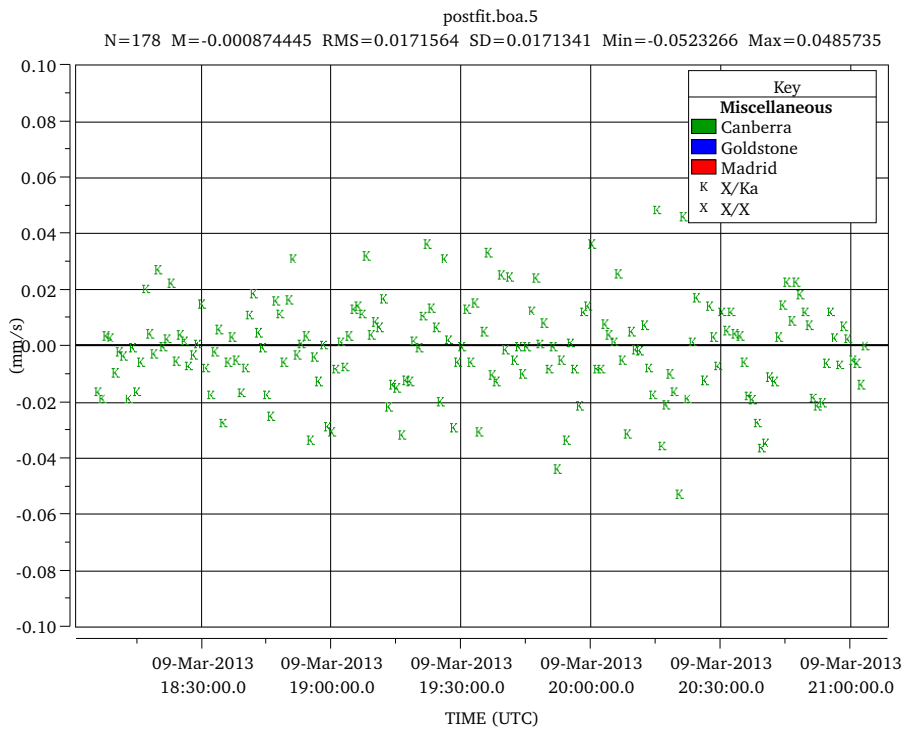


(b) R4. The C/A is about at 09-MAR-2013, 19:40 UTC.

Figure 4.7: Sol-MA-0: range-rate residuals around the closest approach of R1 and R4 in mm/s.

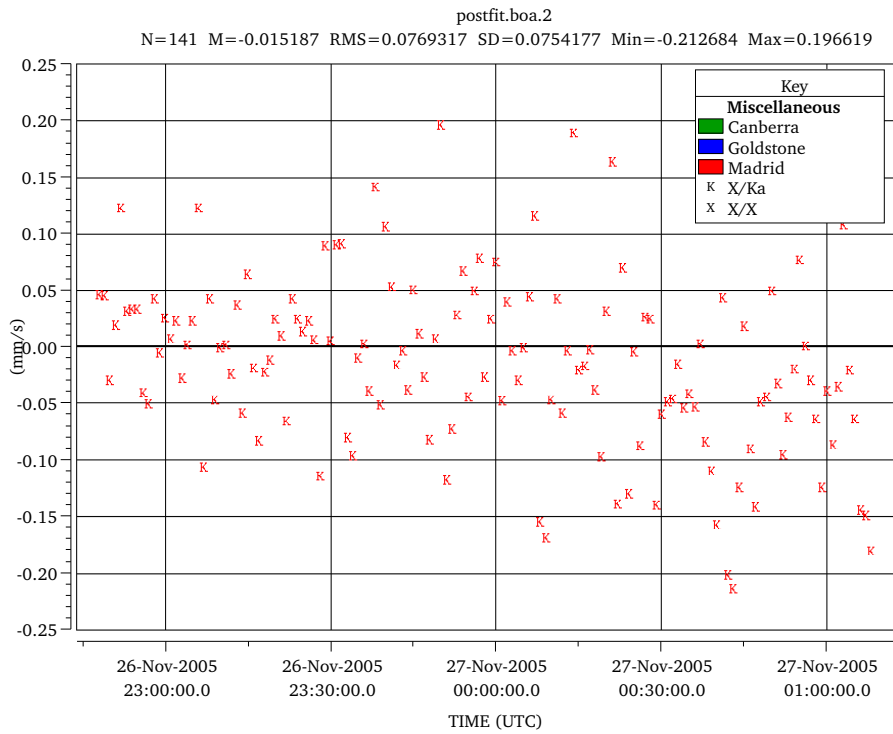


(a) R1. The C/A is about at 26-NOV-2005, 23:50 UTC.

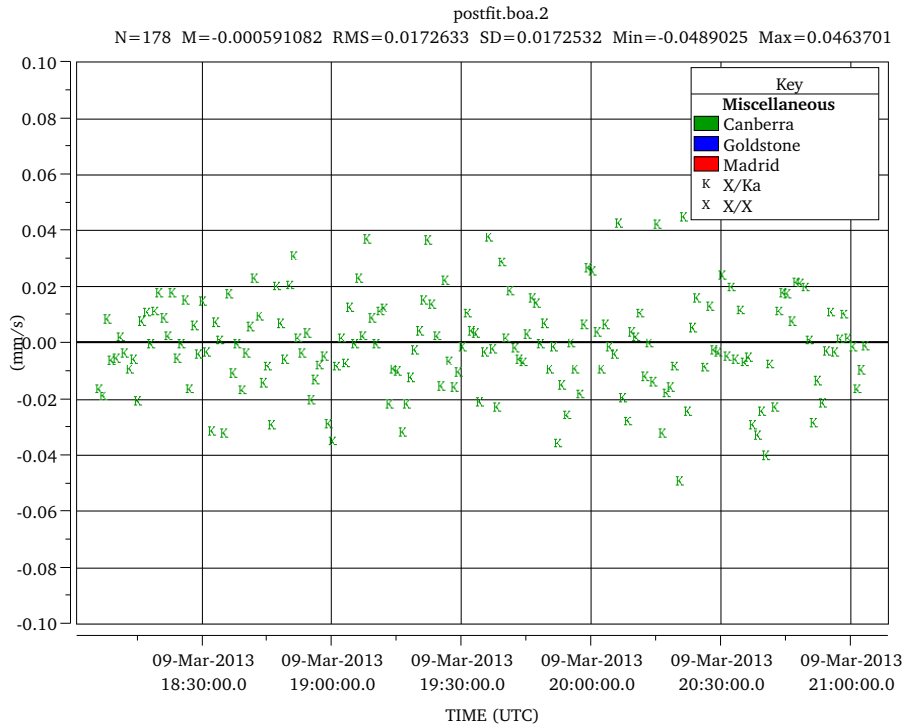


(b) R4. The C/A is about at 09-MAR-2013, 19:40 UTC.

Figure 4.8: Sol-MA: range-rate residuals around the closest approach of R1 and R4 in mm/s.

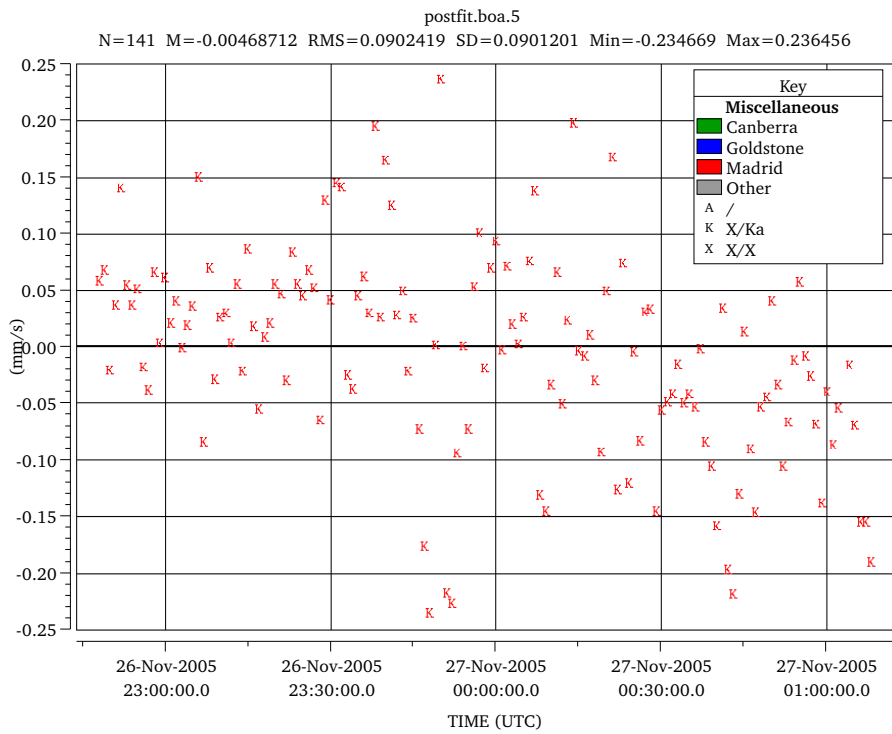


(a) R1. The C/A is about at 26-NOV-2005, 23:50 UTC.

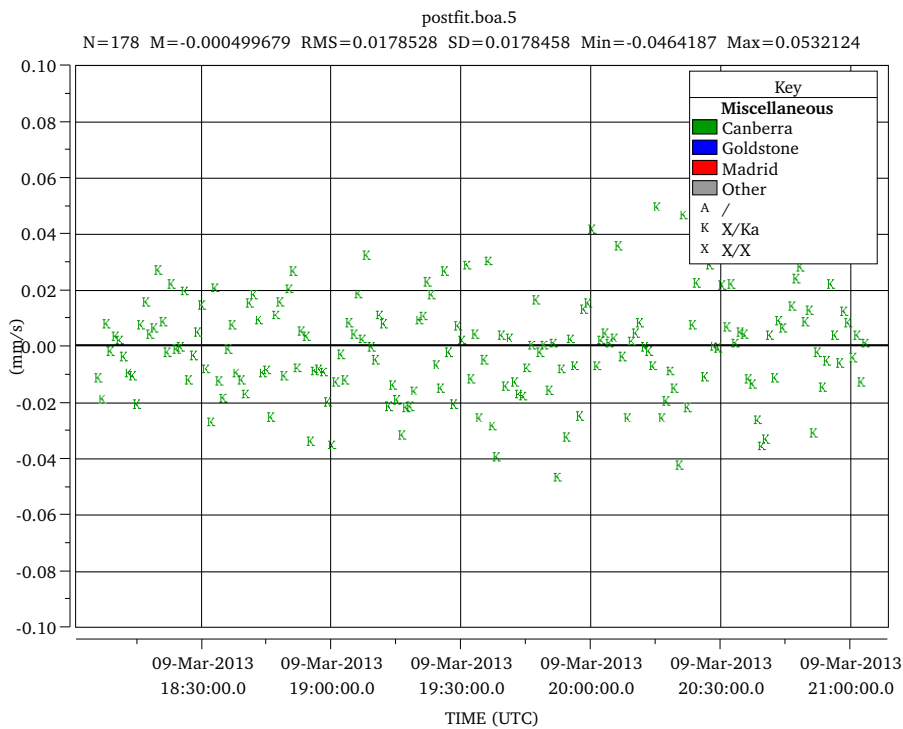


(b) R4. The C/A is about at 09-MAR-2013, 19:40 UTC.

Figure 4.9: Sol-MA-L: range-rate residuals around the closest approach of R1 and R4 in mm/s.



(a) R1. The C/A is about at 26-NOV-2005, 23:50 UTC.



(b) R4. The C/A is about at 09-MAR-2013, 19:40 UTC.

Figure 4.10: Sol-MA-HE: range-rate residuals around the closest approach of R1 and R4 in mm/s.

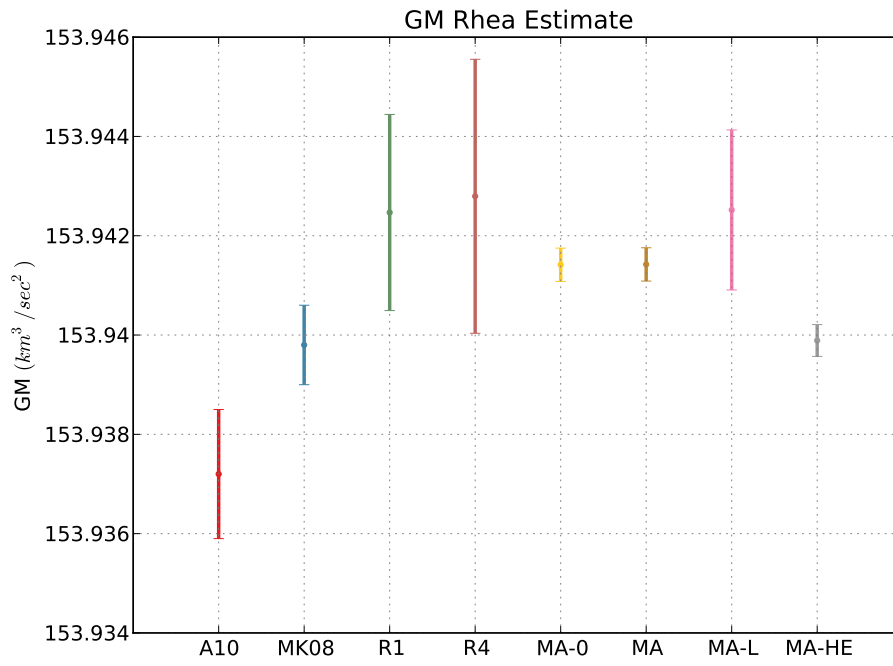


Figure 4.11: Rhea  $GM$  1-sigma error bars.

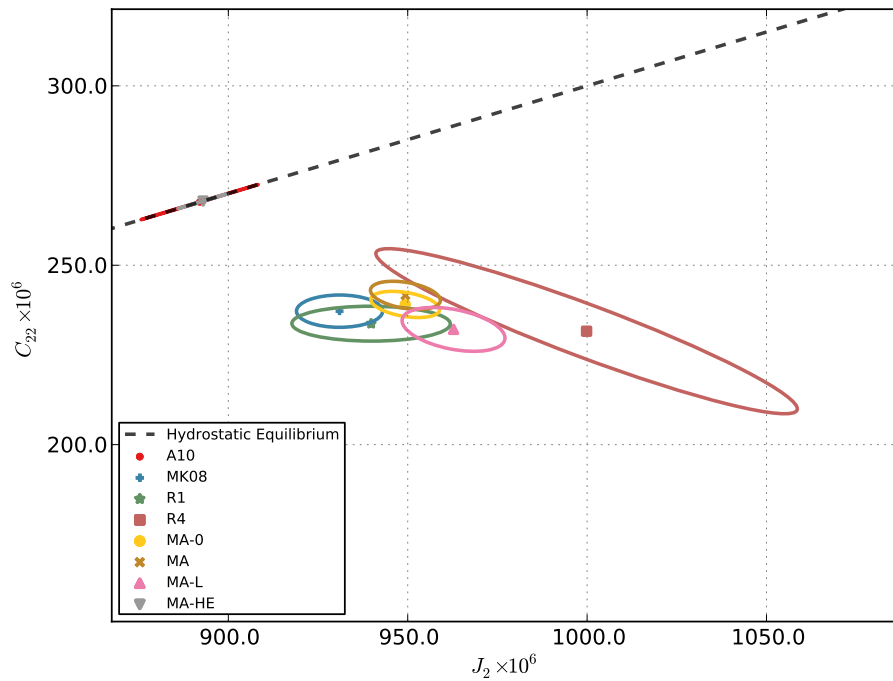


Figure 4.12: Rhea  $J_2$ - $C_{22}$  1-sigma error ellipses.

Table 4.4: Rhea estimated gravity fields.

	Apriori	Sol-R1	Sol-R4	Sol-MA-0
$GM$ ( $km^3/s^2$ )	153.940±0.025	153.9425±0.0020	153.9428±0.0028	153.94142±0.00034
$J_2$ ( $\times 10^6$ )	930±600	940±22	1000±59	949.3±9.6
$C_{21}$ ( $\times 10^6$ )	0±300	0.0±0.0	0.0±0.0	0.0±0.0
$S_{21}$ ( $\times 10^6$ )	0±300	0.0±0.0	0.0±0.0	0.0±0.0
$C_{22}$ ( $\times 10^6$ )	240±250	233.7±4.9	232±23	239.1±3.7
$S_{22}$ ( $\times 10^6$ )	0±250	-17.9±4.6	-50±16	-20.4±4.3
$J_2/C_{22}$	3.9±4.8	4.02±0.13	4.32±0.67	3.971±0.084
corr $J_2-C_{22}$	+0.00	-0.01	-0.94	-0.38
	Apriori	Sol-MA	Sol-MA-L	Sol-MA-HE
$GM$ ( $km^3/s^2$ )	153.940±0.025	153.94142±0.00034	153.9425±0.0016	153.93989±0.00032
$J_2$ ( $\times 10^6$ )	930±600	949.4±9.7	963±14	893.0±7.0
$C_{21}$ ( $\times 10^6$ )	0±300	-20±11	-16±11	-34±11
$S_{21}$ ( $\times 10^6$ )	0±300	25±20	-19±32	45±21
$C_{22}$ ( $\times 10^6$ )	240±250	241.6±3.9	232.1±6.1	267.9±2.1
$S_{22}$ ( $\times 10^6$ )	0±250	-15.5±5.0	-16.6±5.0	-16.2±6.0
$J_2/C_{22}$	3.9±4.8	3.929±0.087	4.15±0.15	3.3±0.0
corr $J_2-C_{22}$	+0.00	-0.36	-0.40	+1.00

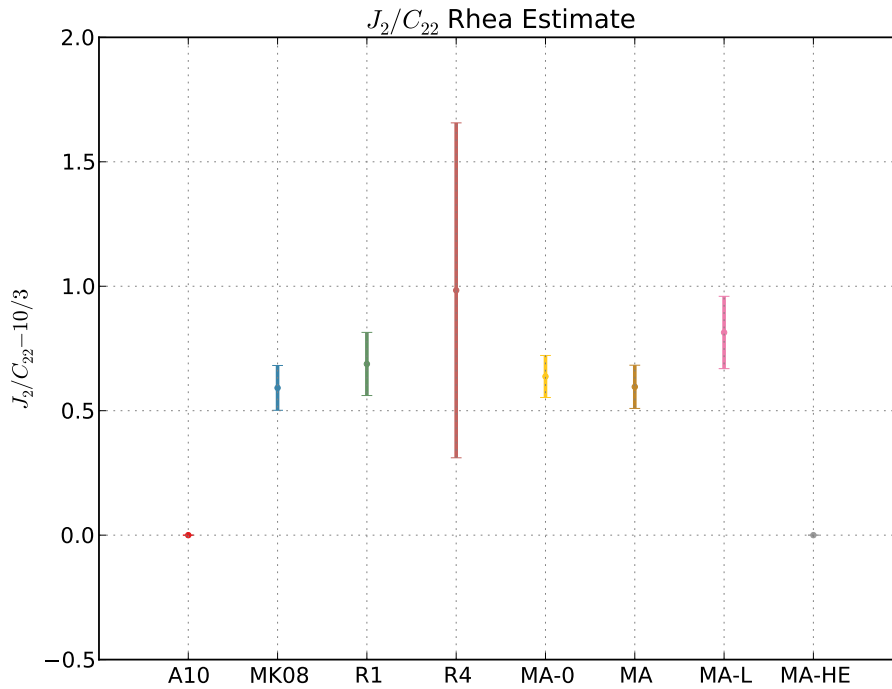


Figure 4.13: Rhea  $J_2/C_{22} - 10/3$  1-sigma error bars.

constraining the hydrostatic equilibrium ratio between  $J_2$  and  $C_{22}$ . However, Sol-MA-HE is compatible at 1-sigma level with [4], that used the same a priori constraint.

Summarizing, the MONTE set-up and procedures developed to analyze the radio science gravity experiments can be considered successfully tested, because all the solutions obtained are reliable and congruent to the set-up used.

#### 4.6.3.2 The Multi-Arc Strategy

The multi-arc strategy is a procedure to analyze radiometric data obtained during non-contiguous orbital arcs, allowing to increase the accuracy of the estimation with respect to the correspondent single-arc analyses. Regarding the analysis of the Rhea radio science gravity experiments, the two fly-bys R1 and R4 were first analyzed using a single-arc approach, then they were jointly analyzed using the multi-arc approach obtaining significant improvements in the Rhea's gravity field estimation, as expected. To quantify this improvements, Sol-MA-0 can be directly compared to Sol-R1 and Sol-R4 because it was obtained using the same a priori and estimating the same gravity coefficients. At a first approximation, adding more arcs is like adding more measurement of the same physical quantity, so the uncertainty is expected to decrease with the square-root of the number of arcs  $\sqrt{N}$ , which corresponds to a 30% passing from 1 arc to 2 arcs. Moreover, of the two single-arc solutions, Sol-R4 is characterized by much larger uncertainties, by about 5 times for  $C_{22}$  and 3 times for  $J_2$ . Hence, at a first approximation, the uncertainty is expected to decrease by less than the 30% because R4 seems to carry less information content than R1. In fact, the addition of R4 data allowed to improve the estimation of  $C_{22}$  by 20%, but the estimation of  $J_2$  improved by 55%. This is because the advantage

of a multi-arc approach is not simply the addition of more equivalent measurements, but it allows to break the correlations between the parameters. In this case, R1 is an almost equatorial fly-by, so there is a large correlation between  $J_2$  and  $GM$  because the acceleration due to  $J_2$  can be separated from the  $GM$  contribution only for the different variation with the distance from the body. R4 is an almost polar fly-by, then it allows to break this correlation.

Moreover, given the limited amount of data, the single-arc analyses did not allow to obtain a reasonable estimation of the full quadrupole gravity, so  $C_{21}$  and  $S_{21}$  were set to zero. On the contrary, the multi-arc analyses allowed to estimate also  $C_{21}$  and  $S_{21}$ , obtaining almost equal central values and a very limited increase of the formal uncertainties, about the 7% for  $C_{22}$  and less than 2% for  $J_2$ .

### 4.6.3.3 The Satellite Ephemerides Update Strategy

As stated in Chapter 4.3, during a multi-arc analyses two approaches for the update of the satellite ephemerides can be used: the “global”, conventional, method and the new “local” method. Sol-MA-0, Sol-MA and Sol-MA-HE were obtained using the global approach, while Sol-MA-L was obtained using the local approach starting from the same set-up of Sol-MA.

As a result, solution Sol-MA is compatible at a 1-sigma level with Sol-MA, but it is characterized by larger uncertainties: the standard deviation of  $J_2$  and  $C_{22}$  increase by 50%, while for  $GM$  it increases by a factor of 5. This is because the local approach has a large number of parameters to estimate, and using the global approach the orbit of Rhea during R4 is very sensitive to the satellite’s  $GM$  because of the very long propagation from the initial epoch.

Summarizing, the local approach provides compatible results for the gravity field, but the global approach provides the best accuracies. However, the local approach can be very useful during the analysis set-up, for example to build and validate the dynamical model and to evaluate the calibrations, because of the much smaller integration times.

## 4.7 Interpretation

The most important consideration that is possible to do from the results reported in Chapter 4.6 is that the obtained estimation of the Rhea quadrupole field are not compatible with the condition of hydrostatic equilibrium. In fact, as shown in Figure 4.12 and Figure 4.13, the ratio  $J_2/C_{22}$  is more than 3-sigma apart from the hydrostatic value of  $10/3$  for all the solution apart Sol-R4, that is about 1.5-sigma apart, and Sol-HE, where the hydrostatic equilibrium was constrained a priori. Moreover, forcing the hydrostatic equilibrium degrades the orbital fit, as can be observed comparing the solutions Sol-MA and Sol-MA-HE, that differ only for the hydrostatic equilibrium constraint. For R1, the residuals of Sol-MA-HE show an evident signature around the closest approach, and the RMS increases by 17%, from about  $77 \mu\text{m/s}$  to about  $90 \mu\text{m/s}$ . However, for R4 the degradation is much smaller: the residuals of Sol-MA-HE do not show any evident signature, and the RMS increases only by a 4%, to about  $17.8 \mu\text{m/s}$ .

Given a body in hydrostatic equilibrium, deviations from the spherical symmetry are caused only by its rotation and tidal forces exerted by an external body and are dominated by the quadrupole terms. In particular, considering a satellite in hydrostatic equilibrium and in a circular orbit around a planet, if the satellite is in synchronous rotation the only non-zero quadrupole terms are  $J_2$ , generated by both rotation and tides, and  $C_{22}$ , generated by only tidal forces. Their ratio, as said before, is defined as  $10/3$ . In this case the Radau-Darwin equation can be used to infer the normalized principal moment of inertia  $C/MR^2$  [20, 55]:

$$\frac{C}{MR^2} = \frac{2}{3} \left[ 1 - \frac{2}{5} \sqrt{\frac{4 - k_f}{1 + k_f}} \right] \quad (4.8)$$

where the fluid Love's number  $k_f$  can be obtained by either  $J_2$  or  $C_{22}$  according to the following relations:

$$k_f(J_2) = \frac{6 J_2}{5 q_r} = -\frac{18 J_2}{5 q_t} \quad (4.9)$$

$$k_f(C_{22}) = 4 \frac{C_{22}}{q_r} = -12 \frac{C_{22}}{q_t} \quad (4.10)$$

where  $q_r$  and  $q_t$  are adimensional parameters related respectively to the body's rotation and external tides:

$$k_f(J_2) = \frac{6 J_2}{5 q_r} = -\frac{18 J_2}{5 q_t} \quad (4.11)$$

$$k_f(C_{22}) = 4 \frac{C_{22}}{q_r} = -12 \frac{C_{22}}{q_t} \quad (4.12)$$

The moment of inertia can provide useful information about the degree of differentiation of the body: for an homogeneous body  $C/MR^2 = 0.4$ , hence smaller values indicates that there is a concentration of mass near the center, as a rocky core. Moreover, it can be used as an additional constraint for parametric models of the internal structure of the body.

Even if Rhea does not satisfy the assumption of hydrostatic equilibrium, the Radau-Darwin equation can give useful indications about its degree of differentiation, recalling that in this case it may led to significant errors, up to 20% [25]. For each solution, the fluid Love's number  $k_f$ , and so  $C/MR^2$ , can be computed either by  $J_2$  or  $C_{22}$ . From Table 4.5 is it possible to state that all the solutions produce qualitatively similar results, even if with different values and accuracies. Using  $J_2$  higher values of  $C/MR^2$  are obtained, very similar to the homogeneous value of 0.4, while using  $C_{22}$  smaller values are obtained, about 0.37.  $J_2$  provides smaller formal uncertainties, but the real uncertainty is dominated by the applicability of the Radau-Darwin equation itself. This is a strong indication that Rhea may be almost homogeneous, or at least with a small degree of differentiation. However, the exact degree of differentiation and the internal composition cannot be assessed with the available data but an important constraint has been derived anyway.

Table 4.5: Rhea Fluid Love's Number and  $C/MR^2$ .

	$k_f(J_2)$	$k_f(C_{22})$	$C/MR^2(J_2)$	$C/MR^2(C_{22})$
Sol-R1	$1.502 \pm 0.035$	$1.245 \pm 0.026$	$0.4002 \pm 0.0038$	$0.3713 \pm 0.0031$
Sol-R4	$1.598 \pm 0.094$	$1.23 \pm 0.12$	$0.4103 \pm 0.0096$	$0.370 \pm 0.015$
Sol-MA-0	$1.518 \pm 0.015$	$1.274 \pm 0.019$	$0.4019 \pm 0.0016$	$0.3747 \pm 0.0023$
Sol-MA	$1.518 \pm 0.016$	$1.287 \pm 0.021$	$0.4019 \pm 0.0017$	$0.3763 \pm 0.0024$
Sol-MA-L	$1.539 \pm 0.023$	$1.237 \pm 0.033$	$0.4041 \pm 0.0024$	$0.3703 \pm 0.0039$
Sol-MA-HE	$1.427 \pm 0.011$	$1.427 \pm 0.011$	$0.3921 \pm 0.0012$	$0.3921 \pm 0.0012$

# Chapter 5

## Conclusions

The work presented in this thesis had as its subject the study and development of new models and toolkits for orbit determination codes to support the radio science gravity experiments of the Cassini-Huygens mission to Saturn.

Cassini is the largest interplanetary spacecraft ever built. It carries the most sophisticated and high-performance communication and radio science systems which, used in conjunction with the most advanced ground station equipment, allowed to obtain an unprecedented accuracy in the spacecraft orbit determination and radio science experiments. At present, even if the failure of the KaT transponder affected the capabilities of the spacecraft to calibrate the solar plasma, the quality of the residuals is still extremely high, allowing to perform many interesting investigations and supporting important discoveries about the Saturn system. Future interplanetary missions, like NASA's Juno and ESA's BepiColombo and JUICE, are expected to achieve and maybe surpass the extraordinary performances of Cassini radio science.

To support these highly accurate radio science experiments, improvements also in the data analysis procedures must be achieved.

A first part of the work focused on a detailed study of a somewhat unexpected source of noise: the numerical errors in the Doppler observables computed by the orbit determination codes. The numerical errors are due to the use of finite arithmetics in the computers and, as the "real" measurements noise, they degrade the accuracy of the orbit determination. Even if the numerical noise was known since the very beginning of the space era, a detailed characterization was never performed and its entity was never considered in the noise budget of the orbit determination, both for navigation and radio science. This work should have fill this gap proving that, surprisingly, the numerical errors can be an important source of noise, comparable to the measurements noise and, in some conditions, even larger. In the process of characterize the numerical errors, several models with different levels of accuracy were built: initially, an order of magnitude model allowed to assess the possible criticality of the problem, so the development of more sophisticated models was started. This required a parallel effort on two aspects: on one side a detailed study of the mathematical formulation of the radiometric observables was performed, focusing on its actual implementation in the main orbit determination codes. Particular attention was devoted to the solution of the light-time problem, one of the most delicate phases of the computation. On the other side a more

realistic modelization of the rounding errors, the so-called Widrow's model, was identified and applied to the problem under consideration. A first detailed model provided promising accuracies in the a priori estimation of the numerical noise, but it failed to provide a complete and satisfactory description of all the observed phenomena. More analyses were performed to assess the applicability of the Widrow's model, finding some condition under which the model cannot be applied, and deriving the necessary corrections. The resulting, complete, detailed model describes with very good accuracy the numerical noise on radiometric observables computed by both the ODP, the orbit determination program developed since 1960s by NASA/JPL, and its recent successor MONTE. In particular, the model allows to estimate a priori the numerical noise standard deviation for a specific orbit determination problem, with typical accuracies below the 10%. A numerical noise characterization proved that the ODP numerical noise is already at critical levels: for the Cassini and Juno mission it can reach values of about  $60 \mu\text{m/s}$  at 60s of integration time, and it may dominate the noise budget of the missions. To mitigate these problems, MONTE implements an extended precision representation of time variables, allowing a reduction of the numerical noise of about one order of magnitude. The MONTE numerical noise however, even if mitigated, remain an important source of noise for the high-precision radio science experiments of present and future missions, like Juno and JUICE.

A second part of the work focused on extending Monte functionalities to support radio science investigations. In particular, the multi-arc approach allows to improve the estimation of constant parameters through the joint analysis of measurements acquired during non-contiguous orbital arcs. This approach is fundamental to analyze the Cassini radio science experiments dedicated to the estimation of gravity fields of Saturn and its satellites. However, at present, Monte supports only a single-arc approach, so a Monte-Python library to perform a multi-arc analysis was developed. The resulting `multiarc` library allows to easily set-up, configure, and execute a multi-arc analysis. It is well integrated with Monte, because it does not introduce external software to assembly and filter the residuals, so that only Monte routines, developed and tested by JPL, are used for the most delicate phases of the orbit determination process, which are: spacecraft trajectory integration, residuals and the partials computation, and estimation. The library was developed and successfully tested during the analysis of the Cassini radio science gravity experiments of the Saturn's satellite Rhea.

Rhea is the second biggest satellite of Saturn. Cassini performed two fly-bys of Rhea dedicated to gravity investigations, the first in November 2005, referred to as R1, and the second in March 2013, referred to as R4. The radiometric data acquired during R1 were analyzed by the scientific community with two different approaches, obtaining non-compatible estimations of the Rhea's gravity field. In particular, a first approach assumed *a priori* the hydrostatic equilibrium, obtaining several constraints about the satellite's internal structure and composition. A second approach computed an unconstrained estimation of the quadrupole gravity field coefficients  $J_2$ ,  $C_{22}$  and  $S_{22}$ , obtaining a solution non statistically compatible with the condition of hydrostatic equilibrium. In this case, no useful constraint on Rhea's interior structure could be imposed. This thesis presented the estimation of the Rhea's gravity field obtained from a joint multi-arc analysis of R1 and R4,

describing in details the spacecraft dynamical model used, the data selection and calibration procedure, and the analysis method followed. In particular, the approach of estimating the full unconstrained quadrupole gravity field was followed, obtaining a solution statistically not compatible with the condition of hydrostatic equilibrium. The stability of the solution was tested performing different multi-arc analysis varying the data set, the strategy for the update of the satellite ephemerides and the dynamical model. The solution proved to be stable and reliable. Given Rhea's non-hydrostatic condition, very few considerations about its internal structure can be made. In particular, the computation of the moment of inertia factor using the Radau-Darwin equation can introduce large errors. Nonetheless, even by accounting for this possible error, the normalized moment of inertia is in the range 0.37-0.4 indicating that Rhea's may be almost homogeneous, or at least characterized by a small degree of differentiation. The internal composition cannot be assessed with more details with the available data but, unfortunately, no other gravity flybys are scheduled up to the end of the mission in 2017.



# Bibliography

- [1] Acton, C. H., “Ancillary data services of NASA’s Navigation and Ancillary Information Facility,” *Planetary and Space Science*, vol. 44, 1996, pp. 65–70.
- [2] Anderson, J. D., Rappaport, N. J., Giampieri, G., Schubert, G., and Moore, W. B., “Gravity field and interior structure of Rhea,” *Physics of the Earth and Planetary Interiors*, vol. 136, Apr. 2003, pp. 201–213.
- [3] Anderson, J. D., and Schubert, G., “Saturn’s satellite Rhea is a homogeneous mix of rock and ice,” *Geophysical Research Letters*, vol. 34, Jan. 2007, pp. 4–7.
- [4] Anderson, J. D., and Schubert, G., “Rhea’s gravitational field and interior structure inferred from archival data files of the 2005 Cassini flyby,” *Physics of the Earth and Planetary Interiors*, vol. 178, Feb. 2010, pp. 176–182.
- [5] Archinal, B. A., A’hearn, M. F., Bowell, E., Conrad, A., Consolmagno, G. J., Courtin, R., Fukushima, T., Hestroffer, D., Hilton, J. L., Krasinsky, G. A., Neumann, G., Oberst, J., Seidelmann, P. K., Stooke, P., Tholen, D. J., Thomas, P. C., and Williams, I. P., “Report of the IAU working group on cartographic coordinates and rotational elements: 2009,” *Celestial Mechanics and Dynamical Astronomy*, vol. 109, 2011, pp. 101–135.
- [6] Armstrong, J. W., Iess, L., Tortora, P., and Bertotti, B., “Stochastic Gravitational Wave Background: Upper Limits in the  $10^{-6}$  to  $10^{-3}$  Hz Band,” *The Astrophysical Journal*, vol. 599, Dec. 2003, pp. 806–813.
- [7] Armstrong, J. W., “Low-frequency gravitational wave searches using spacecraft Doppler tracking,” *Living Reviews in Relativity*, vol. 9, 2006.
- [8] Armstrong, J. W., Estabrook, F. B., Asmar, S. W., Iess, L., and Tortora, P., “Reducing antenna mechanical noise in precision spacecraft tracking,” *Radio Science*, vol. 43, Jun. 2008.
- [9] Asmar, S. W., Armstrong, J. W., Iess, L., and Tortora, P., “Spacecraft Doppler tracking: Noise budget and accuracy achievable in precision radio science observations,” *Radio Science*, vol. 40, 2005, pp. 1–9.
- [10] Bar-Sever, Y. E., Jacobs, C. S., Keihm, S., Lanyi, G. E., Naudet, C. J., Rosenberger, H. W., Runge, T. F., Tanner, A. B., and Vigue-Rodi, Y., “Atmospheric Media Calibration for the Deep Space Network,” *Proceedings of the IEEE*, vol. 95, Nov. 2007, pp. 2180–2192.

- [11] Barboglio, F., Iess, L., and Armstrong, J. W., "Precise Doppler measurements for navigation and planetary geodesy using low gain antennas: test result from Cassini," 23rd International Symposium on Space Flight Dynamics (ISSFD), Pasadena (CA), 2012.
- [12] Bertotti, B., and Comoretto, G., "Doppler tracking of spacecraft with multi-frequency links," *Astronomy and Astrophysics*, vol. 269, 1993, pp. 608–616.
- [13] Bertotti, B., Ambrosini, R., Armstrong, J. W., Asmar, S. W., Comoretto, G., Giampieri, G., Iess, L., Koyama, Y., Messeri, A., Vecchio, A., and Wahlquist, H. D., "Search for gravitational wave trains with the spacecraft ULYSSES," *Astronomy and Astrophysics*, vol. 296, 1995, pp. 13–25.
- [14] Bertotti, B., Iess, L., and Tortora, P., "A test of general relativity using radio links with the Cassini spacecraft.," *Nature*, vol. 425, Sep. 2003, pp. 374–6.
- [15] Bertotti, B., Ashby, N., and Iess, L., "The effect of the motion of the Sun on the light-time in interplanetary relativity experiments," *Classical and Quantum Gravity*, vol. 25, Feb. 2008, p. 045013.
- [16] Bierman, G. J., "Factorization methods for discrete sequential estimation," 1977.
- [17] Budnik, F., "Mathematical Formulation of AMFIN", Technical Report, 2008.
- [18] Campbell, J. K., Anderson, J. D., "Gravity field of the saturnian system from Pioneer and Voyager tracking data," *Astronomical Journal*, vol. 97, 1989, pp. 1485–1495.
- [19] Curkendall, D. W., and McReynolds, S. R., "A simplified approach for determining the information content of radio tracking data.," *Journal of Spacecraft and Rockets*, vol. 6, 1969, pp. 520–525.
- [20] Darwin, G. H., "The theory of the figure of the Earth carried to the second order in small quantities. *Mon. Not. R. Astron. Soc.* 60, 82–124, 1899.
- [21] Di Benedetto, M., "The non-gravitational accelerations of the Cassini spacecraft and the nature of the 'Pioneer anomaly,'" PhD Thesis, Università di Roma "La Sapienza", 2011.
- [22] Ekelund, J. E., Esposito, P. B., Benson, R., "DPTRAJ-DP User's Reference Manual. Jet Propulsion Laboratory Navigation Software Group, Technical Report, Vol. 1, 1996.
- [23] Finocchiaro, S., and Iess, L., "The Determination of Jupiter's Angular Momentum from the Lense-Thirring Precession of the Juno Spacecraft," AGU Fall Meeting 2011, 2011.
- [24] Folkner, W. M., Williams, J. G., Boggs, D. H., Park, R. S., and Kuchynka, P., "The Planetary and Lunar Ephemerides DE430 and DE431," *The Interplanetary Network Progress Report*, 2014, pp. 1–81.

- [25] Gao, P., and Stevenson, D. J., “Nonhydrostatic effects and the determination of icy satellites’ moment of inertia,” *Icarus*, vol. 226, 2013, pp. 1185–1191.
- [26] Goldberg, D., “What Every Computer Scientist Should Know about Floating-Point Arithmetic,” *ACM Computing Surveys*, vol. 23, Mar. 1991, pp. 5–48.
- [27] Graziani, A., “Troposphere calibration techniques for deep space probe tracking,” PhD Thesis, University of Bologna, 2010.
- [28] Kliore, A. J., Anderson, J. D., Armstrong, J. W., Asmar, S. W., Hamilton, C. L., Rappaport, N. J., Wahlquist, H. D., Ambrosini, R., Flasar, M. F., French, R. G., Iess, L., Marouf, E. A., and Nagy, A. F., “Cassini Radio Science,” *Space Science Reviews*, vol. 115, Nov. 2004, pp. 1–70.
- [29] Henry, C. A., “An introduction to the design of the Cassini spacecraft,” *Space science reviews*, vol. 104, 2002, pp. 129–153.
- [30] IEEE Std 754-2008, “IEEE Standard for Floating-Point Arithmetic,” IEEE Computer Society, Aug. 2008. doi:10.1109/IEEESTD.2008.4610935
- [31] Iess, L., Rappaport, N. J., Tortora, P., Lunine, J. I., Armstrong, J. W., Asmar, S. W., Somenzi, L., and Zingoni, F., “Gravity field and interior of Rhea from Cassini data analysis,” *Icarus*, vol. 190, Oct. 2007, pp. 585–593.
- [32] Iess, L., Asmar, S. W., and Tortora, P., “MORE: An advanced tracking experiment for the exploration of Mercury with the mission BepiColombo,” *Acta Astronautica*, vol. 65, Sep. 2009, pp. 666–675.
- [33] Iess, L., Jacobson, R. A., Ducci, M., Stevenson, D. J., Lunine, J. I., Armstrong, J. W., Asmar, S. W., Racioppa, P., Rappaport, N. J., and Tortora, P., “The tides of Titan,” *Science (New York, N.Y.)*, vol. 337, Jul. 2012, pp. 457–9.
- [34] Iess, L., Di Benedetto, M., James, N., Mercolino, M., Simone, L., and Tortora, P., “Astra: Interdisciplinary study on enhancement of the end-to-end accuracy for spacecraft tracking techniques,” *Acta Astronautica*, vol. 94, Feb. 2014, pp. 699–707.
- [35] Jacobson, R. A., “Satellite Software Users Guide,” JPL Internal Memo, 2003.
- [36] Jacobson, R. A., Antreasian, P. G., Bordi, J. J., Criddle, K. E., Ionasescu, R., Jones, J. B., Mackenzie, R. A., Meek, M. C., Parcher, D. W., Pelletier, F. J., Owen, W. M., Roth, D. C., Roundhill, I. M., and Stauch, J. R., “The Gravity Field of the Saturnian System from Satellite Observations and Spacecraft Tracking Data,” *The Astronomical Journal*, vol. 132, Jan. 2006, pp. 2520–2526.
- [37] Jacobson, R. A., Antreasian, P. G., Bordi, J. J., Criddle, K. E., Ionasescu, R., Jones, J. B., Mackenzie, R. A., Meek, M. C., Parcher, D. W., Pelletier, F. J., Owen, W. M., Roth, D. C., Roundhill, I. M., and Stauch, J. R., “The Gravity Field of the Saturnian System from Satellite Observations and Spacecraft Tracking Data,” *The Astronomical Journal*, vol. 132, Jan. 2006, pp. 2520–2526.

- [38] Love, A. E. H., "A Treatise on the Mathematical Theory of Elasticity," Cambridge Univ. Press, Cambridge, UK, 1906.
- [39] Mackenzie, R. A., Antreasian, P. G., Bordi, J. J., Criddle, K. E., Ionasescu, R., Jacobson, R. A., Jones, J. B., Parcher, D. W., Pelletier, F. J., Roth, D. C., and Stauch, J. R., "A Determination of Rhea's Gravity Field From Cassini Navigation Analysis," Proceedings of the AAS/AIAA 17th Space Flight Mechanics Meetings, 2007.
- [40] Mackenzie, R. A., Iess, L., Tortora, P., and Rappaport, N. J., "A non-hydrostatic Rhea," Geophysical Research Letters, vol. 35, Mar. 2008, pp. 1–5.
- [41] Mariano, J., and Ramos, H., "Validity of Widrow's model for sinusoidal signals," Measurement, vol. 39, Apr. 2006, pp. 198–203.
- [42] Mariotti, G., and Tortora, P., "Experimental validation of a dual-uplink multifrequency dispersive noise calibration scheme for deep space tracking," Radio Science, vol. 48, Feb. 2013, p. n/a–n/a.
- [43] Matousek, S., "The Juno New Frontiers mission," Acta Astronautica, vol. 61, Nov. 2007, pp. 932–939.
- [44] Matson, D. L., Spilker, L. J., Lebreton, J., "The Cassini/Huygens mission to the Saturnian System," Space Science Reviews 104, pp. 1–58, 2002.
- [45] Milani, A., and Gronchi, G. F., "Theory of orbit determination," Cambridge University Press, 2009.
- [46] Modenini, D., "Investigation on the Navigation Anomaly of Pioneer 10 and 11 probes," PhD Thesis, Università di Bologna, 2012.
- [47] "MONTE-Python Documentation", MONTE version: 089. December 2013.
- [48] Mottinger, N. A., "Updating Navigation Software for Ka-Band Observables—A Progress Report," ipnpr.jpl.nasa.gov, 2004, pp. 1–10.
- [49] Moyer, T. D., "Differenced-Range Doppler Versus Integrated Doppler," The Deep Space Network, Space Programs Summary 37-60, Vol. II, Pasadena CA, 1969, pp. 125-136, <http://hdl.handle.net/2060/19700013503> [retrieved 28 October 2012].
- [50] Moyer, T. D., Mathematical formulation of the Double-Precision Orbit Determination Program (DPODP)., Pasadena (CA): 1971.
- [51] Moyer, T. D., "Formulation for Observed and Computed Values of Deep Space Network Data Types for Navigation," Deep Space Communications and Navigation Series, Monograph 2, Jet Propulsion Laboratory, Pasadena (CA), 2000.

- [52] Naudet, C., Jacobs, C., Keihm, S., Lanyi, G., Linfield, R., Resch, G., Riley, R., Rosenberger, H., and Tanner, A. "The media calibration system for Cassini radio science: Part I." The Telecommunications and Mission Operations Progress Report 42-143, July–September 2000.
- [53] Peters, C. F., "Numerical integration of the satellites of the outer planets," *Astronomy and Astrophysics*, vol. 104, issue 1, pp. 37-41, December 1981.
- [54] Petit, G., and Luzum, B., "IERS Conventions (2010)," IERS Technical Note No. 36, 2010.
- [55] Radau, R., *Sur la loi des densités à l'intérieur de la Terre*. C.R. Acad. Sci. Paris, 100, 972–974, 1885.
- [56] Racioppa, P., "ORACLE Documentation." Università di Roma "La Sapienza", 2012.
- [57] Resch, G. M., Clark, J. E., Keihm, S. J., Lanyi, G. E., Naudet, C. J., Riley, A. L., Rosenberger, H. W., and Tanner, A. B., "The Media Calibration System for Cassini Radio Science: Part II," *The Interplanetary Network Progress Report*, vol. 42, 2001.
- [58] Resch, G. M., Keihm, S. J., Lanyi, G. E., Linfield, R. P., Naudet, C. J., Riley, A. L., Rosenberger, H. W., and Tanner, A. B., "The Media Calibration System for Cassini Radio Science: Part III," *The Interplanetary Network Progress Report*, vol. 42, 2002, pp. 1–12.
- [59] Smith, J., and Buffington, B., "Overview of the Cassini solstice mission trajectory," *Advances in the Astronautical Sciences*, vol. 135, 2009, pp. 829–854.
- [60] Somenzi, L., "Multi arc analysis and least-square fit," Technical Report, Università "La Sapienza", 2006.
- [61] Sripad, A., and Snyder, D., "A necessary and sufficient condition for quantization errors to be uniform and white," *IEEE Transactions on Acoustics, Speech, and Signal Processing*, vol. 25, Oct. 1977, pp. 442–448.
- [62] Standish, E. M., "Time scales in the JPL and CfA ephemerides," *Astronomy and Astrophysics*, vol. 336, 1998, pp. 381–384.
- [63] Taylor, J., Sakamoto, L., and Wong, C. J., "Cassini Orbiter/Huygens Probe telecommunications," DESCANSO Design and Performance Summary Series, 2002.
- [64] Terrien, J., "News from the Bureau International des Poids et Mesures," *Metrologia*, vol. 8, 1971, pp. 32–26.
- [65] Terrien, J., "News from the Bureau International des Poids et Mesures," *Metrologia*, vol. 11, 1975, pp. 179–183.

- [66] Tortora, P., Iess, L., and Ekelund, J. E., “Accurate Navigation of Deep Space Probes using Multifrequency Links: the Cassini Breakthrough during Solar Conjunction Experiments,” IAF abstracts, 34th COSPAR Scientific Assembly, 2002, p. 675.
- [67] Tortora, P., Bordi, J. J., Ekelund, J. E., Iess, L., and Roth, D. C., “Precise Cassini Navigation During Solar Conjunctions Through Multifrequency Plasma Calibrations,” *Journal of Guidance, Control, and Dynamics*, vol. 27, Mar. 2004, pp. 251–257.
- [68] Thomas, P. C., Burns, J. A., Helfenstein, P., Squyres, S., Veverka, J., Porco, C. C., Turtle, E. P., McEwen, A., Denk, T., and Giese, B., “Shapes of the saturnian icy satellites and their significance,” *Icarus*, vol. 190, Oct. 2007, pp. 573–584.
- [69] Thornton, C. L., and Border, J. S., “Radiometric Tracking Techniques for Deep Space Navigation,” *Deep Space Communications and Navigation Series, Monograph 1*, Jet Propulsion Laboratory, Pasadena (CA), October 2000.
- [70] Widrow, B., “Statistical analysis of amplitude quantized sampled-data systems,” *Trans. AIEE*, vol. 79, 1961, pp. 555–567.